HYDROTHERMAL ALTERATION EVENTS IN THE ARCHAEAN COONGAN GREENSTONE BELT

TENDAI RUBABA

August 2022

SUPERVISORS:

Dr. F.J.A van Ruitenbeek

Dr. I.E.A.M Fadel

SCIENTIFIC ADVISOR:

Prof.dr. Kim Hein

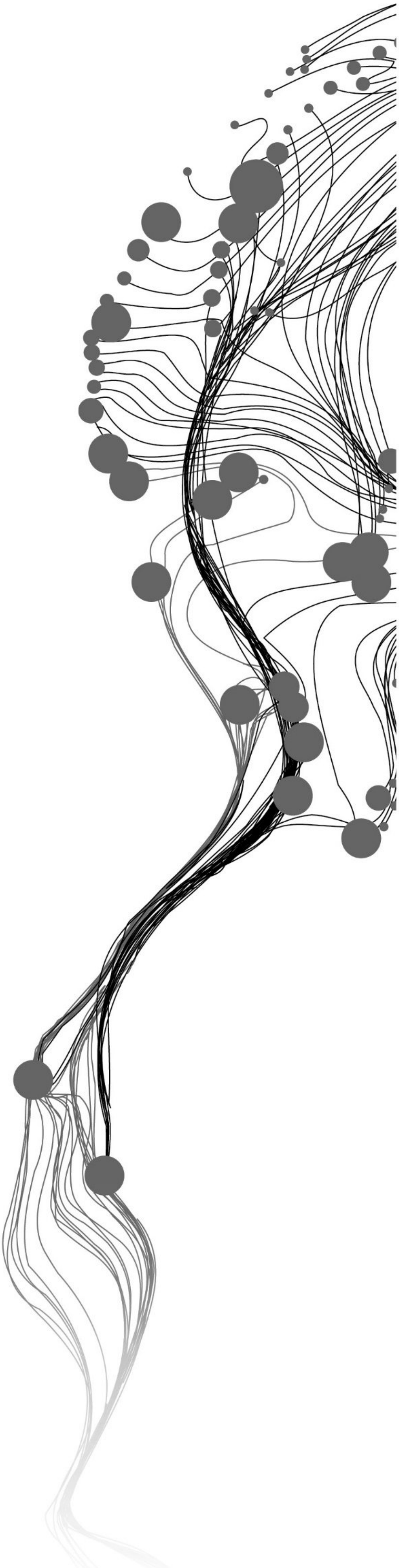

HYDROTHERMAL ALTERATION EVENTS IN THE ARCHAEAN COONGAN GREENSTONE BELT

TENDAI RUBABA
Enschede, The Netherlands, August 2022

Thesis submitted to the Faculty of Geo-Information Science and Earth Observation of the University of Twente in partial fulfilment of the requirements for the degree of Master of Science in Geo-information Science and Earth Observation.

Specialisation: M-GEO: Applied Remote Sensing for Earth Sciences (ARS)

SUPERVISORS:
Dr. F.J.A van Ruitenbeek
Dr. I.E.A.M Fadel
THESIS ADVISOR:
Prof. dr. K. Hein (External Examiner, Emeritus & visiting professor at the University of the Witwatersrand in South Africa)
THESIS ASSESSMENT BOARD:
Dr H.M.A. van der Werff (Chairman)
Dr Martin Schodlok
(External Examiner)

ABSTRACT

Hyperspectral data of the 3-3.5Ga Coongan greenstone belt in the Pilbara craton Western Australia shows the presence of fossiliferous chert horizons and indications of hydrothermal alteration not present in published regional geological maps. These maps show stratigraphic and structural interpretations of geologic events within the volcanic-sedimentary greenstone sequence; however, little detail exists about the hydrothermal events and the extent of hydrothermal alteration within the greenstone belt. This study seeks to map the hydrothermal alteration patterns and related paleosurfaces to predict the relative timing of geologic events and possible linkages with early life in this context. This research employs an integrated analysis informed by remote sensing hyperspectral imagery, aerial photos and airborne geophysics for a detailed mapping of the hydrothermal systems and paleo-surfaces. Geophysical data were used to form the framework of the study, showing the mineral zonation and general division of the nCGB. Potential paleosurfaces were identified through the nature of the contacts. Subsequently, mineral mapping techniques were applied to the airborne hyperspectral data, and a mineral map was produced. Interpretations of the occurrence and spatial distribution of hydrothermal minerals were done to see how they related to the general division of the study area.

Research findings identified seven potential paleosurfaces. Mineral mapping results indicate that the volcano-sedimentary sequence has been altered to various alteration assemblages ranging from chlorite-carbonate to different types of white micas and pyrophyllite. The spatial distribution of alteration minerals indicates episodes of hydrothermal alteration connected to paleo-layers within the volcano-sedimentary sequence. The classified hydrothermal alteration minerals showed white micas (muscovite, paragonite, phengite, illite), clay minerals (pyrophyllite, kaolinite, dickite), silicates (amphibole, biotite epidote, chlorite, talc), carbonate minerals (dolomite), sulfate minerals (alunite) and iron oxides (hematite, goethite). The occurrence of pyrophyllite indicates reducing acidic conditions, silica-rich and low-intermediate temperature hydrothermal fluids. Variations in pyrophyllite and muscovite up the stratigraphy towards the paleosurface suggest a connected hydrothermal system with changing temperature, acidity and redox conditions. The identification of paleosurfaces stands as evidence of paleoclimates paleoenvironments and conditions. The spatial distribution of these hydrothermal alteration minerals and rock unit characteristics were summarised and organised into a relative chronology of events for the nCGB. The overall sequence of events shows a younging direction up the stratigraphy towards the east. The findings show a correlation between the potential paleosurfaces, formation, interpreted hydrothermal alteration, and inferred changes in paleoenvironment across the study area, indicating that there have been temporal changes in the northern Coongan Greenstone Belt with part of the field indicating a connected hydrothermal system with changing temperature, acidity and redox conditions.

Keywords: Hyperspectral, Hydrothermal, Alteration, Archaean, Coongan, Data Integration, Greenstone Belt, Geochronology, Relative-timing, Pyrophyllite, White micas, Paleosurface

ACKNOWLEDGEMENTS

I want to thank my supervisors, Dr F.J.A van Ruitenbeek and Dr I.E.A.M Fadel, for their amazing guidance and support throughout this research. They gave me confidence when mine was wavering, ensuring I saw this project through until the end. A special thank you also goes to my advisor Prof. dr. K. Hein, whose feedback ensured that I was on the right track with the research.

I thank IGO Limited and Brian Bennett (Western Geospectral) for providing the AMS hyperspectral images on which much of this reserach relied on.

I also want to thank my mother, an unwavering pillar of strength and inspiration whose stories of a similar journey kept me going and constantly reminded me that "we finish what we started".

My gratitude also goes to Memory and Getnet, who were always around to listen, discuss, and read through my drafts, especially when I felt a little lost in my work.

Lastly, I would like to thank my family and friends who encouraged and supported me during the entire research process.

TABLE OF CONTENTS

LIST OF FIGURES

LIST OF TABLES

LIST OF ABBREVIATIONS

CGB: Coongan Greenstone Belt

nCGB: Northern part of Coongan greenstone Belt

nm: nanometres

HSV: Hue Saturation Value

SWIR: Short-wave Infrared

VNIR: Visible -Near Infrared

ppm: parts per million

cps: counts per second

1. INTRODUCTION

1.1. Background and justification

The evolution and understanding of early life on Earth have always interested Earth scientists. The formation processes of Earth are crucial in the development of geologic events and their timing, geomorphological changes, mineral exploration, and, most recently, searches for life on other planets such as Mars (Hickman and Van Kranendonk, 2012; Van Kranendonk, 2006; Walter and Des Marais, 1993). Of significance to Earth's formation are paleosurfaces; ancient rock surfaces in the rock record formed by a specific culmination of tectonic and environmental changes (Widdowson, 1997). This definition reflects the geological and geomorphological facets of erosion, deposition and tectonic processes. Hydrothermal activity is considered to be at the core of tectonic processes of crustal uplift and igneous activity (Pirajno, 2009a), driving magma formation, circulation and ultimately deposition. The hydrothermal systems generate distinct surfaces indicative of the fluid types and environmental conditions such as temperature and pressure (Sillitoe, 2015).

Hence, paleosurfaces in this study are defined as identifiable and distinct surfaces highlighting different depositional stratigraphies, dynamic environments and hydrothermal activity preserved over time. The critical assessment of paleosurfaces then creates an opportunity to investigate the hydrothermal history of early Earth and succeeding geologic terranes as we see today.

Pirajno (2009b) and Sillitoe (2015) suggested that hydrothermal processes played a pivotal role in the formation of the Earth. Hydrothermal alteration is a process where hydrothermal fluids interact with surrounding rocks, influencing the development of new mineral assemblages. The deposition of the altered minerals is a result of the composition, temperature and pressure of the fluids and the rocks (Pirajno, 2009b). Understanding these mineral systems involves defining the source and transport system for metal and fluids for the mineral formation (Wyborn et al.,1994). Hence, mapping the chronological changes like hydrothermal alteration allows insight into the evolution, timing, environmental conditions, and hydrothermal record. Different Earth processes are related to paleosurfaces and should be recognised through their unique descriptive characteristics (Widdowson, 1997). Likewise, the identification of preserved paleosurfaces proves to be a proxy for predicting hydrothermal sites of discharge and insight into the stratigraphy and hydrothermal events in relative time.

The presence of biological fossils in pre-Phanerozoic rocks (<550Ma) in variable habitats signifies the preservation of early life in the rock record (Eriksson et al., 2001; Beraldi-Campesi, 2013). The formation and evolution of ancient habitats through time are thus better understood from the hydrothermal events that form these rocks, and on paleosurfaces, they are identified. Research on the existence of life on other planets such as Mars (Walter and Des Marais, 1993) is based on scientific findings determined from these ancient environments.

Concurrently, hydrothermal events influence the type of mineralisation occurring in each environment. Understanding the different hydrothermal processes may lead to identifying mineral targets before extensive exploration (Haldar, 2018). Not all mineral occurrences are economically viable (Ericsson and Löf, 2019; Yousefi et al., 2019). It is then necessary to strategically target viable ore deposits driven by knowledge and existing data. Therefore, understanding both early-life and mineralisation processes holds significance to the perpetuity of human existence and economic growth.

Remote sensing methods have made inroads in their application in geological and geographical surveys, mineral mapping and environmental studies (Gupta, 1991). Spectral analysis is a remote sensing technique used to identify and map minerals in the electromagnetic spectrum's visible and infrared (300-3000nm) range (Hunt, 1977; Clark et al., 1990). Minerals absorb light at specific wavelengths creating spectral absorption features unique to individual minerals or mineral groups (Hecker et al., 2019b). According to Yousefi et al. (2019), remote sensing geospatial technologies allow for collective acquisition, storage and high-speed processing of multi-disciplinary data sets to comprehensively interpret geology. With such broad applications, remote sensing is suitable for discriminating details of the Earth's land surface and supplying vital support for geological reconstructions.

With the evolution and advancement of remote sensing technologies, the identification and discretion of surface features only stand to improve. In particular, the applicability of hyperspectral remote sensing has become significant in giving detailed and accurate information on mineralogical spectroscopy signatures at both the regional and local scales (Magendrana and Sanjeevi, 2014; Tripathi and Govil, 2019; Cudahy et al., 2002); highlighting the sensitivity of hyperspectral sensors to detect surficial minerals. Examples of minerals identifiable using hyperspectral mapping include clay, sulphate, carbonate, hydroxides, silica and oxide minerals (Hunt, 1977; van der Meer et al., 2012; Tripathi et al., 2020). Spectroscopy can identify different minerals associated with hydrothermal alteration and give insight into the compositional and formation processes that have taken place in a particular environment.

Historical studies have traced the nature of early-Earth formational processes. The critical objectives centred on the nature of formational processes with a robust debate between vertical diapirism (Hamilton, 1998) and tangential plate motion (De Wit, 1998). As the relics of paleoenvironments, Archaean cratons have been the focus of these studies (Nijman et al., 2017). The Archaean cratons are remnants of the Earth's early (4.6Ga) continental lithosphere and are considered to host complex geological environments known as greenstone belts (Goodwin, 1981). Archaean Greenstone belts are regions with well-preserved paleo-surfaces, and possible signs of ancient mineral systems are still observed (Kranendonk et al., 2002; Hickman and Van Kranendonk, 2012). Because of their preserved nature, signatures of early life and associated habitats can be identified in these greenstone belts (Eriksson et al., 2001). Furthermore, Archaean Greenstone belts are identified as diverse well-preserved rocks and textures influenced by different deformation and tectonic events and hydrothermal activity (Anhaeusser, 2014). Thus, studying these regions with hyperspectral mapping helps identify the interplay of ancient hydrothermal activities through deposited mineralisation to interpret the evolution environments.

The Eastern Pilbara Craton in Western Australia is one of the most preserved Archaean cratons on Earth, with its evolution and stabilisation forming between 3.72 to 2.85 Ga. Within the East Pilbara Craton is the Coongan greenstone belt, which has significant exposures of the oldest rocks, in which evidence of early life is associated with hydrothermal alteration mineral deposition (Zegers, 1996). Although cycles of deformation and metamorphism complicate the location and make interpretation of stratigraphic units more complicated (Trofimovs et al., 2006), preserved surfaces within the Coongan provide a basis to study hydrothermal processes and the evidence for early life.

The limitation of effective tools to target and effectively explore through cover has been improved by technological improvements that have seen the continual progression of hyperspectral remote sensing support for improved analysis of possible geological placement events (van der Meer et al., 2012). Hyperspectral mapping provides access to high-resolution data sets and renews the efforts to better predict the interpretations of formational processes. Furthermore, complementary airborne and geophysical data ultimately enable comprehensive interpretation of the geologic events within the Coongan Greenstone Belt. Adopting an integrated approach of multi-disciplinary remote sensing techniques of different resolutions can improve details of the formation processes and likely constrain them within specific times. Overall, the different sources of information, of either low-resolution or high resolution, offer both the regional and local perspective in an integral approach and could lead to a comprehensive geological interpretation.

In this study, hyperspectral data will be used to map the mineralogy of the Coongan greenstone belt to understand the hydrothermal events and related paleosurfaces in the area's development. This is to better characterise the existing mineralogical systems, predict their formation and trace early life evidence. Additional geophysical data and high-resolution aerial photography will complement the hyperspectral data in the mapping and interpretation. Moreover, the availability of field observation data is an additional positive, as it gives a more explicit synopsis of the field status and additional value addition to result analysis and data validation possibilities of the mapping results

1.2. Research problem

Hyperspectral data on the Coongan greenstone belt shows the existence of chert horizons and hydrothermal alteration that are not present in the regional geologic map (Van Ruitenbeek et al., 2012). However, little detail is known about the hydrothermal events and extent of alteration within this part of the greenstone belt. The interpretations of geologic events, whilst derived from the stratigraphic and structural point of view, have not focused on the role of hydrothermal fluids in rock alteration processes. These hydrothermal fluids are a key variable in predicting formation processes, depositional environments, paleosurfaces, transport systems and, therefore, reconstructing events. Understanding these relationships will improve the understanding of the relative timing of events within the Coongan greenstone belt

1.3. Research objectives

1.3.1. General objective

The overall objective of this study is to determine the type and extent of hydrothermal alteration (and related paleosurfaces) in the Coongan greenstone belt using hyperspectral and geophysical mapping and thereby form an understanding of the relative timing of geologic events within the greenstone belt.

1.3.2. Specific objectives

- To identify and map different hydrothermal alteration minerals in the study area using hyperspectral mapping
- To relate the spatial distribution of identified alteration minerals to existing geophysical maps to identify and delineate paleosurfaces
- To predict the conditions and depositional environments of the alteration minerals
- To interpret the alteration mineral and paleosurface maps applying the stratigraphical principles of geology
- To understand the relationships between the hydrothermal events and relative timing of formational processes within the Coongan greenstone belt

1.3.3. Research Questions

1. Which hydrothermal alteration minerals can be classified using hyperspectral mapping in the study area?
2. Which paleosurfaces are distinguished, and what is their relationship with identified surface minerals?
3. Are there recognisable patterns at the paleosurfaces in relation to continuity, mineral patterns, and depth?
4. What is the role of the multi-disciplinary data sets in improving the understanding of the development systems in the study area?
5. Which role did the hydrothermal events play in the study area, and can they be distinguished temporally?

1.4. Thesis structure

The thesis is organised into seven chapters as follows:

Chapter 1: Introductory chapter highlights the background and justification, research problem, overall and specific objectives and research questions of the study

Chapter 2: Deals with the scope of the study and review of the literature relevant to the study

Chapter 3: Describes the instrumentation and datasets used for the research

Chapter 4: Describes the research methodology, materials and experimental procedures undertaken during the study

Chapter 5: Presents the study's findings, analysis, and data interpretation

Chapter 6: Deals with discussions and interpretations of the final output and limitations of the research and recommendations for further studies
Chapter 7: Draws the conclusions

2. LITERATURE REVIEW

In this chapter, the following sections are presented: location of the study area (2.1), geology of the study area (2.2), paleosurfaces and hydrothermal activity (2.3), hydrothermal alteration in the Pilbara area (2.4), remote sensing of hydrothermal minerals and hyperspectral data(2.5) and data integration approach (2.6).

2.1. Location of Study Area

The northern part of the Coongan greenstone belt (nCGB) is located within the East Pilbara Craton of Western Australia (Figure 1). It is situated within latitudes -21.24°N and -21.30°N and longitudes 119.36°E and 119.42°E (UTM50S 770426.3E, 7634283.9N, 777281.3E and 7623028.9N). The study area is accessible via graded roads from Port Hedland (Figure 1a) with Marble Bar to the north and Newman to the south. Most of the area is accessible by car, whilst the most rugged portions are only accessible by foot.

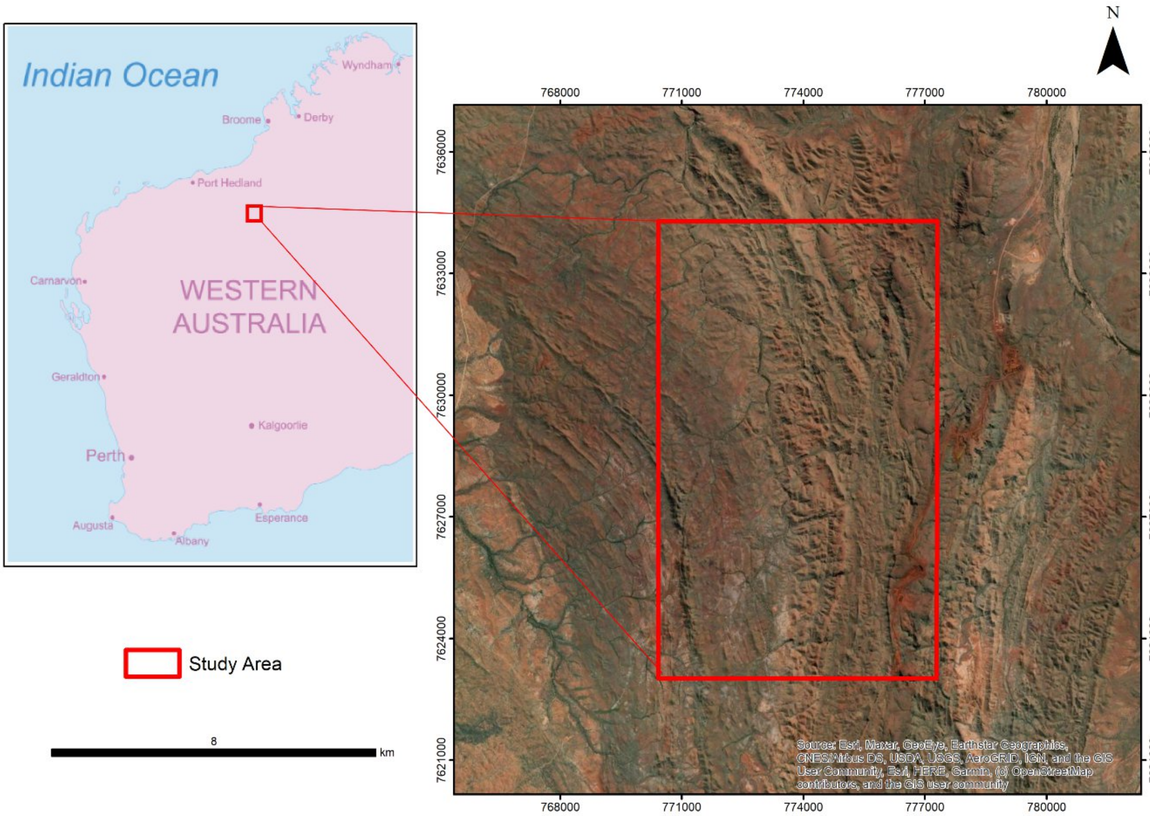

Figure 1: Location of the study area: (a) the map inset to the left shows site and location access, (b) while the map on the right shows the topographic imagery of the area

The Coongan area is characterised by an undulating terrain controlled by bedrock geology. Strike-controlled ridges and hills cover the south-eastern, western and south-western areas (Figure 1b). The north and central parts are mostly flat colluvial-alluvial plains transacted by several large rivers such as the Coongan and Talga rivers. A dry climate with alternating wet and dry seasons is typical for the study area. Vegetation is dominated by spinifex grass species usually close to near-surface water. Other areas also have eucalypts, wattles and small shrubs.

2.2. Geology of the Study Area

2.2.1. Regional Geology

The Pilbara craton in Western Australia is one of the oldest Archaean cratons on Earth, with the other being the Kaapval craton of South Africa (Van Kranendonk et al., 2002). Van Kranendonk (2002;2006) split the Pilbara Craton into granite-greenstone terranes as the 3.52 – 3.23 Ga East Pilbara Terrane, the 3.27 – 3.07 Ga West Pilbara Superterrane and the (approximately dated) 3.18 Ga Kurrana Terrane. Of these terranes, The East Pilbara craton hosts some of the oldest and very well preserved rocks on Earth and evidence of early life (Schopf and Packer, 1987; Zegers, 1996) and are associated with stromalitic and microfossil occurrences (Van Kranendonk, 2006). The craton's preserved nature makes it relevant to investigating evolution processes across various periods. This is because some markers of geological processes are still identifiable in the present day and can be studied. Moreover, the East Pilbara craton is well known and has been studied significantly due to the controversial tectonic evolution. Geological interpretations set East-Pilbara's tectonic and stratigraphical terrane as having formed from either a back-arch sequence (Brauhart et al., 1998) or granitoid diapirism, with clear granitic domes and greenstone keels (Van Kranendonk et al., 2002).

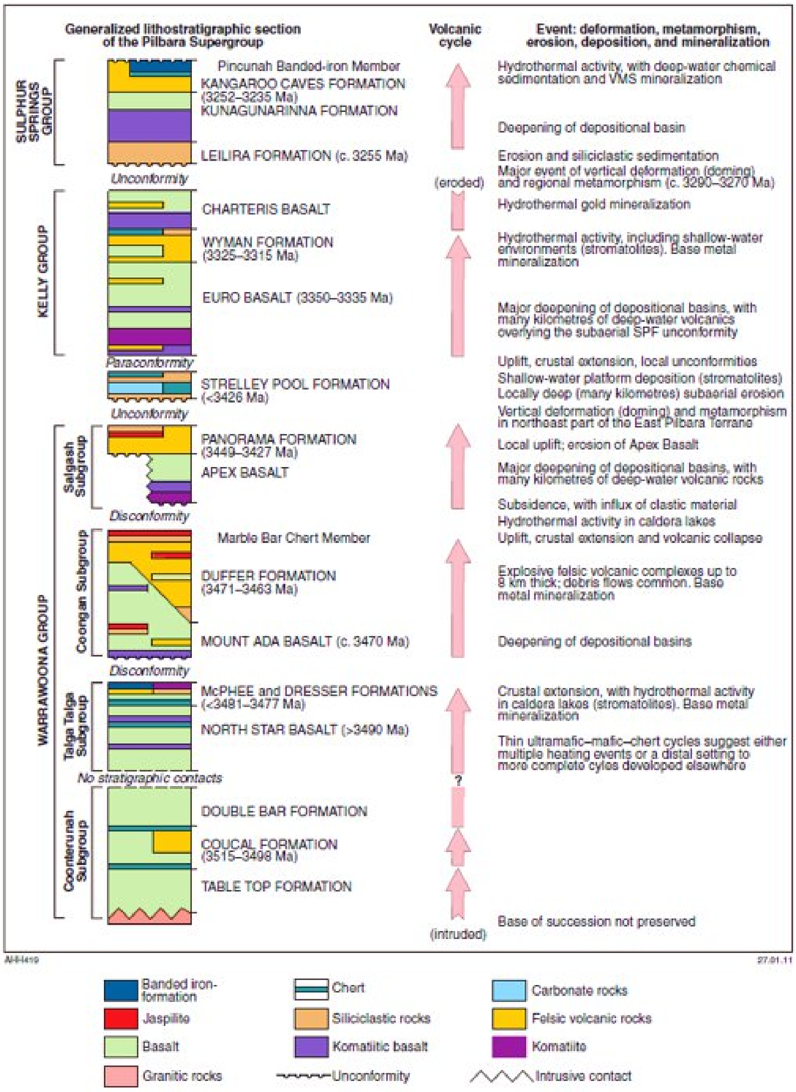

Figure 2: Simplified stratigraphy of the Pilbara Supergroup within the East Pilbara Terrane (adapted from Hickman,2011)

A varying range of exploratory scientific and non-scientific research has been carried out in the region (Hickman, 2012; Nijman et al., 2017) with several revisions of the rock formations (Van Kranendonk, 2010; Hickman, 2011). The Pilbara Supergroup illustrated in Figure 2 is made up of volcano-sedimentary groups of the Warrawoona (ca.3.49-3.31Ga), Kelly (3.35-3.30Ga), Sulphur Springs (ca. 3.26-3.24 Ga), Gorge Creek (ca. 3.24-2.94 Ga) and De Grey (ca. 2.94 Ga) (Hickman, 1983; Zegers, 1996; Van Kranendonk et al., 2002;

Hickman and Van Kranendonk, 2012). The Warrawoona Group is made of basaltic volcanic rocks with felsic volcano-sedimentary pulses. A conglomeratic quartzite-rich formation known as the Strelley Formation was unconformably deposited overlying Warrawoona, and evidence of silicified and stromatolitic carbonates are present at the top. As shown in Figure 2, the Kelly Group conformably lies above the Strelley Formation; it is made up of interbedded basalt and komatiites rock unit of high-K rhyolite derived from the melting of older felsic crust (Van Kranendonk et al., 2002). Deposition of the Sulphur Springs Group over a regional unconformity is characterised by a sedimentary base overlain by volcanic komatiites, andesite, and rhyolites hosting volcanogenic sulfide deposits. Dykes and sills ranging from ultramafic to felsic in composition intrude and crosscut these rock successions across the region (Hickman, 1983; Van Kranendonk et al., 2002). Several shear zones have also been mapped, transacting the rock succession (Zegers, 1996). At the top of the Pilbara Supergroup, low-grade metasedimentary and metavolcanic rocks of the De Grey Supergroup (ca.2.94 Ga) and Fortescue Group (2750Ma) are found (Van Kranendonk, 2010). Furthermore, the rocks of the Pilbara supergroup have undergone low-grade seafloor metamorphism to high-grade contact metamorphism, with marked amphibolite facies and greenschist facies going up the stratigraphy (Hickman, 1983; Van Kranendonk et al., 2002; Van Kranendonk, 2006).

2.2.2. Local Geology

The nCGB is part of the East Pilbara Craton, and the corresponding stratigraphy of the nCGB was put forward by Hickman (1983), Dirmaco and Lowe (1989), Zegers (1996) and Van Krandendonk (2002). From these studies, the widely accepted stratigraphy shows the Warrawoona(ca.3.52-3.42Ga), Kelly (ca.3.35-3.30Ga), Dalton Suite(ca.3.20-3.07Ga), Gorge Creek(ca.3.05-2.94Ga), Croydon(ca.2.97-2.94Ga), and Fortescue (ca.2.78- 2.63Ga) Group rock types (Geoscience Australia and Australian Stratigraphy Commission, 2017). This stratigraphy is evident in the 1:100 000 scale geological map (Figure 3) after (Hickman and Van Kranendonk, 2008; Van Kranendonk, 2010). It is established that most of the Coongan sequences are from the Warrawoona Group of Pilbara Supergroup (Zegers, 1996). A summary of this stratigraphy (Hickman and Van Kranendonk, 2008; Van Kranendonk, 2010) is given below from oldest to youngest:

- Talga Talga Sub-Group (ca. 3.49-3.47) of the Warrawoona Group is a 6km mafic unit of pillow basalts, gabbros, and doleritic sills interbedded by a 0.6km ultramafic unit. Banded iron formations(BIFs) and cherts layers are included.
- Duffer Formation (ca. 3.47-3.49Ga), a felsic 1-3km thick unit of intercalated volcanic and sedimentary rocks. The felsic volcanics include rhyolite, dacite with sedimentary units of sandstone, chert, conglomerate BIF turbidite and chert.
- Panorama Formation is a ~100m thick basal unit of the Salgash Sub-Group, with ash-fall tuff, a minor amount of siltstone, breccia and felsic lava.
- Salgash Sub-Group (ca. 3.45—3.42Ga) of the Warrawoona Group with pillowed and komatiitic basalt and chert.

- Strelley Pool Formation (ca. 3.42-3.35Ga) is a 20-25 metres thick chert unit containing different stromatolite and microfossils. The unit overlies the Duffer formation. This formation separates rocks of the Warawoona group from those of the Kelly Group.
- Kelly Group (ca. 3.35-3.30Ga) comprises basaltic to komatiitic volcanics, felsic tuff and thin chert beds, collectively termed the Euro Basalt (ca. 3395-3325 Ma). In turn, the Euro Basalt is conformably overlain by volcanoclastic rocks and massive, or, columnar jointed rhyolite of the Wyman Formation.
- Wyman Formation (ca. 3.32-3.31Ga), is a ~1km rhyolite and chert unit that forms the upper sequence of the Kelly Group. This formation unconformably overlies the Salgash Sub-group.
- Emu Pool Suite is a relatively felsic composition compared to the surrounding mafic rocks. It includes meta-monzogranite and mafic schist rock types dated at ca. 3.32-3.29 Ga.
- Cleaverville formation (ca. 3.02-3.05Ga) of the Gorge Creek Group is a ~1km thick banded iron formation and has residual Cenozoic sediments in most parts of the unit.
- Lalla Rookh Sandstone (ca. 2.95-2.94Ga) overlying the Cleaverville formation consisting of beds of sandstone, siltstone and minor conglomerate
- Mt Roe Basalt of the Fortescue Group (ca.2.78-2.62Ga) unconformably overlies the Lalla Rookh Sandstone. It comprises pillowed and hyaloclastite breccia

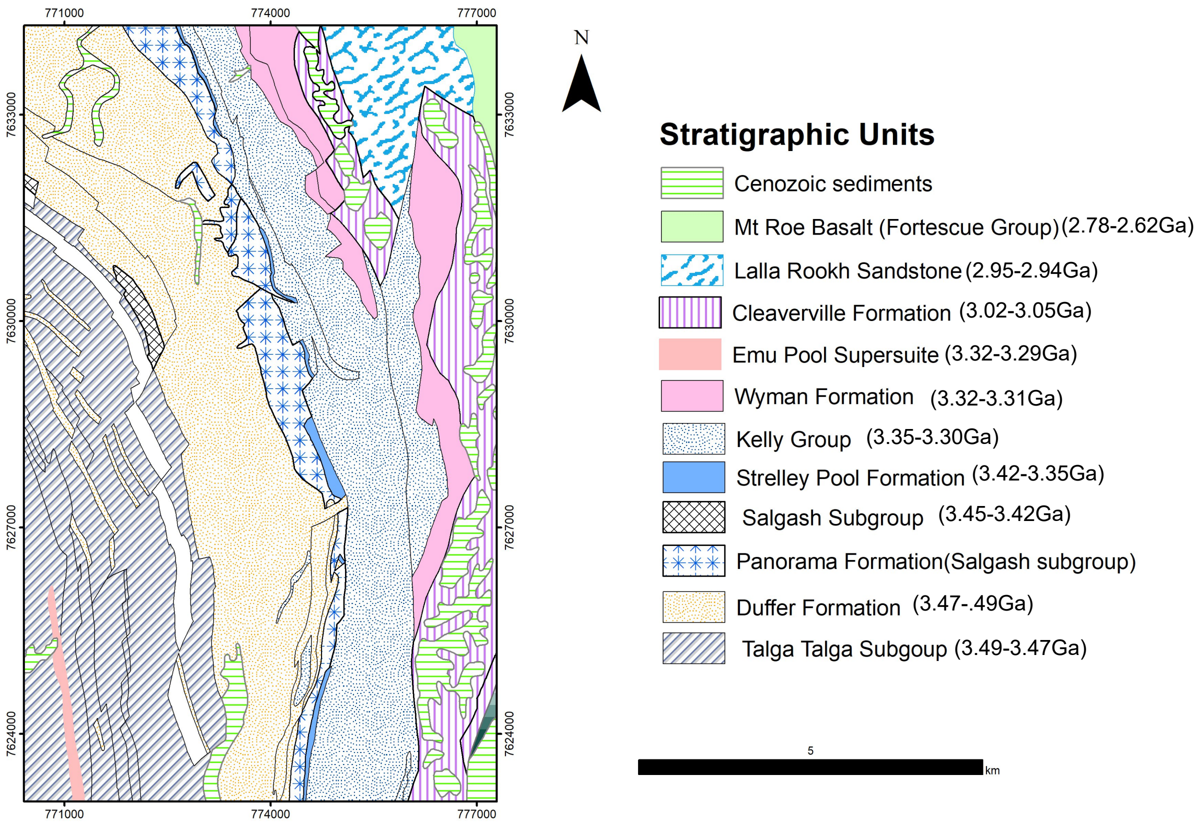

Figure 3: Geological Map of the Coongan Greenstone Belt showing the stratigraphic units as summarised by (Hickman and Van Kranendonk, 2008; Van Kranendonk, 2010)

Several deformation events took place in the East Pilbara terrane between 3.49-2.94 Ga (Zegers, 1996; Van Kranendonk et al., 2002; Van Kranendonk et al., 2002). In accordance to these events, lithologies of the nCGB have been deformed with the development of numerous northerly-trending shear zones (such as the Central Coongan and Split Rock Shear Zone), and undergone regional greenschist facies metamorphism (Hickman, 1983; Zegers, 1996). Additionally the granitoids of the nCGB are associated with development of amphibolite facies in the contact zone.

2.2.3. Related Work

An alternative stratigraphy has been brought forward by Hein et al., n.d., which incorporates field observations, interpretation of aerial photographs, and topographic data on a 1:25 000 scale. The unpublished paper summarises the stratigraphy and significant geological structures of the nCGB using simple cross-cutting relationships. Observations from this study inferred a stratigraphic facing eastwards (younger towards the east) across the entire belt, different to the previous studies on the greenstone belt. Additionally, no evidence was found to support the existence of the Split Rock Shear Zone within the Coongan greenstone belt, as reported by Zegers (1996).

The 1:25 000 scale map by Hein et al. (n.d.) and 1: 100 000 scale map by Hickman and Van Kranendonk (2008) are the current standing stratigraphies and the basis for this study. Correlations of the data studied in this research to either of the current stratigraphies will contribute to any new interpretations of the Coongan area. This study and interpretations thereof hope to be the starting point of alternative relative stratigraphical sequencing within the nCGB.

2.3. Paleo-surfaces and hydrothermal activity

Most hydrothermal and geothermal systems are identified as distinct surface or shallow subsurface geomorphological horizons, formed when different fluids are discharged under varying environmental conditions. Relics of these paleo-horizons are preserved either entirely or in a semi-eroded state (Cudahy et al., 2002). Additionally, the preserved paleo-surfaces and associated products reveal the formational age, tectonic setting, climate and hydrothermal fluid content and alteration zones at deposition (Sillitoe, 2015). Hence, the preserved nature of the Coongan greenstone Belt provides a way to study both the paleo-environments and associated hydrothermal systems.

The broad field mapping and petrogenic analysis executed in the Pilbara identified the paleoenvironments for the microfossils to be primarily hydrothermal (Brasier et al., 2002; Brasier et al., 2005). Related previous work on Archaean hydrothermal systems greenstones (Wit and Furnes, 2016; de Wit et al., 1982; Brauhart et al., 1998) as well as identified volcanogenic massive sulphides (VMS) and barite mineralisation (Van Kranendonk, 2006; Van Kranendonk and Pirajno, 2004) within the Pilbara Craton also serve as evidence of hydrothermal activity within the Coongan. Epigenetic gold mineralisation of various ages have also been identified within the rocks of the Pilbara Supergroup (Huston et al., 2002). Markers of deformation from regional greenschist facies within lithologies to amphibolite facies at contact zones have also been identified within the nCGB (Hickman, 1983; Zegers, 1996). These studies form the basis for understanding the hydrothermal systems operating within the study area.

2.4. Hydrothermal Ateration in the Pilbara Craton

Hydrothermal systems typically involve fluid pathways by which seawater and magmatic fluids are recharged at low temperatures zones and discharged at high temperatures zones (Gifkins et al., 2005). These fluids interact with the wall-rock changing the fluid composition, thus forming hydrothermal alteration minerals (Pirajno, 2009b).

Brauhart (1998) defined the alteration distribution of the Panorama into four alteration facies; feldspar, feldspar-sericite-quartz, feldspar-destructive sericite-quartz and chlorite-quartz alteration. An analysis by Van Kranendonk and Pirajno (2004) of altered and unaltered metabasalts of the Coonterunah and Warawoona Groups established the existence of advanced argillic, argillic, phyllic, and propylitic alteration zones. Together with the silica-alunite alteration of dolomitic cherts in the area, these zones were interpreted to have been products of periodic seafloor hydrothermal circulation. Work by Van Ruitenbeek (2005) established fluid pathways using white micas in hydrothermal systems and volcanic massive sulphide (VMS) systems. Brown et al (2006), also characterised the hydrothermal system of the Panorama Formation of the North Pole Dome as an acid-sulfate epithermal system controlled by vertical veins. The hyperspectral data identified muscovite to pyrophyllite altering, indicating acidic reducing fluids, associated with the preserved mineral assemblages in the area. The abundance and variation of aluminium content of the white micas illustrated dynamic environment conditions and hydrothermal facies within the Archean terrane (Brown et al., 2006). These relevant studies offer insight into the probable existence of hydrothermal alteration within the Coongan greenstone belt within the Pilbara.

2.5. Remote Sensing of Hydrothermal Minerals using SWIR Spectroscopy and Hyperspectral Data

Hydrothermal alteration has been poorly studied within the Coongan greenstone belt. With the advance in technologies and application of hyperspectral remote sensing in geology, mapping of surface mineralogy has increasingly been adopted (van der Meer et al., 2012). Spectral features and signatures of minerals with the hydroxyl (OH-) cation result from the absorption at specific wavelengths within the visible and near-infrared (0.325-2.5µm). The shortwave infrared (SWIR) range of 2.0-2.5 µm covers spectral features of hydroxyl-bearing minerals, clays, phyllosilicates, carbonates and sulfates (Hunt, 1977). These minerals are predominantly common in hydrothermal systems (Table 1), making them suitable for analysis with hyperspectral spectroscopy technology. Image pixel spectra are attained using various methods, including techniques described by Bakker et al. (2011) and Hecker et al. (2019a). from these, mineral spectra are quantified and validated by matching to library and field spectra for compositional information.

Table 1: Summary of main spectrally active minerals with different alteration (van der Meer et al., 2012)

Environment of formation	Main spectrally active alteration minerals
High sulfidation epithermal	Alunite, pyrophyllite, dickite, kaolinite, diaspore, zunyite, smectite, illite
Low sulfidation epithermal	Sericite, illite smectite, chlorite, carbonate
Porphyry: Cu, Cu-Au	Biotite, anhydrite, chlorite, sericite, pyrophyllite, zeolite, smectite, carbonate, tourmaline
Carlin-type	Illite, dickite, kaolinite
Volcanogenic massive sulphide	Sericite, chlorite, chloritoid, carbonates, anhydrite, gypsum, amphibole
Archaean Lode Gold	Carbonate, talc, tremolite, muscovite, paragonite
Calcic skarn	Garnet, clinopyroxene, wollastonite, actinolite
Retrograde skarn	Calcite, chlorite, hematite, illite
Magnesium skarn	Forsterite, serpentine-talc, magnetite, calcite

Zones of alteration minerals, including pyrophyllite, were identified in the North Pole Dome of the Pilbara using hyperspectral remote sensing (Brown et al., 2006). Other works by (Portela et al., 2021, Hecker et al., 2019, and Van Ruitenbeek et al., 2005) also illustrate the use of hyperspectral remote sensing in hydrothermal systems. The hydrothermal surface manifestations in the Coongan can be tested against these techniques to characterise alteration occurrence.

2.6. Data Integration Approach

The main concern with the application of remote sensing in geology is the limited satellite data continuity (van der Meer et al., 2012). Geologic products such as lithologic maps, geophysical data and field observations should be integrated with remote sensing data to analyse geologic processes. The combined use of multi-disciplinary techniques allows for validation and quantifiable geological interpretations. Data across disciplines of varying resolution allow for regional and local analysis, from as little detail as possible to great detail over a study area. Hence in a study such as this, the ability to quantify and validate remote sensing and field data offers a comprehensive interpretation.

3. DATASETS AND SOFTWARE

This chapter highlights the datasets and software used in this research. The datasets includes airborne hyperspectral data(3.1), aerial photography (3.2), geological map (3.3) airborne geophysical data (3.4), spectral libraries (3.5) and fieldwork notes (3.6).

3.1. AMS Airborne Hyperspectral data

The AMS hyperspectral data was acquired from a flight campaign of the study area in November 1998. Three (3) scenes, EP0530-EPE0532, outline the extents of the study area bounded within the coordinates -21°25'15, 119°37'24; -21°25'15, 119°39'53. The spectrometer has a total of 64 bands AMS1-32 and AMS65-96. The wavelength range covering both visible-near infrared (VNIR) and short-wave infrared (SWIR) between 530nm- 2500nm. However, the data has no recorded features between 1000nm-1900nm to improve the signal to noise in the lower wavelength range. Hyperspectral images from the airborne survey are calibrated, and atmospherically corrected (radiances to reflectance) with a spatial resolution of 5m and can be georeferenced after spectral processing. AMS data is used in this research due to its SWIR region spectral coverage that is of interest in alteration mineral mapping as well as Fe-oxide mineral identification in the VNIR (Abubakar et al., 2018).

3.2. Aerial photograph

A high-resolution colour aerial photograph with a spatial resolution of 0.77m from a flight survey on 20 September 1993 of the study area is used in the research. The data is held in GDA decimal degrees. The photo provided by ITC had limited metadata except for the aforementioned.

3.3. Geological Map

A detailed 1:100 000 scale geological map (Van Kranendonk, 2010), first edition, published under the title of Marble Bar (2855) by the Geological Survey of Western Australia (Hickman and Van Kranendonk, 2008), encompasses the research study area. The detailed map held in GDA decimal degrees, provides information on geological units, structural geology and fault systems of the region. This map has a positional accuracy of 10 to 100 metres, with all geological units classified using standard geological nomenclature.

3.4. Airborne Magnetic and Radiometric Data

Airborne magnetic and gamma-ray images acquired in 2009 by Fugro Airborne Surveys for Gondwana Resources Limited. Details of the survey were reported by Lawrence and Stenning (2009), and used in this study. An aircraft Geometrics G-822A ultra-high sensitivity Caesium vapour magnetometer sensor with an operating range of 20,000 to 100,000 nT and nominal sensitivity of 0.001nT was used. The gamma-ray spectrometer GR-820 with 256 channels to measure K, Th, U and Total Count. Whilst the spectrometer used was calibrated to ppm and %, the data was gridded to cps for the individual radioelements. Both the magnetic and gamma-ray surveys were carried out with a flightline spacing of 50m. The grids are corrected for background noise, deadtime, calibrated and an overall spatial resolution of 12.5m.

3.5. Spectral Libraries

Hyperspectral mineral spectra from the study are resampled and compared with the USGS and JPL libraries. The USGS and JPL spectral libraries are open source and accessed via the USGS and JPL websites at https://speclab.cr.usgs.gov/spectral-lib.html and
https://speclib.jpl.nasa.gov/documents/jpl_desc
https://speclib.jpl.nasa.gov/documents/jpl.htmlrespectively or via ENVI software.

3.6. Field observation notes

Field observation notes collected by Prof. Kim Hein in 2005 describing lithologies, structures and related identifiable geology within the Coongan area (Hein et al., n.d.). This data is not published but its use and manipulation has been granted within the scope of this study.

3.7. Software

1. ENVI 5.6 + IDL 8.8, is used for hyperspectral processing analysis including geometric correction and spectral analysis.
2. Hyperspectral Python (HypPy), is used for hyperspectral wavelength mapping, mineral maps, end-member extraction and spectral analysis.
3. Oasis Montaj Geosoft is used for the processing and analysis of the geophysical data sets
4. ArcGIS 10.8.1 is used for data integration, overlay analysis and visualisation of all data sets.

4. METHODOLOGY

The following chapter presents the overall methodology applied in this study as well as sub-steps of the methodology. The sub-steps include data collection (4.1), exploratory data analysis (4.2), pre-processing of data sets (4.3) , hyperspectral data preparation (4.4), mineral mapping (4.5), geophysical data analysis(4.6) and data integration generation of stratigraphic column (4.7).

Overall methodology

The overall approach of this study is based on hyperspectral mapping, including an integrated analysis of multi-disciplinary data sets as identified in Chapter 3. The methodology's viewpoint is to go from a low level of details to identify units and boundaries to a more detailed analysis of the mineral composition and hydrothermal alteration patterns. This approach has been selected to better answer the research questions. Table 2 shows the relationship between the various data sets and the expected output for a comprehensive insight into the study area.

Table 2: Overall Methodology for the Research

Objectives	Research questions	Data/information required	Analysis technique	Output
To identify and map different hydrothermal alteration minerals in the study area	Which hydrothermal alteration minerals can be classified using hyperspectral mapping in the study area?	Hyperspectral map, aerial photograph	Exploratory analysis, georeferencing, mineral mapping, end member extraction, comparison with spectral libraries, classification	Spectral plots, mineral maps, classified mineral map
To relate the spatial distribution of identified alteration minerals to existing geophysical maps and delineate paleosurfaces	Which paleosurfaces are distinguished, and what is their relationship with identified surface minerals	Gamma-ray, magnetic data, geological map, aerial photograph	Visual interpretation, quantitative and qualitative analysis of gamma-ray data, overlay analysis	Lithological and structural boundaries, mineral occurrence and distribution
To predict the conditions and depositional environments of the alteration minerals	Are there recognisable patterns at the paleosurfaces in terms of continuity, mineral patterns, and depth?	Aerial photograph, geological map, literature review	Visual interpretation, overlay analysis, comparison with literature	Annotated maps, interpretation
To interpret the alteration mineral and paleosurface maps applying the stratigraphical principles of geology	What is the role of the multi-disciplinary data sets in improving the understanding of the development systems in the study area?	Lithological and structural boundaries, mineral maps, geological map, field notes, geophysical data	Visual interpretation, overlay analysis	Annotated maps
To understand the relationships between the hydrothermal events and relative timing of formational processes within the Coongan greenstone belt	Which role did the hydrothermal events play in the study area, and can they be distinguished temporally?	Mineral maps, geological map	Visual interpretation, comparison of existing literature	Stratigraphic column

4.1. Data collection

Primary data for the study area includes airborne hyperspectral data, aerial photographs, geological maps, and geophysical data and accessible through ITC. The laboratory hyperspectral data is accessed through Utrecht University. No field-work was carried out during this research.

4.2. Exploratory Data Analysis

All data sets were assessed to get familiar with the data content and different characteristics of each set by employing visualisation methods in GIS software or ENVI. The initial exploratory analysis aids in understanding the data extents, variables, and identification of any errors within it. This phase revealed that the data sets whilst no bad bands were observed, they were in different projection systems and the airborne hyperspectral data needed to be geocorrected.

4.3. Pre-processing

All data sets were initially in different coordinate systems (GDA94 MGA50), and hence for the purposes of this research converted to the same system of WGS84 UTM Zone 50S. They were additionally subset to the same spatial extent to be in the confines of the study area.

4.4. AMS Airborne Hyperspectral Data Preparation

Two important factors that considered whilst processing the hyperspectral data; (1) accuracy of the georeferencing, (2) maintaining the pixel integrity of the images. For the pre-processing of the AMS hyperspectral data, georeferencing (4.4.1) was done first, followed by a cross-track illumination correction (4.4.2) and finally images were mosaicked (4.4.3). At each step, the spectral profiles had to be constantly compared to avoid any deviance from the local variation in the data.

4.4.1. Geometric correction (Georeferencing)

A geometric correction was applied to the AMS airborne hyperspectral data to create an accurate positional image of the study area. For ground control, the high-resolution aerial photo with a spatial resolution of 0.77m of the study area was used as the reference. The georeferenced images were created in two steps; (1) choosing ground control points (4.4.1.1) and warping those GCPs to the reference image (4.4.1.2). The geocorrected images were then resampled to a 5m resolution (4.4.1.3).

4.4.1.1. Selection of Ground Control Points (GCPs)

An average of 300 ground control points (Annex 1) were chosen for each of the three scenes. The selection was made by choosing unique features identifiable in both the hyperspectral image to be referenced and the aerial photo.

4.4.1.2. Warping Parameters

A Delaunay Triangulation was applied and points were resampled to the nearest neighbour to produce geocorrected images. These two methods facilitate a high accuracy of interpolation and analysis of possible irregularly-gridded data in our images.

4.4.1.3. Resampling/Resizing to 5m resolution

The warped images match the spatial resolution of the reference image and resampling might be necessary to represent the data as from spectrometer sourced. The multi-scene geocorrected images were resized to 5m spatial resolution, to maintain the pixel integrity matching the unrectified AMS data.

4.4.2. Cross-Track Illumination Correction (CTIC)

The hyperspectral images showed non-uniform illumination across the scenes. Cross-track Illumination Correction (CTIC) is a radiometric correction tool used to remove differences in illumination of images. The mean variation deducted along-track of the image is fit to a polynomial function of a preferred order and applied to remove the difference. A cross track direction across samples (along-track) polynomial order of 1 was used to retain the local variation in the data . Annex 2 shows an example of the plots of along-track values of Image_0530 before and after CTIC. The non-linear ranges before correction show the distinct illumination variations around the mean, whilst the values plot parallel to the mean after correction. To ensure that the local variation within the data and pixel integrity was maintained, spectral profiles of the images before and after correction were compared.

4.4.3. Mosaicking

A geocorrected mosaic (Figure 4), projected to WGS_1984_UTM50S covering the study area and bounded within 770417.10, 7634296.30, 777299.50 and 7623017.71 was produced. The mosaicking was georeferenced based to maintain pixel integrity. The mosaic's quality was assessed over its positioning accuracy in relation to the aerial photograph , as well as random spectral evaluation to check for the pixel integrity. The geometrical evaluation of the overall location positioning error of the mosaic is ~15m.
The level of accuracy is not as high (only ~20m), specifically to the west and north-east of the study area, due to the limited ground control points where the reference image does not cover the study area.

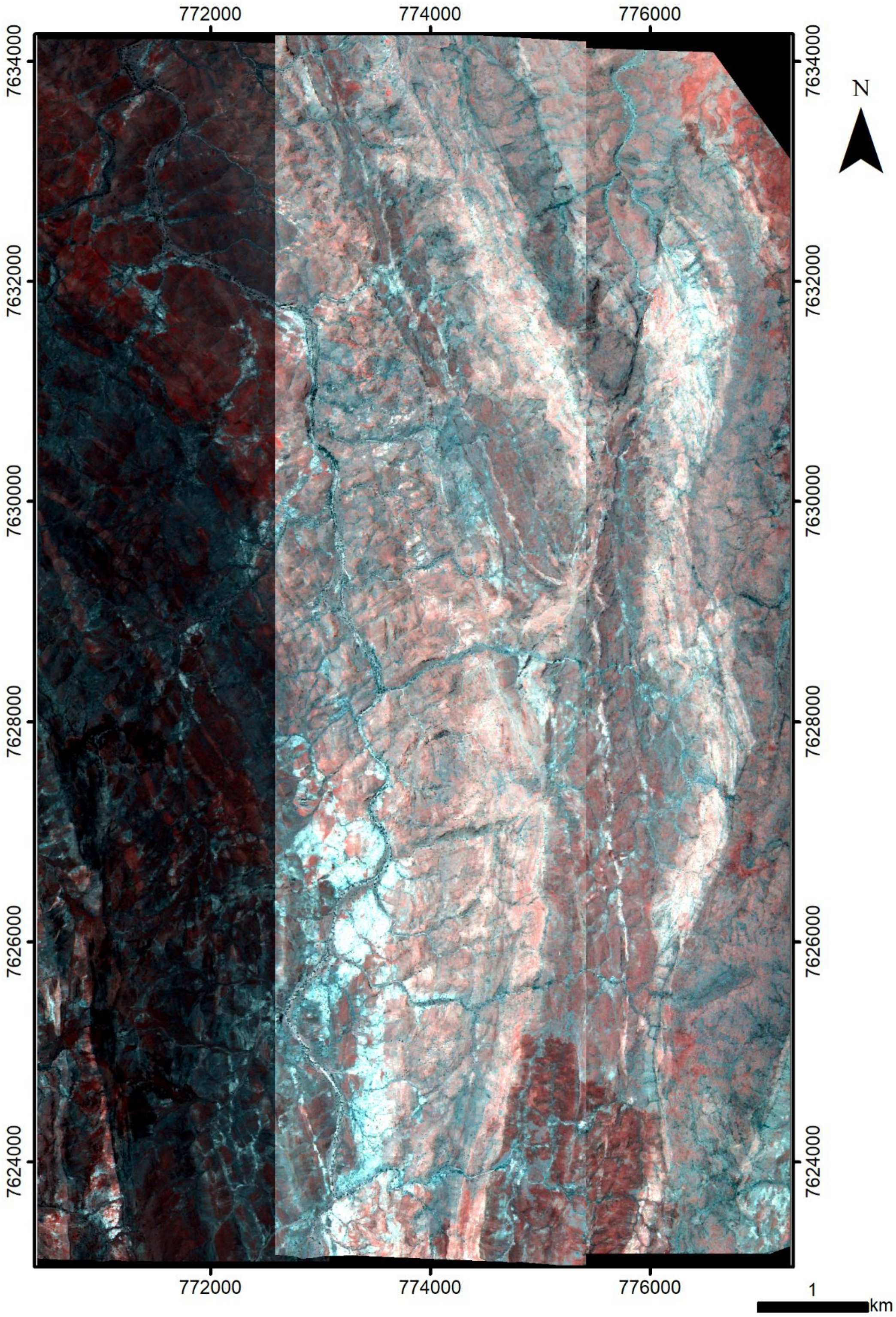

Figure 4: Georeferenced-based hyperspectral mosaic of the study area showing a non-uniform illumination across the study area

A radiometric evaluation of the mosaic proved that the CTIC improved the individual image illumination for each scene before stitching. However, the overall non-uniform illumination was still observed, particularly in the west of Figure 4, which is much darker in comparison to the rest of the image. This is acceptable if the spectral profiles of the hyperspectral data are preserved. To check and validate the pixel integrity, different spectral profiles before and after the illumination correction were compared. Figure 5 shows two random spectra with the same shape and peak positions, signifying no changes in the pixels after correction.

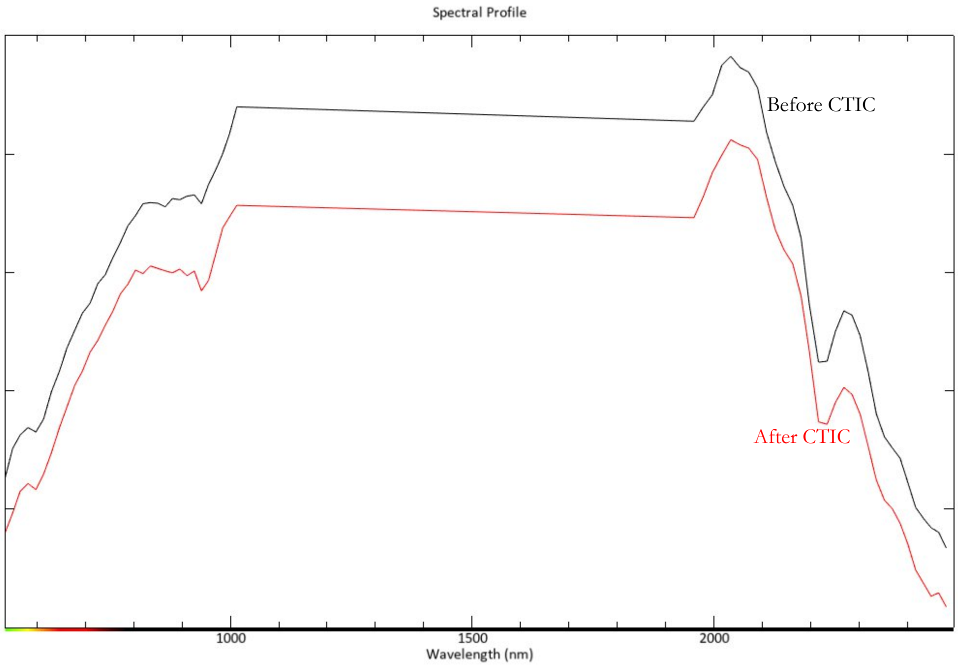

Figure 5: Spectra of mosaic pixels showing similarity before CTIC (black) and after CTI (red)

It is important to maintain the pixel integrity of the hyperspectral data as spectral analysis is dependent on image pixels (Chang, 2003; Wolfe and Black, 2018) ; any changes will not be representative of the originally acquired data, changing any interpretations. Furthermore, to offer an accurate interpretation of positioning and spatial distribution of the mineral alteration, a highly accurate geometric hyperspectral image is required (Maghsoudi Moud et al., 2021). This study assessed the accuracies between ASTER data and hyperspectral data in relation to predicting and interpreting the mineral distribution.

4.5. Mineral mapping methods using Hyperspectral Data

The mapping techniques applied to map the alteration minerals was conducted first in Hyperspectral Python (HypPy) (Bakker, 2012) and then in ENVI 5.6. Sections 4.5.1 to 4.5.3 illustrate how minerals were mapped starting from wavelength maps, mineral end-member and mineral classification to produce the mineral map.

4.5.1. Minimum wavelength Mapper

This method is based on the theory described by (Bakker et al., 2011) and (Van Ruitenbeek et al., 2014) and relies on the characterisation of the interpolated wavelength position and depth of the deepest absorption features. A further distinction between wavelengths is using colour hues within the wavelength mapper (Hecker et al., 2019). Ultimately a colour-coded map representing mineral composition, abundance and spatial distribution is generated. The wavelength position represents the feature (mineral) and the depth represents the abundance of the feature. The minimum wavelength mapper technique is done in two steps, first the wavelength of minimum followed by wavelength mapping.

Wavelength of minimum determines the wavelength position and depth of the deepest absorption features (Figure 6). The wavelength position is an interpolated wavelength through a parabola function. Additionally a continuum removal (hull quotient) is applied to highlight these individual absorption features. Three absorption feature wavelengths are determined with their corresponding depths. Figure 6 shows an example of a continuum removed spectrum with three absorption features.

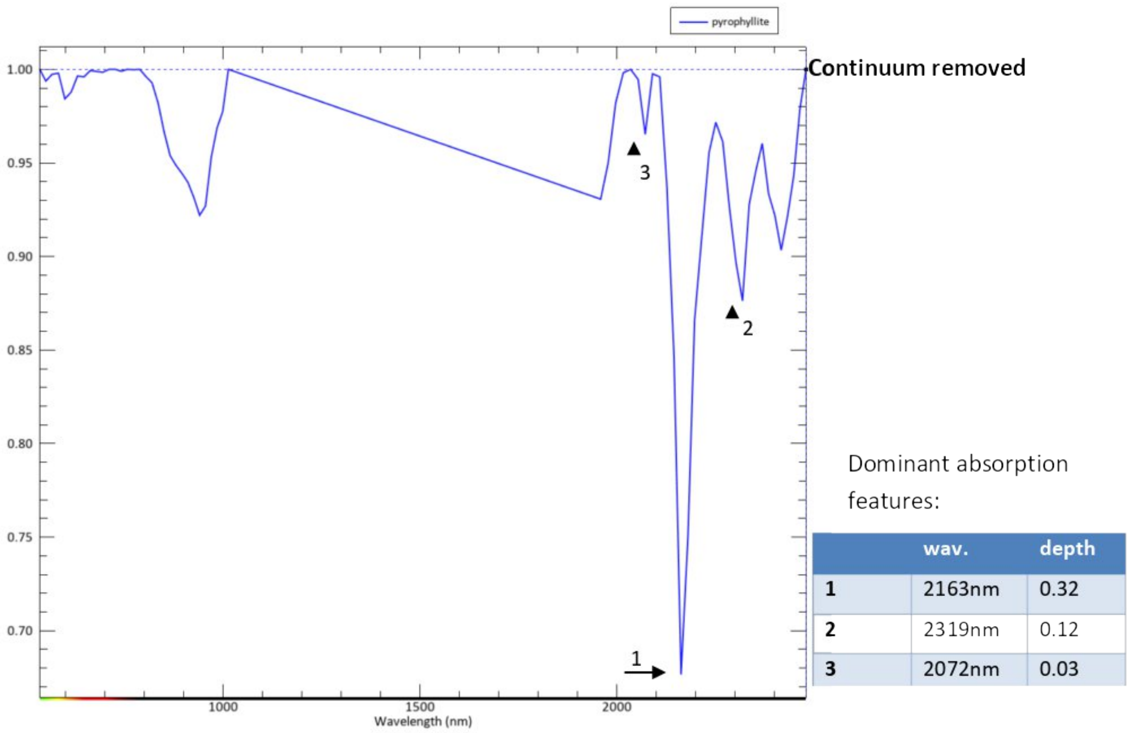

	wav.	depth
1	2163nm	0.32
2	2319nm	0.12
3	2072nm	0.03

Figure 6: Example of interpolated wavelength and depth absorption features with a continuum removal

The second step, wavelength mapping, is a hue saturation value (HSV) fusion of wavelength and depth on the wavelength of minimum product (Hecker et al., 2019b). A colour map is generated from this, where the colour is representative of a specific mineral group and the hue (brightness) determines its depth . The wavelength maps are generated in the SWIR from 2100-2400nm (Table 3) range in both steps. The range is chosen to facilitate diagnostic features in the hydroxy (-OH) groups. Table 3 shows the ranges and colour stretches applied. In the case for VNIR, a wavelength range of 500-1000nm is applied to accommodate iron oxides such as hematite or goethite.

Table 3: Table of wavelength positions of deepest absorption features of individual minerals and group minerals

Wavelength Interval (nm)	Colour stretching Interval (nm)	Molecular Bonds
800-1000	800-1000	Fe oxides (haematite, goethite)
800-1000	900-960	Fe oxides (goethite)
2100-2400	2100-2400	X-OH (X: Al, Fe, Mg, Si); CO_2
2100-2400	2250-2350	X–OH (X: Fe, Mg);CO3

4.5.2. End member Collection

The subsequent analysis involves end-member extraction either manually from the image maps, statistical algorithms or automatic methods such as spatial-spectral endmember extraction (SSEE) ((L3 Harris Geospatial, n.d.). Each end member represents a signature class identifiable in the map and that can be compared to known spectral libraries such as USGS or JPL spectral libraries. Main absorption features of the spectra and general shape of the spectra are deterministic. This helps in identifying and assigning spectra to a specific mineralogical group with the classes determined. In this study end-member extraction was manual and image pixels (spectra) were picked for the different classes in the wavelength map. In HypPy, the original image is loaded as a shadow image and the spectra is taken from this shadow image underlying the wavelength map. Spectra is also taken from RGB composites of the wavelength maps for improved contrast. Scatterplots (Figure 7) of the wavelength map in the spectrum ranges can also be used to analyse dominant features and pick out spectra identified from the peaks in the graph.

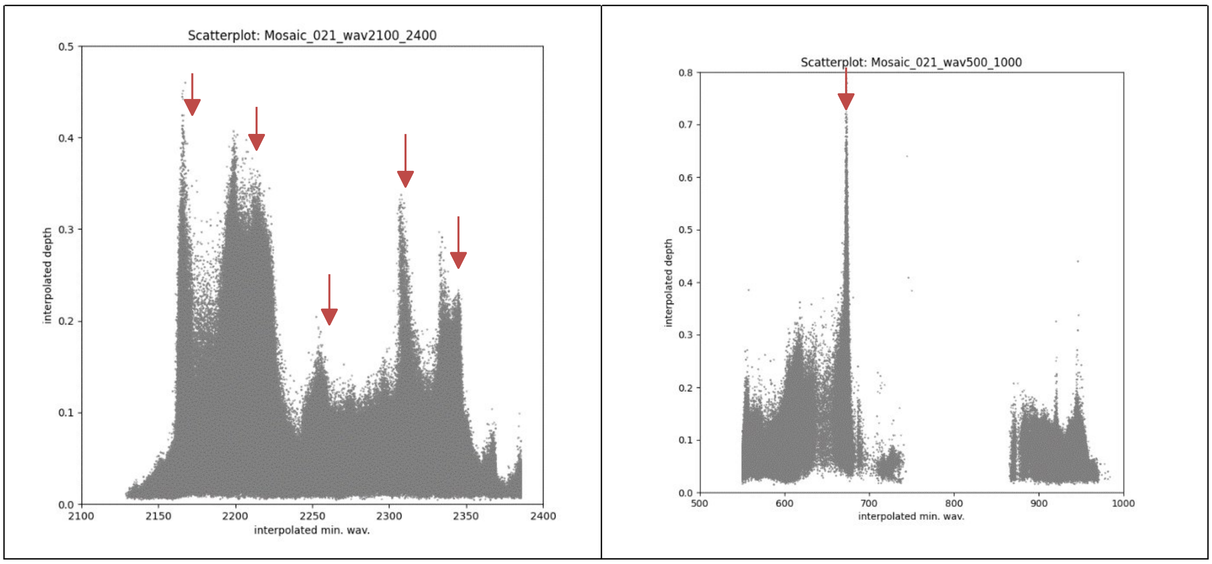

Figure 7: Graphs of minimum wavelength scatterplots of the hyperspectral mosaicked images for the SWIR and VNIR with the red arrows showing peaks of dominant absorption features

Approximately five similar spectra are chosen for a class and an average of the spectra is calculated and retained as representing each class. The wavelength map can also be viewed in an RGB composite for a better analysis and to aid in picking spectral end members. The spectra can be displayed as images and values and saved as a spectral library for further analysis with known spectral libraries.

4.5.2.1. Analysis with Spectral Interpretation Field Manual (GMEX)

The spectra collected from the wavelength map are unknown minerals and further analysed using the spectral interpretation field manual (GMEX) to identify them. This method and strategy as described in the AusSpec mineral spectral library (GMEX, 1997; GMEX, 2008) was applied to the picked spectra. Using the characteristics of diagnostic absorption features stated in the guide, most of the spectra were identified. The shapes of features were also incorporated to discriminate between closely similar mineral spectra. However, a full identification was impossible in some cases owing to insufficient spectral resolution, overlapping absorption features or artefacts in the spectrum .

4.5.2.2. Comparison with USGS Library

Spectral libraries are collections of spectra of different surface materials, measured by renowned research institutions under laboratory conditions with excellent spectrometers. Subsequently, the identified and unidentified spectra were resampled to the USGS spectral library, the usgs_v7 library for minerals and vegetation was used. This strategy was to accommodate the limitations in the full identification of some spectra as well as validate the identified minerals. Again the unknown spectrum was assessed manually and compared with the known spectrum (Figure 8) on the position and shape of the diagnostic absorption features.

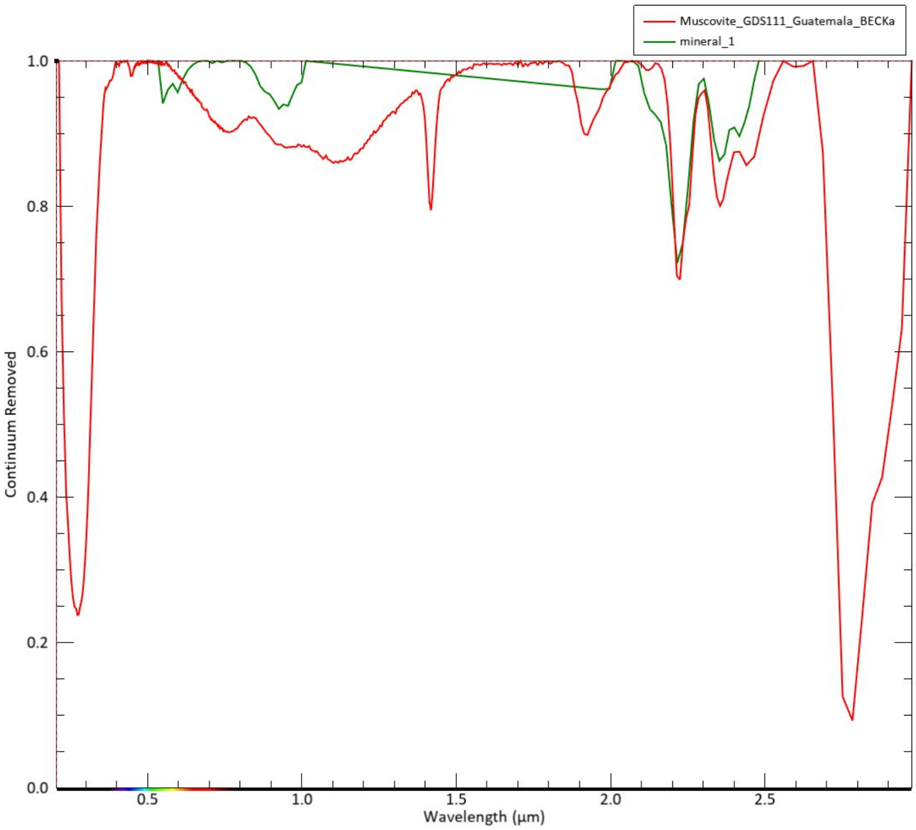

Figure 8: Example showing comparison of spectral plots of USGS mineral vs unknown hyperspectral image pixel

4.5.3. Decision Tree Mineral Classification

With the minerals in the wavelength identified, the next step is to classify those minerals and produce a classified mineral map. A decision tree classifier executes successive operative stages that are based on a binary decision system and puts image pixels into set classes. The decisions are governed by mathematical or logical expressions , with each expression defining a class. These expressions and thresholds are based on the wavelength position of the first deepest feature. Subsequently, the wavelength position of the second and third deepest features are also used in the classification. To determine the thresholds, the wavelength map scatterplot (Figure 9), separation of classes is based on the peaks and thus wavelength positions of the absorption features. The limits of each major class are determined using the spread and distribution as highlighted by the red lines in the scatterplot and corresponding candidate mineral analysis. The classes can be divided as many times by inputting new expressions on different nodes The decision tree classification is iterative with continual removal and endmember refinement. These iterations are influenced by the candidate minerals based on the analysis and interpretation of the GMEX and USGS spectral libraries, radiometric data and geological data within the study area. Ultimately a classified mineral map was derived.

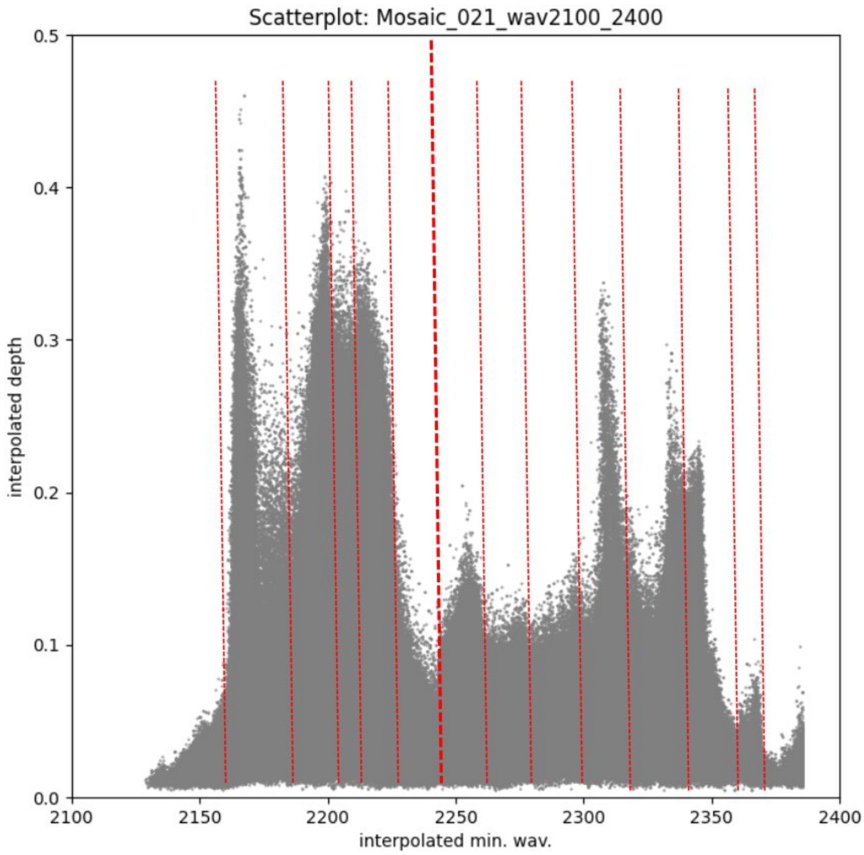

Figure 9: Histogram of wavelength image mosaic between 2100-2400nm with the red line showing separation of wavelength positions used in decision-tree classification

From the classified mineral map, a quantitative analysis was carried out to quantify the mineral distribution for each lithological unit. A spatial analyst tool; tabulate area was used to calculate the area for each pixel in relation to its spatial distribution. This area was then converted to percentage and tabulated.

4.6. Geophysical Data Analysis

The geophysical data is important in identifying and understanding the zonation of geologic features, that is, identifying the contacts and surfaces in the study area. The gamma-ray and magnetic data are already calibrated and corrected for atmospheric and sensor effects. Enhancement filters were applied on the geophysical data layers using Geosoft Package to improve analysis and interpretation. Both quantitative and qualitative interpretations were applied on the data. Boundary vector layers were created using ArcMap to delineate lithological and structural variation based on the geophysical data grids. Overlay analysis of the geophysical data sets and the hyperspectral mineral maps was done to understand the study area's overall lithological, mineral, and structural relationships. The analysis was done using both hardcopy maps and software. Annotating using paper maps was to simplify the different datasets and acquire information faster and more efficiently. The software was then subsequently used to refine the annotations and have them in a layer format for easy use and access.

4.6.1. Radiometric data (Gamma Ray)

The geophysical data was not in element concentration and thus a conversion was done. Using grid math in the Geosoft Software, radioelement grid conversions from counts per second (cps) to parts per million (ppm) applied the following equation:

$$\boldsymbol{C = N_s / S},$$

where :

C = the apparent concentration of the element (K percentage, eU ppm, eTh ppm)

Ns = the count rate for each window (from the attenuation section)

S = the broad source sensitivity for the window (provided in the survey report by Lawrence and Stenning, 2009).

After conversion, radiometric ternary diagram was created from the individual Potassium(K), Thorium(Th) and Uranium (U) data. The ternary Image is a ratio of K, Th, U with the Total count map used as shading grid. A colour legend based on this image was also created with Red, Green and Blue (RGB) representing K-content, eTh-content and eU-content respectively. Based on the ternary image, a vector layer was created in ArcMap , delineating the visually observed lithological variations in the gamma-ray data. These contacts and boundaries were then overlain with the hyperspectral and geological maps for further interpretation. Additional quantitative analysis was performed to quantify the radioelement (K, eU, eTh) compositions and further interpret the implications of the abundance of the radioelements. An analysis of the geologic and geo-environments was also done using the potassium-thorium ratio and uranium-thorium ratio. These were intended to determine potassic enrichment and uranium migration within the study area to determine the forming and alteration conditions.

4.6.2. Airborne Magnetic Data

The magnetic data (magnetic anomalies) was used to identify lineaments (faults, fractures, dykes or feeder zones), as well as to explain the (control of structure on mineral distribution)stratigraphy and relationship to exhalative horizons. The Total Magnetic Intensity (TMI) was first Reduced To Pole (RTP) which is the magnetic pole (Rajagopalan, 2003) (Baranov and Naudy, 1964) with no effects of the induced magnetisation on the anomalies. Filtering and enhancement are applied to the RTP to obtain data that is more resolved and highlight contrasts and features clearly. Products from this filtering were: the Analytical Signal, First Vertical Derivative, and Tilt Derivative. Also the Regional and Residual Effects were separated. Shading grids were included to sharpen the images for better visualisation. In conjunction with the aerial photos, these grids were used to identify the lineaments and digitize them into vector layers that were used for further interpretations.

4.7. Data Integration and Interpretation and Stratigraphic Column

The overall strategy in answering the research questions is to analyse the hyperspectral information and make interpretations integrating geological, geophysical, laboratory and field data. Building up interpretations from the various integrated data sets also allows for a synopsis from a larger framework to a more localised one, giving a more comprehensive and detailed understanding of the study area. The interpretations of processed outputs was carried out in a stepwise approach, starting from low resolution to high-resolution data. The interpretations were then used to construct a stratigraphy column.

Using the 1:100 000 geological map as a baseline, the already mapped lithological formations, mineralogical compositions and timing were identified within the study area. Digitised vector layers were used to represent these lithological boundaries. The output from the geophysical data from the geophysical data was also overlain with the lithological boundaries. These added details of the chemical variations within the formations as well as paleosurfaces, structural controls and any exhalative horizons identified in the study area. Subsequently, the hyperspectral wavelength image and classified mineral map were overlain with the lithological boundaries to establish any evidence of hydrothermal alteration. A correlation between the altered minerals to the lithological units was made. The analysis was to identify any indications of alteration and confine them to their respective formations. Non-altered units were also identified and any other significant minerals within the units highlighted. Furthermore, the spatial patterns and distribution of the indicated alteration was evaluated. The timing of alteration, paleo-surfaces and paleo-environments were also discussed and interpreted. Basis for interpretations was also extracted and used from the field notes of Kim Hein. Ultimately, from the data integration and interpretations made on the hydrothermal systems, a stratigraphic column was created. This stratigraphic column was hand-drawn. The stratigraphic column highlights the indicated altered and unaltered units with descriptions of alteration events and their relative timing.

5. RESULTS

The chapter presents the research findings in line with the research objectives of the study. Additionally, it also includes interpretations and discussions on these findings. The chapter starts with presenting the radiometric results that describe the classification of the main lithological units in the study area, followed by the interpretation of the magnetic data that gives indications for the structure controls in the area and ending with the detailed mineral map using the hyperspectral data.

5.1. Radiometric Data (Gamma Ray)

Pseudo colour images for the Total Count(TC) (Figure10a), individual radioelements K (Figure 10b), equivalent of eU (Figure 11a) and eTh (Figure11b) and a ternary image map (Figure11) were produced from gridded values with a histogram equalisation. The analysis of these images indicated the surface chemical variation within different lithologies and delineated surface lineaments in the study area. The variation shows highest concentrations of radioactive elements (more than 3.2% K, 6.20 ppm eTh and 2.80 ppm eU) are concentrated in the central part of the study area. Low to moderate concentrations are observed to the west and east of the study area (0.1-0.7%K, 0.9-2.7 ppm eTh and -0.1 to 1.2 ppm eU). Such concentrations in the study area are interpreted as signature of a more felsic area in the central parts of the study area, bounded by a more mafic region in the west and to the east a combined felsic-mafic region.

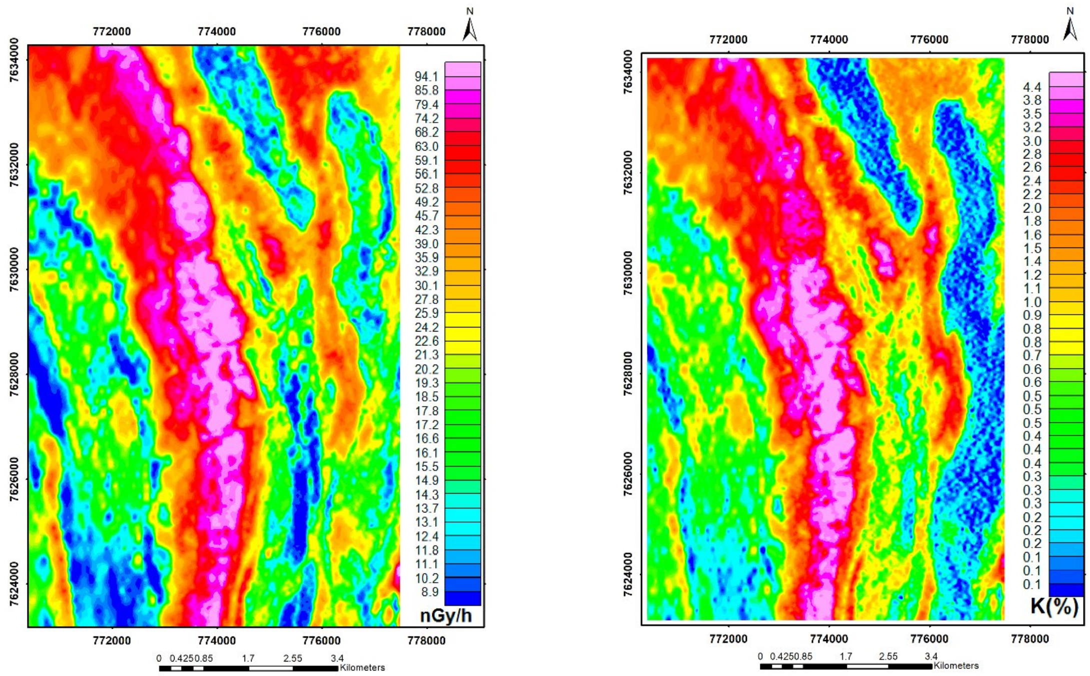

Figure 10: The figure show radiometric element concentration grids of (a) Total Count, (b) Potassium(K%)

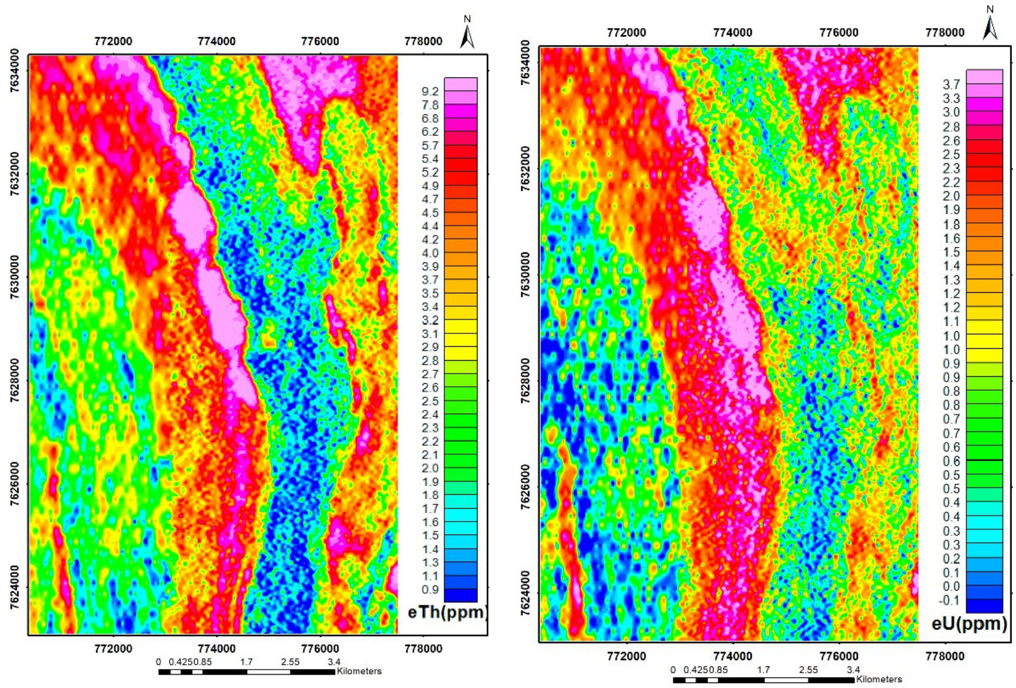

Figure 11: The figure shows the radiometric element concentration grids of (a) Uranium (eU/ppm), (b) Thorium) eTh/ppm)

The radiometric maps, specifically the ternary image was used to separate the radioelements over each lithologic unit. The legend in Figure 12 identifies the dominant radioelements across the study area with red for K%, green and blue for eTh and eU respectively. A high concentration in all three elements is usually signified by a bright almost white colour.

To differentiate the lithological contacts and units (Figure 12), each bounded unit was given a label G with a preceding integer. The contacts were labelled based on these unit labels for easy identification. Some units with similar variation are represented with the same label. Figure 12 outlines eleven (11) major units (G1-G11) and five (5) minor units (G12-G15). The centre units (G2,G3,G5) of the study area is marked by a high enrichment of radioelements with significant potassium content. To the west, G1 is dominant with a moderate thorium content; a pattern similar to the minor units G12. A very bright unit (G11) also appears in the west, with high uranium content. The northeast also shows uranium enrichment in G8, with the east predominantly thorium content and moderately elevated uranium content.

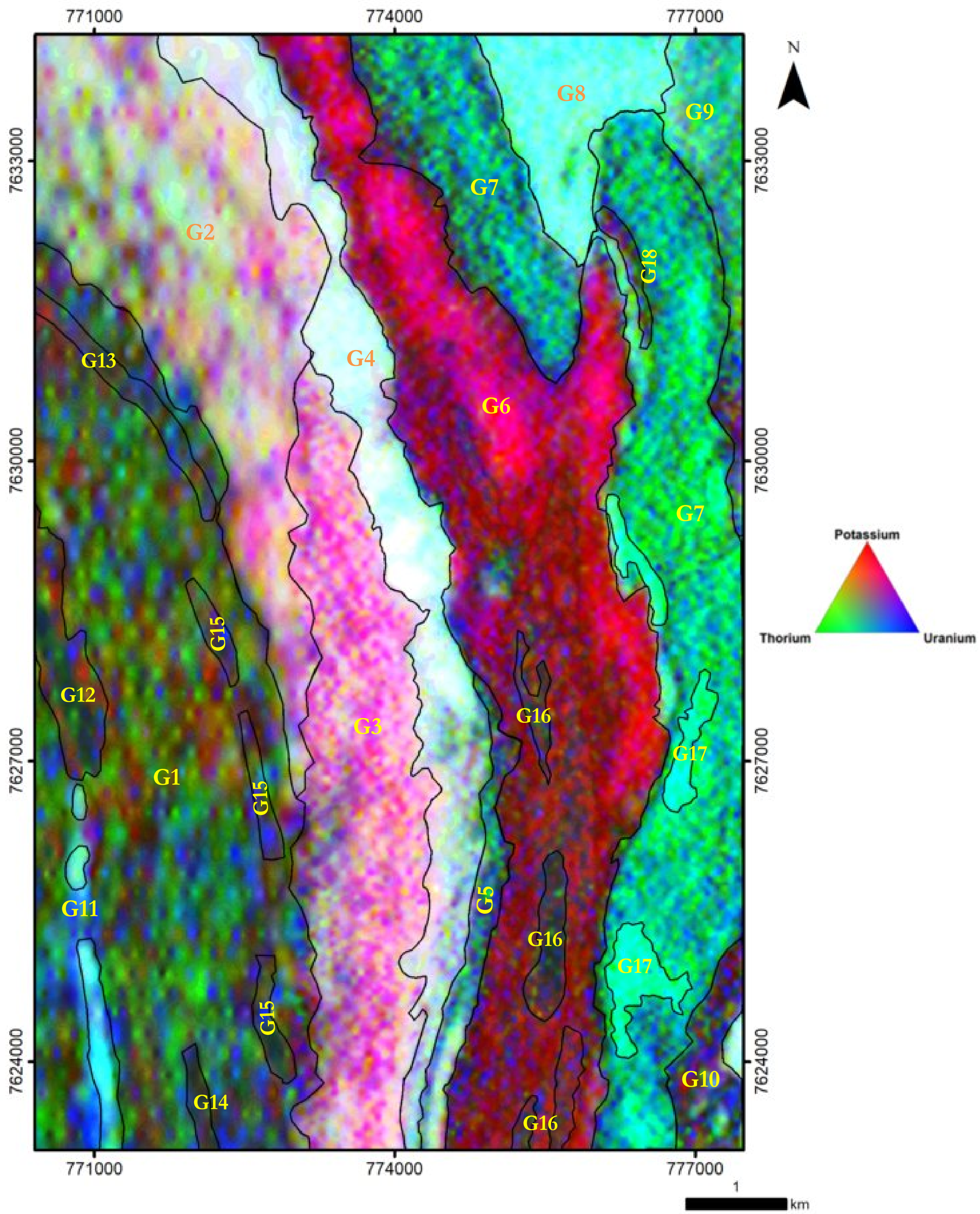

Figure 12: The figure shows the ternary image of K, eU and eTh overlaid with the black polygons showing the derived lithological contacts and units

The units described above represent the chemical variation across the study area. Radioelement concentrations derived from Figures 10 and 11 in relation to each unit are described in Table 4.

Table 4: Radioelement concentration per defined unit

Code	K%	eTh(ppm)	eU(ppm)	Total Count	Description	Interpretated composition
G1	0.2-0.6	1.8-3.2	-0.1-0.9	8.9-27.8	Low radioelements, relatively high eTh-content	Mafic
G2	1.2-2.8	3.4-7.8	1.2-2.6	35.9-63.0	Relatively high radioelements, moderate elevation of K	Mafic and felsic
G3	2.8-4.4	2.8-6.8	1.9-3.3	35.9-94.1	Relatively high radioelements, with elevated K	Felsic
G4	1.8-4.4	5.7-9.2	2.6-3.7	63.0-94.1	Very high radioelements content of all 3	Felsic
G5	0.4-0.6	1.9-4.0	0.5-2.0	14.3-56.1	High eU with low eTh	Mafic
G6	0.4-3.5	0.9-2.5	0.4- 2.0	8.9-68.2	Very high K-content	Mafic and felsic
G7	0.1-0.3	2.6-5.7	0.4-2.0	8.9-21.3	Low radioelements, high eth with moderate eU enrichment	
G8	1.0-1.6	5.7-9.2	2.0-3.7	35.9-68.2	High radioelement enrichment of all 3, with elevated Th-content	Felsic
G9	0.5-0.7	3.9-5.4	0.9-1.9	24.2-32.9	Th-rich with a moderate eU enrichment	
G10	0.1-0.3	0.9-2.6	0.1-1.3	8.9-14.9	Low radioelement, with elevated eU and moderated eth	Mafic
G11	0.8-1.6	3.4-6.8	2.0- 3.3	24.2-56.1	High radioelement content of all 3, with elevated eU	Felsic
G12	0.1-0.3	0.9-1.7	-0.1-0.3	8.9-13.7	Low radioelement, with Th enrichment	Mafic
G13	0.3-0.6	0.9-1.7	-0.1-0.5	8.9-16.6	Low radioelement, with Th enrichment	Mafic
G14	0.3-0.6	1.9-2.6	-0.1-0.5	8.9-12.4	Low radioelement, with Th enrichment	Mafic
G15	0.3-0.7	0.9-2.7	-0.1-0.5	8.9-16.6	Low radioelement, with Th enrichment	Mafic
G16	0.2-0.5	0.9-1.8	-0.1-0.3	8.9-11.8	Low radioelement enrichment, with slightly elevated Th-content	Mafic
G17	1.8-2.4	5.7-9.2	1.2-2.3	27.8-42.3	High radioelement enrichment, with high Th and U content	Mafic and felsic
G18	0.2-0.5	1.8-2.4	0.4-1.2	8.9-11.8	Low radioelement enrichment, with slightly elevated Th-content	Mafic

The contacts between these units are defined based on the geophysical radiometric data variation across the study area. In general the lithological contacts are easily distinguished by their radiometric colour; however, a distinction can also be made based on the transitional nature between the units (Figure 13). Contacts G1-G2, G2-G4, G3-G4, G4-G6,G6-G7,G7-G8, G7-G10 and G11-G1 are sharp and marked by a distinct change in colour, i.e. radioelement distribution. From the west, into the potassic rich centre, the unit boundaries are less sharp. Whilst the G1_G2 is a sharp contact in the north (Figure 13), a gradational transition between the two units is observed towards the south, marked by an increase in potassium content. G3_G4 and G4_G5 in the south also show a gradual change between the contact with a decrease in potassium content across the study area towards the east.

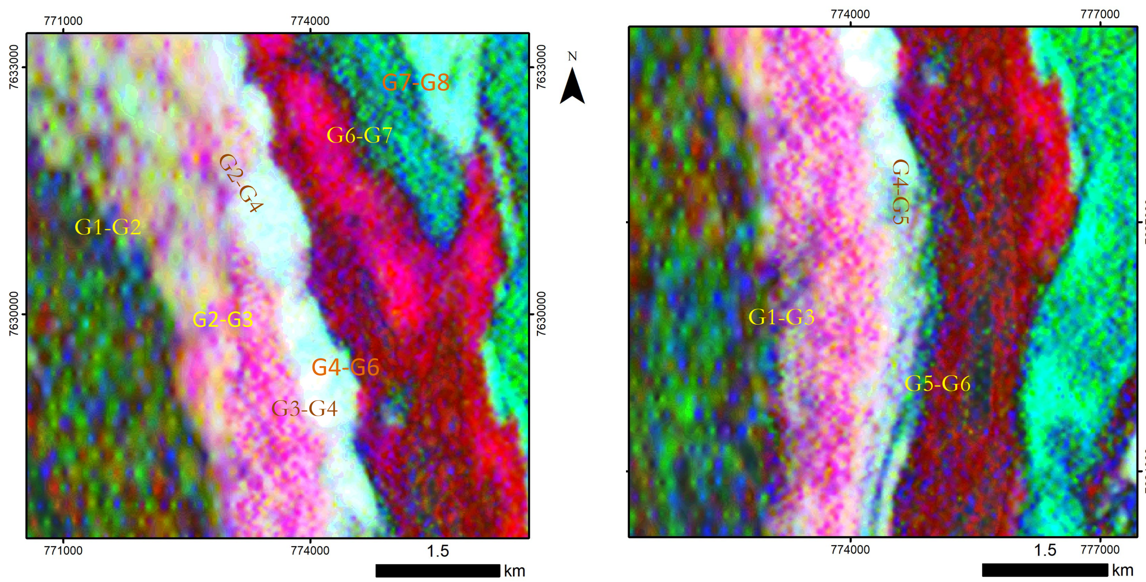

Figure 13: The figure show two zoomed scenes of the ternary images highlighting the sharp (e.g G4-G6 in (a) and G5-G6 in (b)) and gradational nature (e.g., G1-G2 and G2-G3 in (a) and G1-G3 and G4-G5 in (b)) of the contacts.

K/eTh ratio

The K/eTh ratio is used as an indicator of potassic enrichment areas related to hydrothermal alteration. In most rocks the ratio K/eTh is usually constant and thereby any high concentration can signify hydrothermal alteration and mineralisation. In the study area, Figure 14 shows four anomalous potassium domains. Domain 1 which can be related to named unit G6 has extremely high K/eTh values reaching 1.5. Domains 2,3 and 4 coincide with named units G4,G2 and G3 respectively as with ratios exceeding 0.4. Scattered anomalies are also observed in the far west of the map.

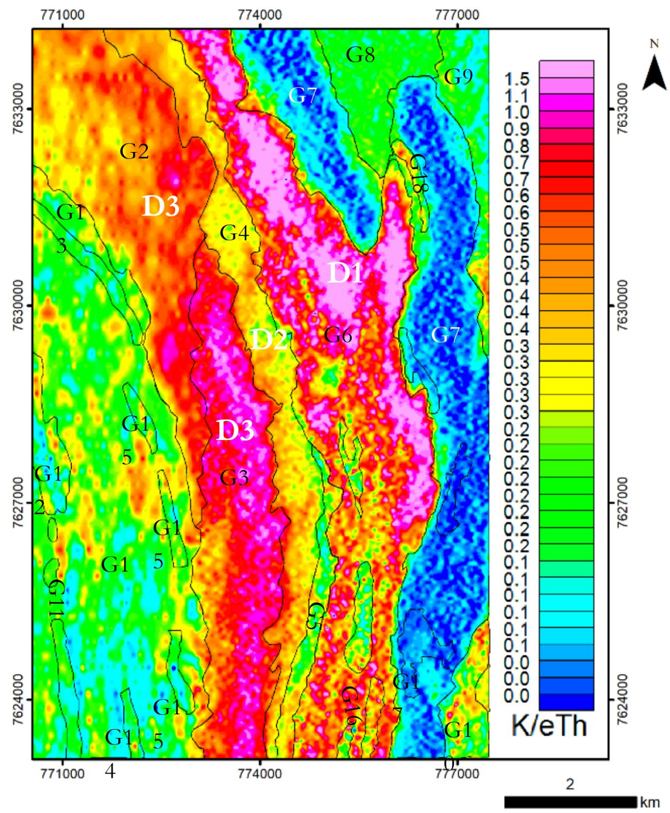

Figure 14: Ratio image of K/eTh showing the domains with high content

5.2. Aeromagnetic Data

The aeromagnetic data were used to enhance the classification of the lithologic units based on the magnetic signal and to add the structural details to the interpreted features from the gamma-ray. Lineament, structures and magnetic anomalies were delineated based on the reduced to pole (RTP) map (Figure 15) and are shown in relation to the interpreted units. The total magnetic intensity (TMI) within the study area generally increases in the centre towards the east of the map (Figure 15a). Very high anomalies (up to 65812nT) are observed stretching from the NE to SE. The separation of the study area into regions of high magnetics are surrounded by moderate-low magnetic regions implying zones of contact and deformation.

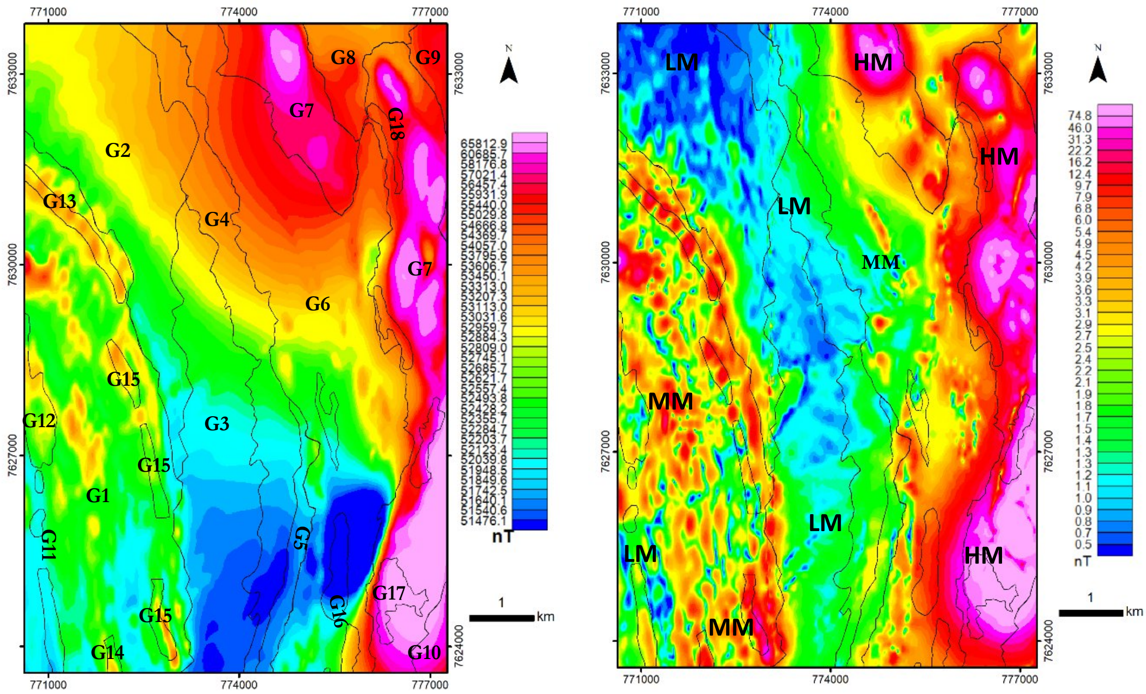

Figure 15: (a) Reduced To Pole (RTP) map shows the total magnetic intensity, (b) Analytical Signal map shows the variation in the magnetic zones associated with near-surface anomalies

Filtering and enhancement procedures were applied to the RTP for further analysis and interpretations. The analytical signal (AS) map (Figure14b) highlights the variation in magnetic anomalies as well as discontinuities across the study area. Positive and negative peaks of magnetic susceptibility are defined by AS into three different zones. Low to relatively low (LM) magnetic zones (0.5 to 2.4nT), moderate magnetic zones (MM) with a gradient of 2.4 to 6.0nT and a high magnetic zones (HM) of gradient of 6.0 to 74.8nT. The HM zones are mostly constrained to G7, and might be significant of banded iron formations (BIFs). The MM zones (G1,G12,G15, G6) show a significant high relief associated with mafic and exhalative horizons. The dislocations imply structural fracturing or metamorphic veins. Units G2, G3, G4 and G5 are LM zones with low relief, which is associated with felsic units. G2 shows some high relief in the extreme NW which implies a mixture of mafic and felsic material.

A separation of the deep and surface features a s represented by the Residual Effects (RE) in Figure 16a, highlights high magnetic anomalies (bright regions) mostly constricted to the east and west of the map. The comparison of these surficial features with the first Vertical derivative (VD) (Figure 16b) and AS map, shows similar patterns in the magnetic anomalies. To the west of the study area, the RE and VD show significant horizontal bedding marked by a high frequency of NE-SW fracturing with NE-SW cutting across the unit. These features are interpreted to be constricted to unit G1. The high relief observed also in these areas suggests the presence of mafic material as compared to the areas with less relief across the study area.

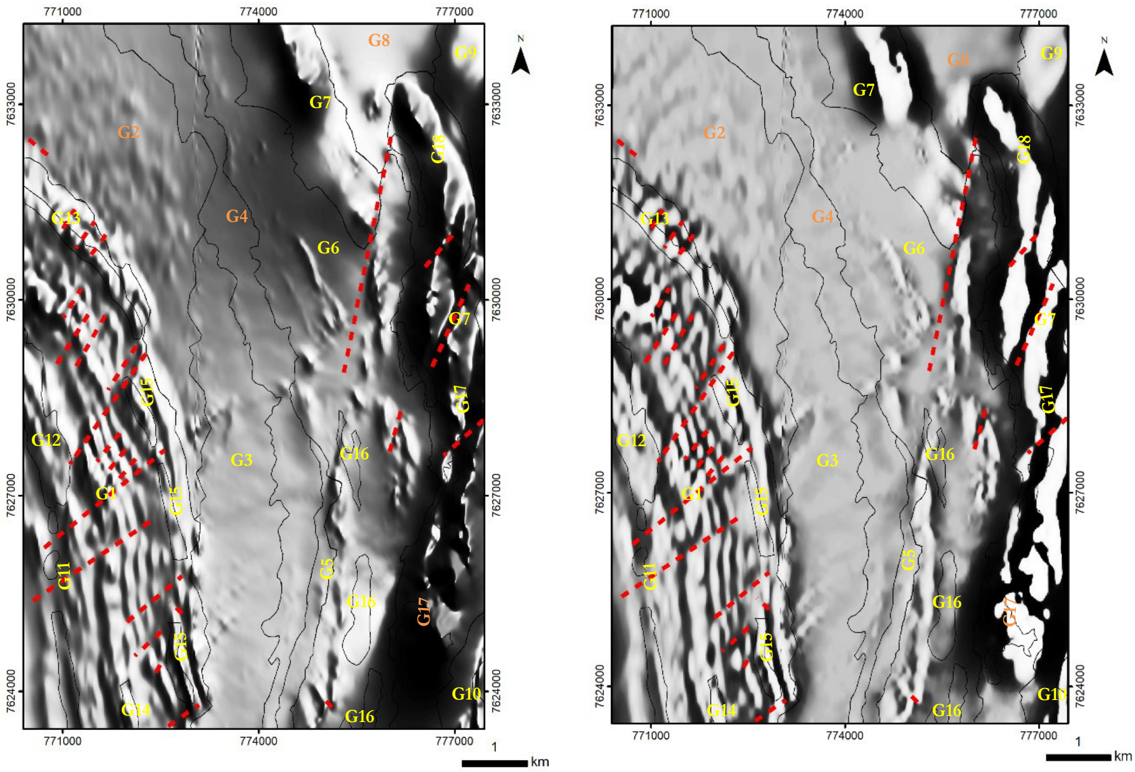

Figure 16: (a) Residual effects, (b) Vertical derivative, highlight near-surface lineaments and structures as red dashed lines in the different units

G6 and G7 appear to have been displaced by a continuous fault line. Additionally, the linear bright structures constricted to unit G7 are interpreted to be either BIFs or exhalative horizons based on their high magnetic footprint in the AS, RE and VD respectively. Dislocations of the BIFs are also apparent with some fractures also observed. The presence of some irregular high magnetic anomalies within units G6 and G8 can be indicative of exhalative horizons.

The analysis of these geophysical data sets gives additional information on the study area. The structure and magnetic footprints imply the existence of iron-rich zones (exhalative horizons) and possible veins (fractures) that acted as fluid pathways within the study area. Crossing-cutting structures indicate multiple episodes of faulting or deformation.

5.3. Minimum Wavelength Mapper

5.3.1. Wavelength Mapping : SWIR Wavelength Image

In order to identify the mineral occurrences within the Coongan, the minimum wavelength mapper was applied to the airborne hyperspectral data in the 2100-2400nm range. The minimum wavelength image produced in the first step of the technique shows the interpolated wavelengths of the deepest feature and associated depths. Three (3) deepest absorption features are identified within the minimum wavelength image and represented by a total of six (6) bands (0-6). These bands identify each deepest feature by a sequential band pair such as band 0 and band 1 represent the wavelength and depth respectively of the first deepest feature and so forth. This minimum wavelength image (Figure 17), is viewed in different stretches for better visualisation and contrast of mineral variation. Figure 17, shows a false colour composite stretch of the first (1^{st}), second (2^{nd}) and third (3^{rd}) deepest features acquired across the hyperspectral image. Whilst there is no influence of depth in the features, the contrast indicates the shallow absorption features that would otherwise not be highlighted.

The colour composite visualisation of the wavelength of the deepest absorption features shows a dominant mineral in green, with blue and red representing minerals restricted to the east and west respectively. The different colours and contrast in the wavelength image suggest variation in feature wavelength positions and in turn mineralogical compositions across the study area. Green dominates the study area with a larger composition in units G2,G3 and G4. The associated wavelength position for the green hues ranges from 2194-2220nm which is typical for white micas. To the west of the study area (mainly G1), red and orange are dominant with wavelengths of 2336nm and 2351nm respectively. This is typical for mafic minerals such as calcsilicates, chlorites, carbonates and amphibole. The red and orange also occur in a layered pattern within G1 and this pattern also repeats itself in G6. This can be interpreted to be a cyclic event of mineral deposition. The blue colours range from cyan to deep blue. The cyan with wavelength position of 2194nm would suggest pyrophyllite.

Because the red, green and blue (RGB) wavelength image only highlights the wavelength position of the deepest features, and does not account for their associated depths, only the mineralogical composition and spatial distribution of the minerals can be interpreted. This gap in information is solved by the wavelength map for which the depths of deepest features which represent mineral abundance are determined.

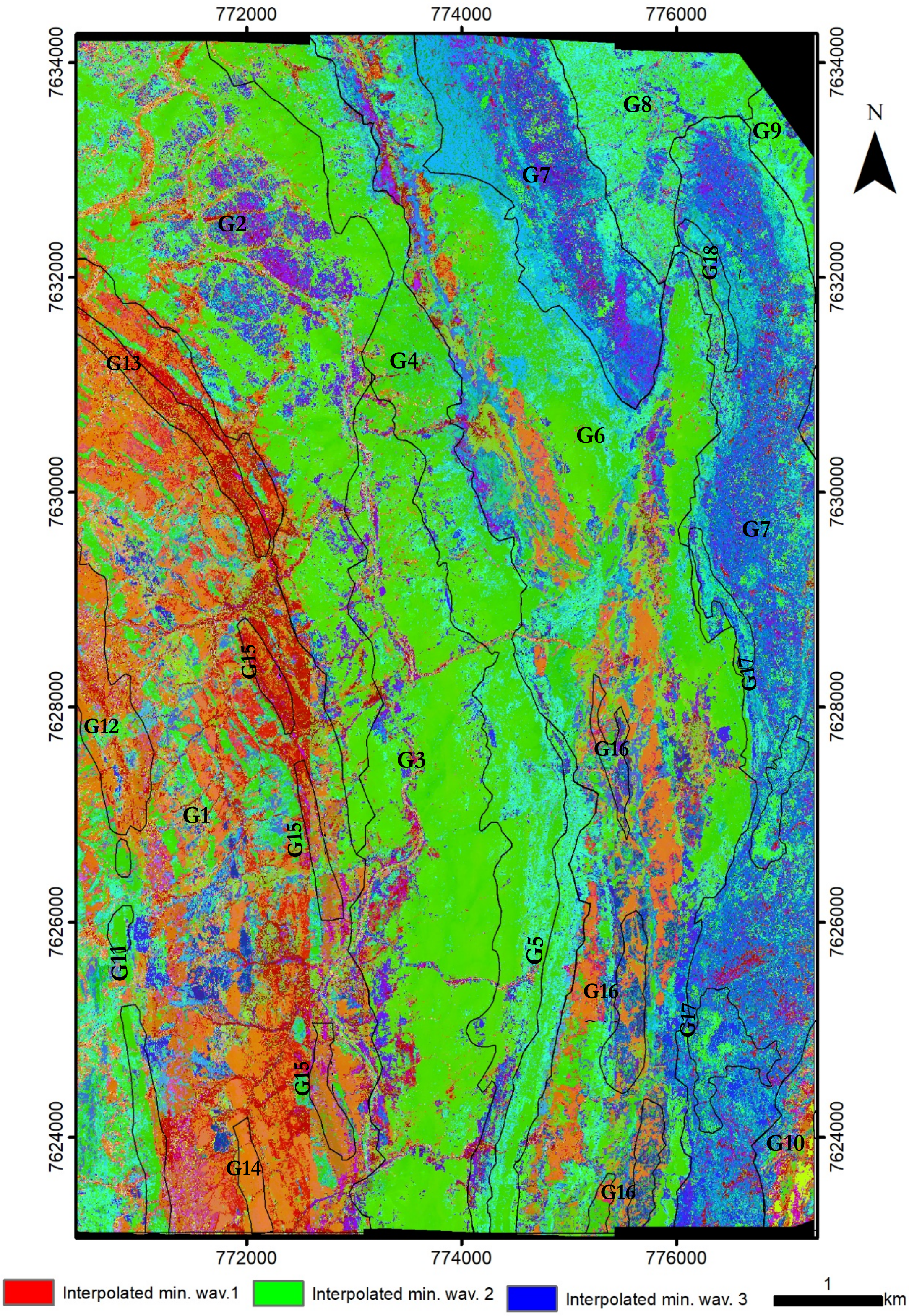

Figure 17: Pseudo-colour(RGB) composite of interpolated minimum wavelength (min.wav) between 2100-2400nm showing mineralogical variation across the study area overlaid by black polygons of the lithological units' contacts.

5.3.2. Wavelength Mapping : SWIR Wavelength Map

Additionally, the minimum wavelength image was used to create a wavelength map. The map is hue-saturated value (HSV) fusion of interpolated wavelength and interpolated depth of absorption features. The resulting wavelength map Figure 18 gives an overview of spectral variability within the study area. From the wavelength map, the study area can be divided into three (3) main regions of different absorption features. The green colour dominates the wavelength map, representing absorption features around 2200-2250nm interpreted to be Al-Mg clay minerals. Deep absorption features around 2300-2350nm (magenta and brown) are also observed in the west of the study area and are most likely associated with Fe, Mg, Al-silicates and carbonates, intercalated with some features in the 2200nm range (green colour). In the NE of the study area, a bright cyan colour representing an absorption feature around 2150nm are easily distinguished and could be Al-clay minerals as well. The east of the study area is mainly covered in shallow features (dark green and black). Smaller and similar zones based on colour and hue are observed, in a cyclic sequence across the study area. The deep pink colour is also observed in the centre of Figure 18, embedded within the majority green. Additionally, the shallow absorption features are dark (black) whilst deep absorption features show high contrast and bright colours. Observations in the wavelength map of the wavelength positions of the absorption feature match the distribution highlighted in the histogram in Figure 9.

The different colours in a wavelength map symbolise the varying absorption feature wavelengths and thus representative of a particular mineral or a group of minerals. Additionally the depth of the feature represents relative mineralogic abundance (Bakker et al., 2011; Hecker et al., 2019a). The degree of saturation of the colours maps is depth-dependent; the deeper the absorption feature, the higher the saturation and vice-versa. Thus the variation in observed hues within the same colour groups such as green in Figure 19 is due to different depths. Thus the wavelength map has all the wavelength and depth positions of the deepest features and highlights, mineralogic composition, mineral abundance and spatial distribution.

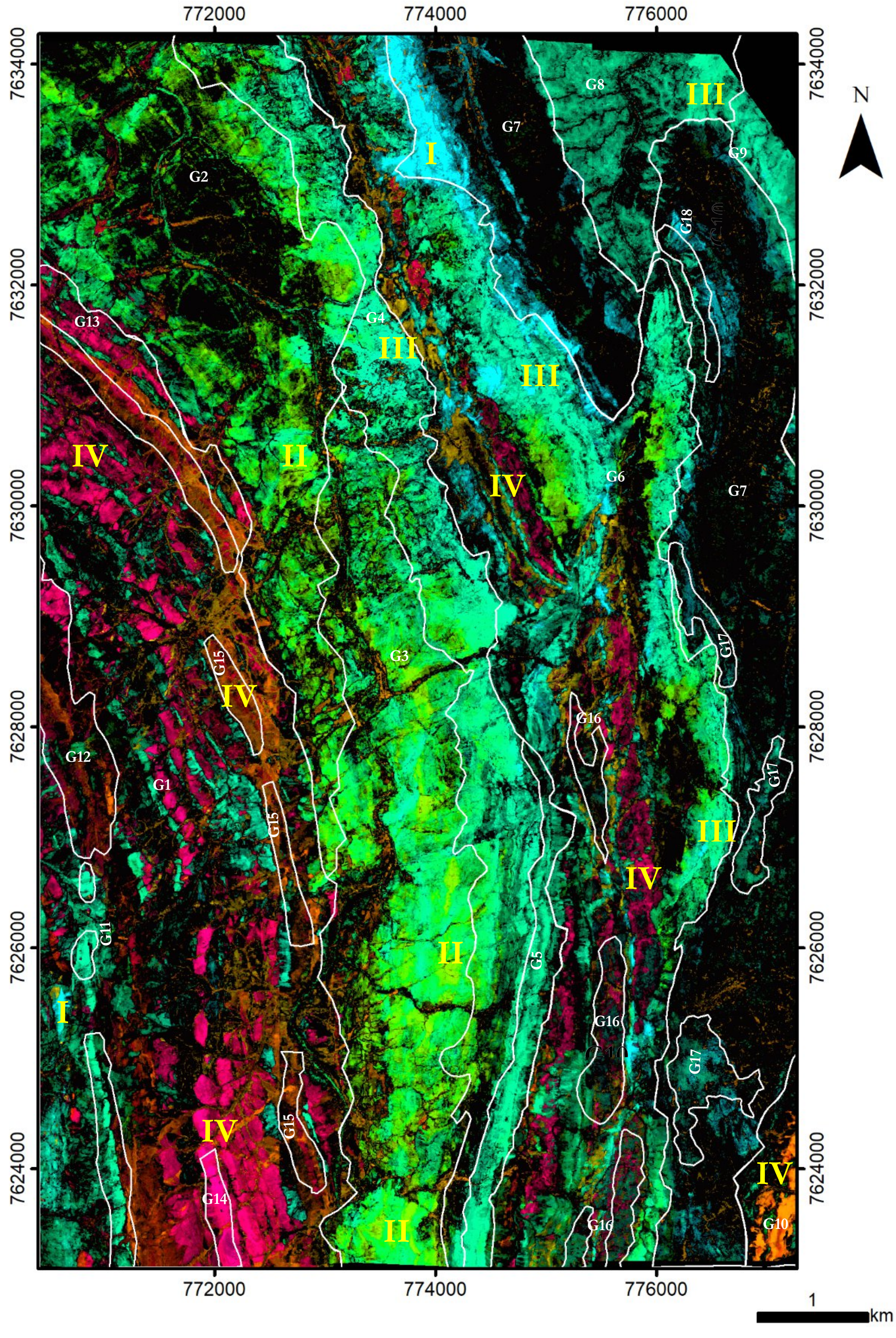

Figure 18: Wavelength map between 2100-2400nm showing variation of the deepest absorption features and their relation to the division of the study area overlaid by white polygons of the lithological units' contacts

5.3.3. Wavelength Mapping: VNIR Wavelength Image

Subsequently wavelength mapping was also done in the VNIR (500-100nm) to map the occurrence of ferric oxide minerals. A wavelength image was constructed and showed interpolated wavelength positions of the three deepest absorption features and their associated depths. This minimum wavelength image (Figure 19), is viewed in RGB pseudocolor stretch representing the first, second and third deepest features respectively. The contrast in Figure 19, distinguishes three main zones of green, cyan-blue and yellow-orange colours.

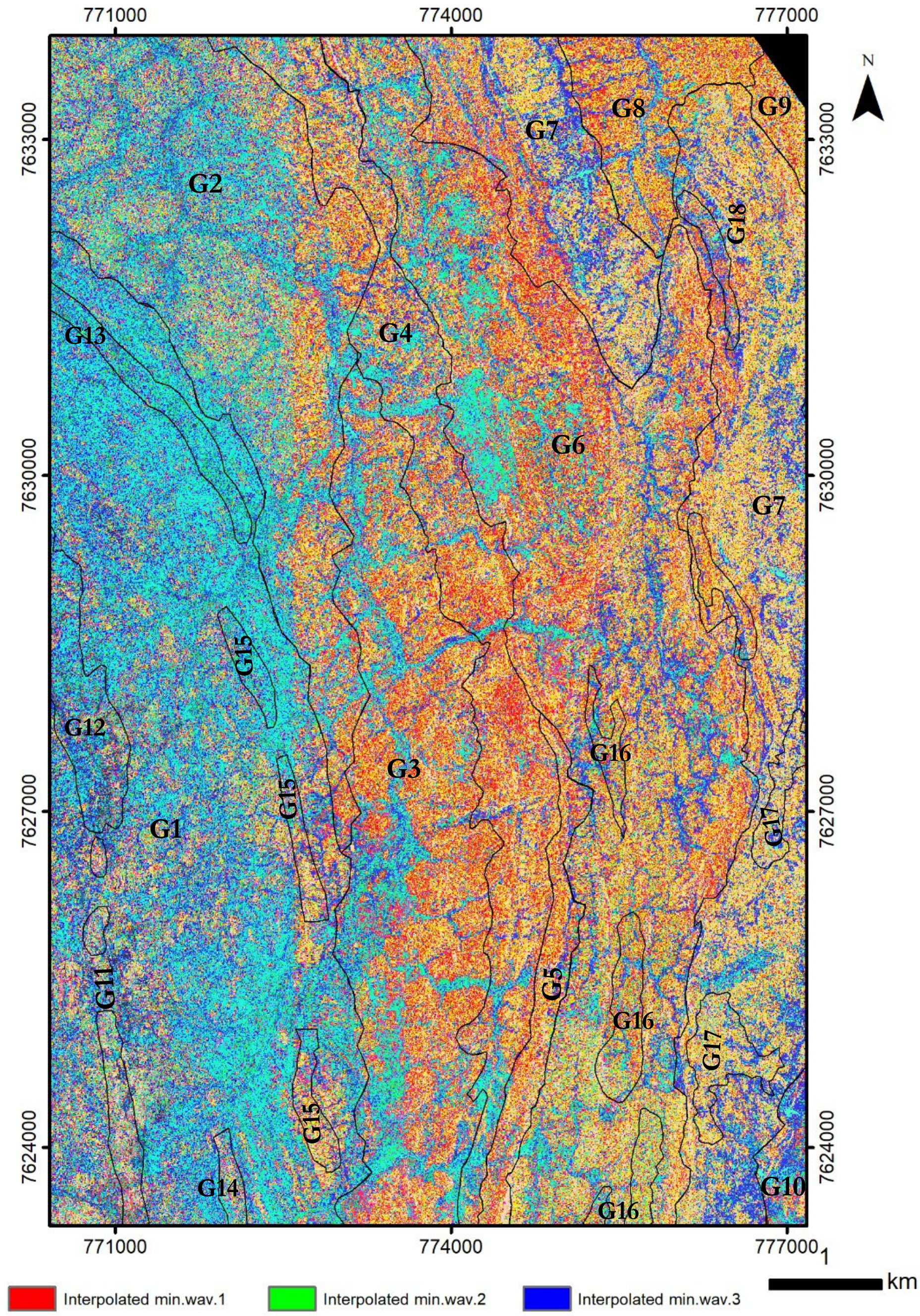

Figure 19: Pseudo-colour(RGB) composite of interpolated minimum wavelength (min.wav) between 500-1000nm showing mineralogical variation across the study area overlaid by black polygons of the lithological units' contacts

Spectra of the coloured pixels were picked from Figure 19to assess their corresponding wavelengths. The cyan-blue colour with a wavelength range of 560-600nm, is mostly restricted to G1 but is also found along stream beds across the study area. Interbedded with the cyan-blue is the green colour in the range of 740nm. The yellow-orange colours spread out from the centre of Figure 19 to the east, have a wavelength around 850nm. A wavelength of 940nm is also noted for minor red zones that are intercalated with the yellow-orange zones. From these wavelength positions, occurrence of ferric material is predicted with zones 940nm and 740nm being hematite-rich, whilst zones of 560-600nm and 850nm being goethite-rich zones.

5.3.4. Wavelength Mapping: VNIR Wavelength Map

Additionally, an HSV-fusion wavelength map for the VNIR was created. The resulting wavelength map Figure 20, gives an overview of spectral variability within the study area. Three major zones of different absorption features are defined by wavelength positions of around 856nm-940nm (magenta) and 560-680nm (blue-cyan) and 740nm (green). From observations of the wavelength maps, magenta hues dominate pervasively across the study area with intense zonation in the east (G7). The green hues are also mainly constricted to the east but highlight lineaments and stream beds. Cyan-blue hues are more dominant to the west (G1). Minor cyan horizons are reflected interbedded with green horizons along stream beds.

The absorption features around 560-680nm (cyan-blue) could be representative of goethite-rich horizons or vegetation. Diagnostic wavelengths (magenta and green) around 856-940nm and 740nm respectively could point out to hematite-rich horizons. Furthermore the zonation and spatial distribution of these features in G7, can suggest the occurrence of banded iron formations in this region.

VNIR minerals are easily identifiable from wavelength maps using dome-like and ridge structures and lineaments that stand out. Although the hyperspectral image is high-resolution, because of the increasing noise in the 500-1000nm range in this data as observed, quantification of these features was difficult using these maps.

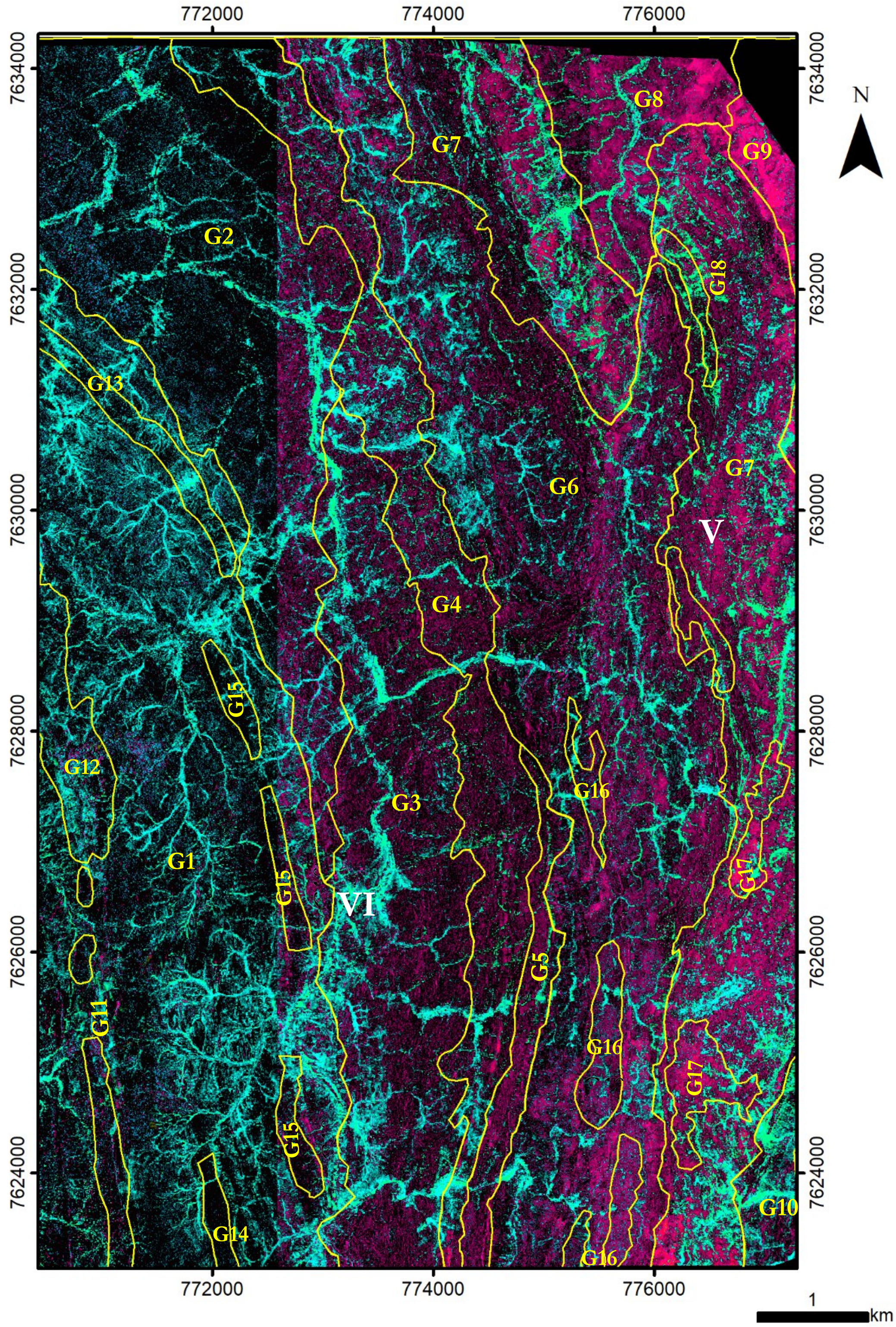

Figure 20: Wavelength map between 500-100nm showing the variation of the deepest absorption features and their relation to the division of the study area overlaid by yellow polygons of the lithological units' contacts

Ferric oxides have diagnostic absorption features between 430-970nm (Clark et al., 1990), and have been successfully mapped in various regions using both multispectral and hyperspectral data (Cudahy et al., 2008, Murphy and Monteiro, 2013; Hecker et al., 2019a; Kruse, 1988). The identification of three diagnostic absorption features within the VNIR shows the occurrence of these ferric oxides within the study area. Vital geological information can be extracted from aerial photographs based on the pattern ,texture colour, association and geometry of the features. The geologic terrain and climate can also influence how these features are recognised (Ray, 1960). For this study, the aerial photo provides a background for comparison and interpretation with the identified lineaments and structures in the wavelength maps. Ray (1960) additionally points out that the identification of features in aerial photos requires a large contrast in the erosional resistance of the neighbouring rocks. The ridges and dome-like structures, and linear horizons identified in this study clearly stand out from their surrounding topography. Drainage channels also provide a different topography due to erosion. The identification of these structures using the diagnostic absorption features of ferric oxides, infers the occurrence of ferric-rich minerals within the study area.

5.4. End-Member Collection

Subsequent analysis of the wavelength mapping involved end-member to facilitate sorting the absorption features into mineralogical groups. In this study, spectra were manually picked for the different classes in the wavelength map. Dominant absorption features were selected based on the wavelength map scatter plots which highlight the relationship between the interpolated wavelength position and the interpolated depth. Figures 7 and 9 show numerous dominating features between 2100-2400nm implying variation in mineralogy. A long narrow peak around 2164nm suggests a single deep feature mineral around this range. The peaks between 2198 to 2212nm with a big spread and minimal distinction between each peak, suggests a gradational series of minerals within the same mineral group. A shallow feature around 2250nm and the spread to around 2300nm might be due to an exchange of anions on the hydroxyl group or layer variation of the maps. These mineral spectra might be difficult to pick from the wavelength map due to their shallow depths. The peak around 2302nm, is distinct and represents a singular mineral group. Between 2330nm and 2350nm another mineral group occurs. Peaks observed above 2360nm are too shallow to be observed in the wavelength maps or they could signify artefacts within the data.

The height and spread of the histogram facilitate the comparison of classes of different wavelength ranges, and associated class abundances (Bakker et al., 2011). The spread of the classes presented within this study supported this notion and offered an insight into the class spectra that were picked and further analysed.

5.4.1. Spectra of Mineral Groups

Seven (7) main end-member groups were identified from the spectra collected from the SWIR hyperspectral wavelength map and two (2) from the VNIR wavelength map.

The pyrophyllite spectrum is clearly identifiable with the wavelength of the deepest feature at 2163nm and another at 2319nm. Five spectra were picked from regions I (G6 and west of G1) in Figure 18 and an average was calculated to represent the pyrophyllite spectrum. Figure 21 highlights the spectra from the image and comparison to the spectral library. As observed, the first and second deepest features are identified in both spectra and have a good match.

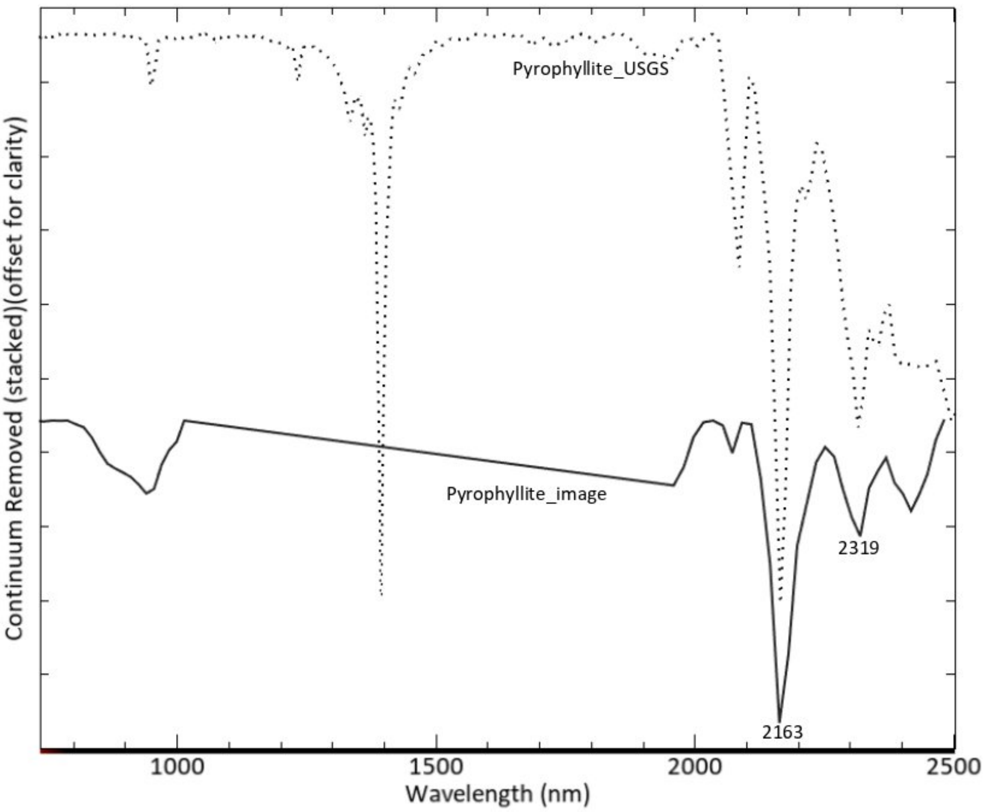

Figure 21: The figure shows the average image derived pyrophyllite spectrum (solid line), compared with the USGS pyrophyllite spectrum (dashed line)

The big spread between 2197 to 2250nm resulted in absorption features with diagnostic wavelengths at 2197nm, 2216nm and 2334nm being collected. Five spectra for each wavelength were collected in regions II and III (Figure 18) and averaged spectra were calculated respectively. Secondary to the first absorption features, two features at ~2340nm and ~2440nm were recognised for the spectra (Figure 22). Based on these positions, the end-members were interpreted to be a series of muscovite-illite minerals (white mica). Figure 22, shows the image derived spectra of the white mica and how they match both by shape and wavelength positions with the USGS white micas.

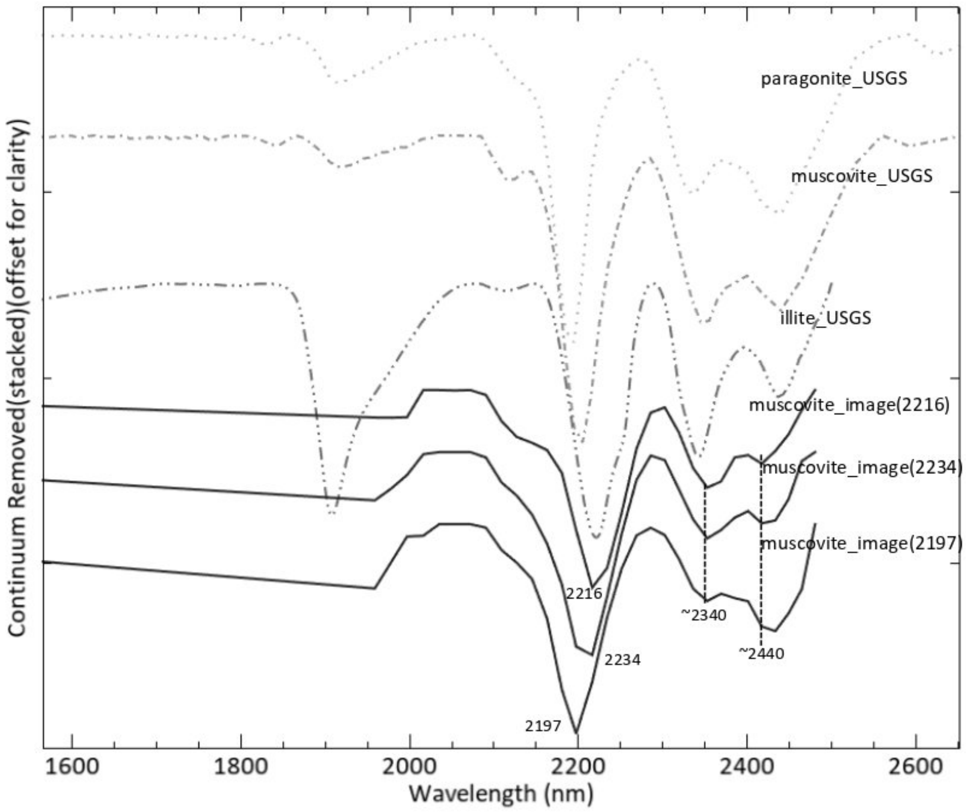

Figure 22: The figure shows the average image derived white mica spectra (solid lines), compared with the USGS white mica (dashed lines)

The spectra for ferro-magnesian minerals were picked from regions IV (Figure 18). As in the case of the other end-members, average spectra were calculated. Figure 23 illustrates the ferro-magnesian mineral spectra collected. Absorption features at 2251nm and 2336nm were predicted to be Fe-chlorite, whilst the spectra with a wavelength position of 2352nm were to be Mg-chlorite. The Mg(OH) spectra interpreted to be amphibolitic and biotite, were not very clear but had diagnostic features at 2251nm and 2352nm. Spectra with features between 2302-2319nm were also collected and interpreted as saponite or nontronite. These spectra were differentiated from similar spectra with a second diagnostic at ~2145nm, and predicted to be dolomite. Epidote spectra with a feature at 2336nm were also collected. Whilst spectra of epidote, dolomite and saponite/nontronite were matched to the USGS library (Figure 23a), the Fe,Mg chlorite and Mg(OH) (Figure23b) were easier to match using the GMEX library.

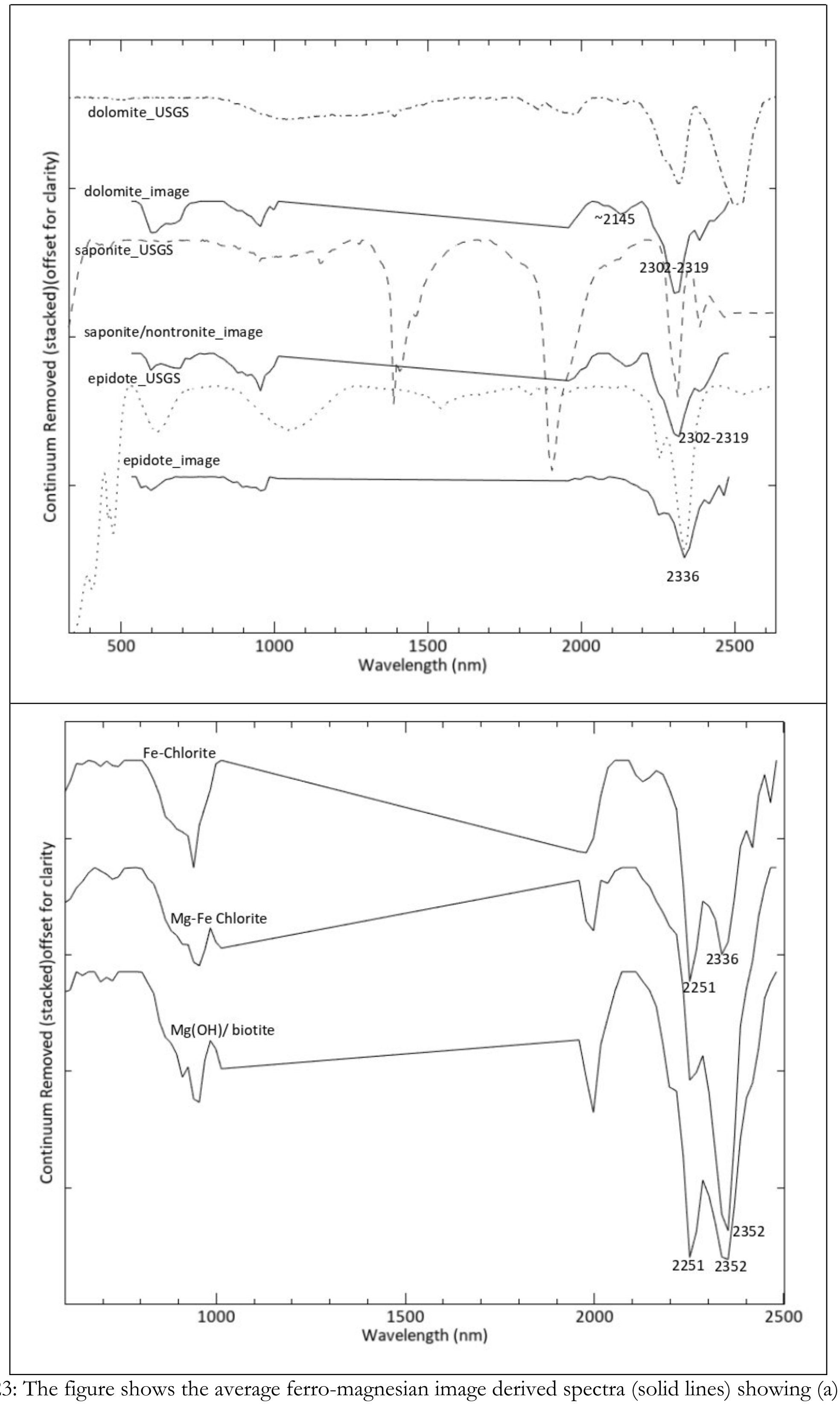

Figure 23: The figure shows the average ferro-magnesian image derived spectra (solid lines) showing (a) spectra compared with USGS library (dashed lines), (b)spectra compared with GMEX library

Because of the manual collection of the spectra, some image pixels could not be identified due to their shallow depths despite being present in the scatterplot. It is difficult to distinguish between Mg,Fe-(OH) and carbonate spectra as well as some mixed image pixels. This put a limitation on the number of end-members collected and their certainty. However, the scatterplot circumvents this limitation of the end members and would once again be considered in the classification for these complicated separations.

The spectral resolution of the VNIR was limited and limited the extraction of pure end-members for the VNIR. However average spectra for the pink and green-cyan were extracted from regions V and VI in Figure 20. The graph in Figure 24 highlights the spectra interpreted to be goethite and hematite. The interpreted hematite spectra showed a deep feature in the range between 865-960nm, and was confirmed using the GMEX library. The goethite spectra were also compared with the GMEX library. These spectra were accepted due to the shape as well as using average spectra is not always as accurate.

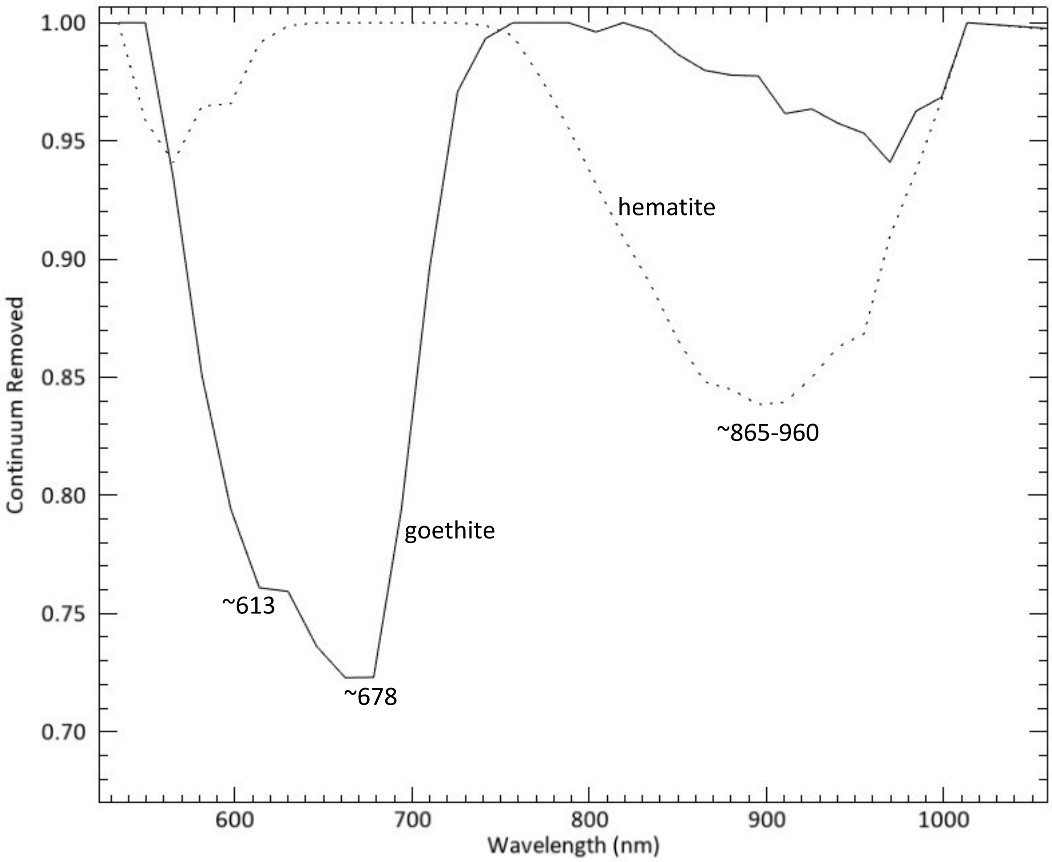

Figure 24: The figure shows average image derived spectra for goethite (solid line) and hematite (dashed line)

5.5. Decision Tree Mineral Classification

The decision tree classifier was used to classify the SWIR minerals from the hyperspectral data. With the implementation of thresholds based on the wavelength positions of the deepest absorption features, the decision tree (Figure 25) is viewed from two aspects; thresholds less than 2250nm and thresholds above 2250nm.

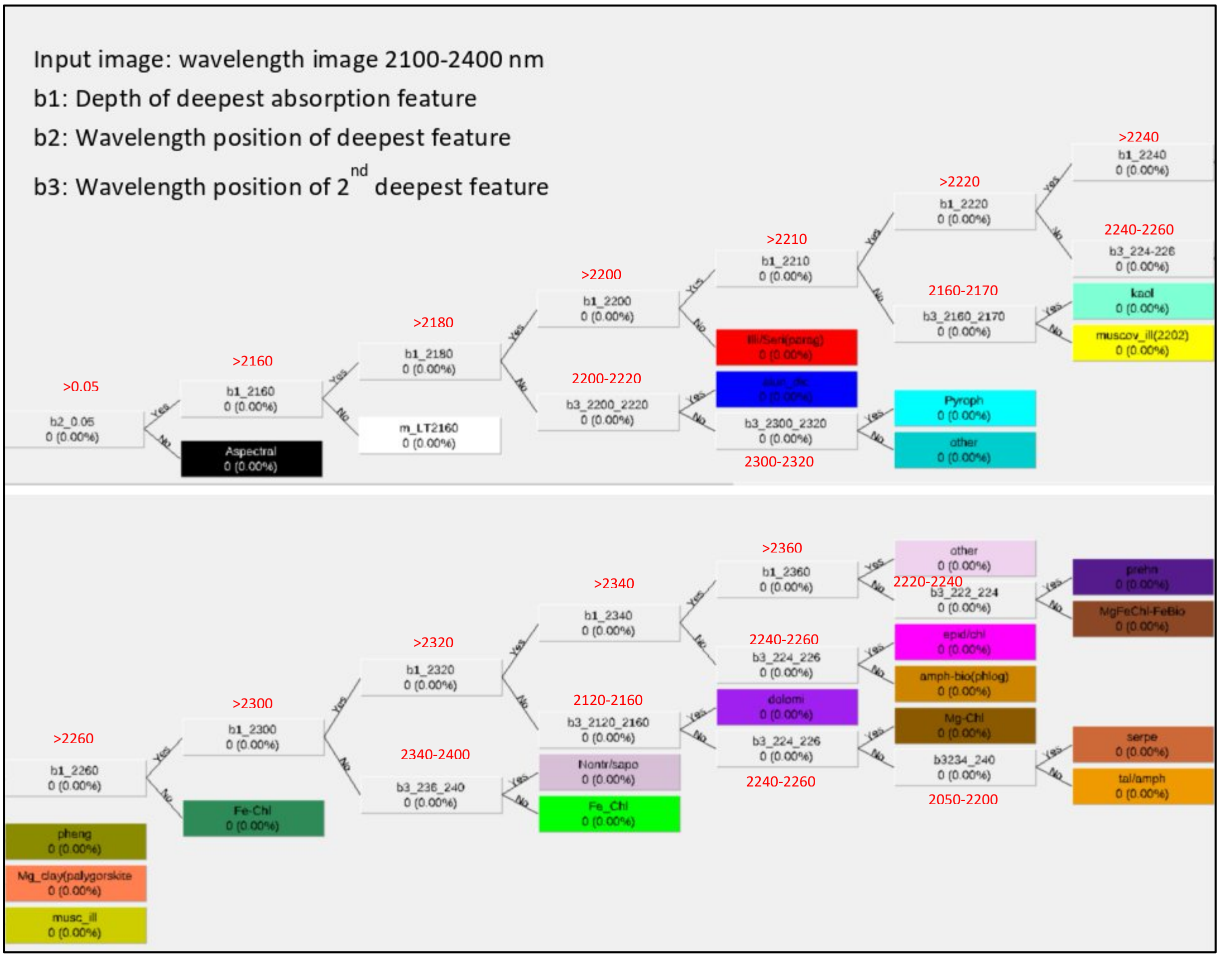

Figure 25: Decision tree classifier for SWIR minerals between 2100-2400nm, with the threshold expressions highlighted in red

The wavelength range covered was between 2100-2400nm, with input thresholds starting from 2160nm to 2360nm for the first deepest feature. Each node classified the hyperspectral image pixels into a mineral class from the diagnostic wavelength position of this first feature. For different nodes, the wavelength position of the second deepest feature was used to classify a mineral group more succinct. Candidate minerals were decided based on the decision tree and analysis of the USGS spectral library. Figure 26 shows a simplified interpretation of this decision tree, highlighting the input wavelength positions and associated expressions and classified candidate minerals.

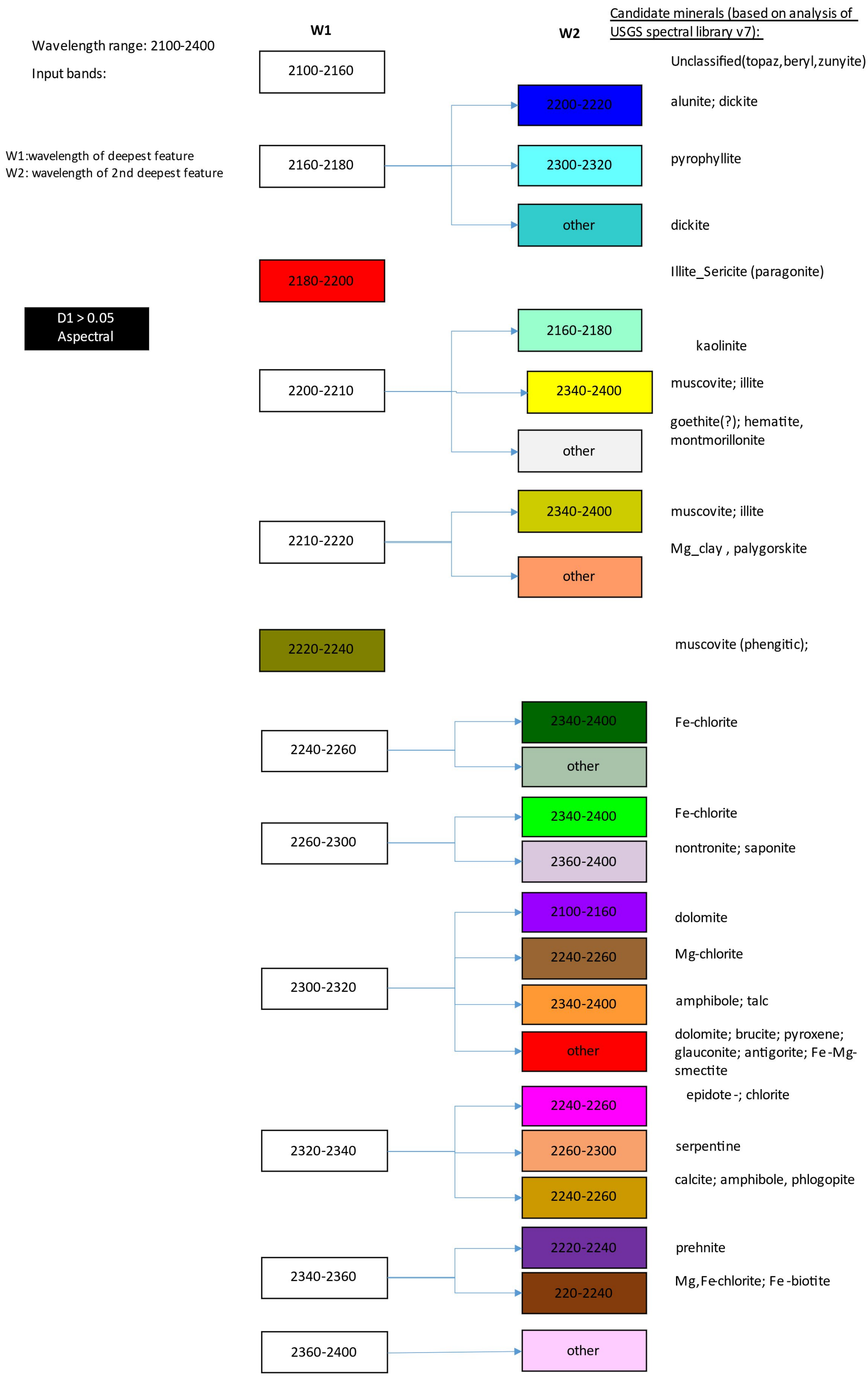

Figure 26: Simplified illustration of the wavelength thresholds of the decision tree classification

5.6. Classified Mineral Map

From iterative analysis and end-member refinement, a classified mineral map (Figure 27) was produced of the study area. Whilst the naming of the minerals was interpretated based on the mineral groups from the classification, some mineral groups could not be clearly separated from each other. For the purposes of this study the naming of minerals thus was a research personal interpretation from wavelength positions and classification shown in Figures 26 and 27. The mineral map is analysed and explained using the two main categories highlighted by the decision tree; wavelength below 2250nm and wavelength above 2250nm. Wavelength positions below 2250nm for the deepest absorption feature reflect the Al-clay minerals, whilst those above 2250nm signify ferro-magnesian minerals. Figure 26, highlights the classified clay and magnesian minerals within the study area based on the hyperspectral image pixels.

Minerals classified as aspectral appear in black across the majority of the units in the study area. This was based on their shallow depths as they could not be easily distinguished below an interpolated depth 0.05.

Majority of minerals in the east of the map were classified as aspectral. The classified map also shows interpreted clay minerals of pyrophyllite and a series of muscovite-illite minerals. Pyrophyllite in cyan, occurs primarily in G6 with alunite and dickite. These three minerals occur in association together, and similarly present in the north and southeast of G7. A minor zone of pyrophyllite is also observed southwest G1 close to the G11 contact. Kaolinite is sparsely distributed and appears in low abundances (<1%) across the study area. The muscovite-illite mineral variations are prominent across the study area, highlighted by the variations in yellow to red. This variation is interpreted to be based on the changes from short wavelength to long wavelengths of the white micas. Muscovite in yellow dominates the study area occurring in abundance in G11,G2,G3 and G4. Interpretations show the phengitic and muscovite-illite also synchronously dominate these central units in abundance. The yellow muscovite is also shown intercalated horizontally in the west of G1 and a NW-SE cross cutting feature is also delineated. Red represents a short wavelength illite-sericite interpreted as paragonite dominant in G6, G8 and G9.Just as the longer wavelength muscovite, this mica also occurs west of G1 and G7. These white micas show a cyclic pattern going from Al-poor to Al-rich across the centre (G2,G3,G4) upwards to the east (G6,G7,G8) of the study area.

Majority of the ferro-magnesian minerals are restricted to the west of Figure 27 bounded within units G1,G12, G13,G14 and G14. Epidote (magenta), Fe-chlorites (green) and amphiboles (brown) show an elaborate bedding style. Epidote and chlorite are the most abundant, with association of Mg-rich biotite, talc and serpentinite minerals. The Fe-chlorite minerals are also spatially distributed along stream beds, whilst Mg-rich clay interpreted as palygorskite is sparsely distributed within G1. A similar bedding pattern of Mg-Fe rich minerals is observed in unit G6 towards the east of the map. Purple indicates dolomite restricted to the top of the mafic units in G15as well as close to G1-G3 contact, south of the study area. Furthermore muscovite rich zones (yellow and red) can be identified interbedded within these mafic zones implying they could either be felsic intrusions or an indicator of different deformation phases. This pattern of mafic and felsic minerals also appears in the east of the map towards the south, however marked predominantly by epidote and chlorite within the felsic zone.

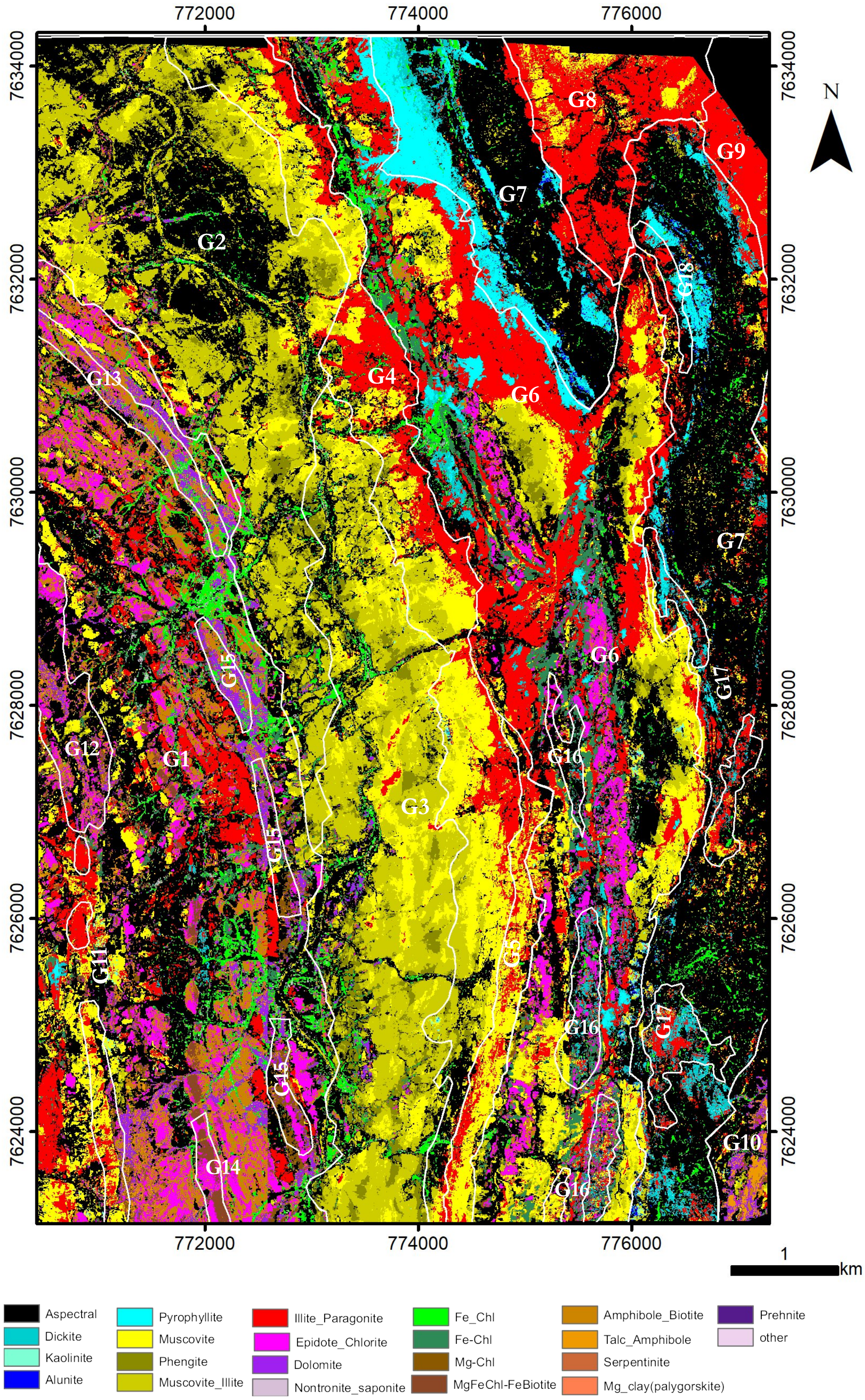

Figure 27: Classified Mineral Map of the Northern Coongan Greenstone Belt

The spatial distribution of the clay minerals would suggest a more felsic central zone in the study area going up to the east. Presence of alteration minerals such as kaolinite and alunite indicate intense alteration away from the centre towards the east of the map. Additionally, the cyclic occurrence of both aluminium-rich and aluminium poor micas is indicator of a change in chemical environment, temperature and thus alteration. The presence of illite is significant of lower temperature alteration, mainly restricted in the centre part of the map, contradicting the alteration pattern at the top. Pyrophyllite and dickite occurrences also indicate a more turbulent deposition environment compared to the one in which white micas form.

Furthermore, the spatial distribution of the Mg-Fe rich minerals suggests mafic sequences to the west of the study area. The bedding style governing these minerals indicates that the rock units were deposited conforming to the stratigraphy in a quiet environment. The chloritic and amphibolitic material is not distinguishable from this classification as to whether they are primary or secondary minerals due to alteration. The cyclic presence and occurrence of these mafic minerals interbedded within the felsic zones can be an indicator of a change in depositional environment and marks different deformational episodes.

This qualitative surface mineral map highlighting potential white micas (muscovite, paragonite , phengite), clay minerals (kaolinite, illite), silicates (amphibole, biotite epidote, chlorite, talc), carbonate minerals (dolomite), sulfate minerals (alunite) and iron oxides (hematite , goethite) suggests hydrothermal alteration. Additionally, the hydrated minerals can be used to predict forming conditions and thus the type of facies like argillic or propylitic. In hydrothermal environments, primary minerals tend to be altered to hydrothermal minerals (Pirajno, 2009b). The formation of these hydrothermal alteration minerals is indicative of temperature and pressure conditions, fluid composition as well as discharge pathways . Hence establishing the location and extent of the hydrothermal alteration, assists in interpreting chemical environments and deposition sequences.

5.7. Linking results and Conceptual Stratigraphic Model of the CGB

The different processed data sets provided a pathway to study the northern CGB in great detail. From analysis, interpretations and relationships were established from a larger framework using geophysical , geological and field data to a more localised framework in relation to the hyperspectral information. Gamma ray intended to show zonation in the CGB. Major divisions based on radioelement signatures were compared with existing stratigraphy. The geophysical data provided structural and magnetic detail of possible fluid pathways and lithological signatures. Integrating all these data with the mineral maps was to show how minerals are related to the general division of the CGB. This facilitated for interpretations of possible paleosurfaces, hydrothermal alteration and its spatial extent within the greenstone belt.

Paleosurface identification

Lithological boundaries were already defined and interpreted from the radiometric ternary image (Figure 12). Comparison of the hyperspectral mineral map (Figure 27) with theses boundaries, illustrates clear surfaces and separation of varying mineralogy . The clear and sharp contacts identified in Figure 13 indicate a sharp change in chemical variation and thus mineralogy. The hyperspectral map in Figure 27, validates these differences and shows a distinct mineral variation around these boundaries. These contacts are interpreted to be zones at which deposition, hydrothermal activity and change in environment has taken place and hence are paleosurfaces.

Hydrothermal alteration

The overlay of the hyperspectral classification map with the lithological boundaries (Figures 27) show evidence of hydrothermal minerals. Different mineral assemblages ranging from chlorite-carbonate as well as enrichment of clay minerals up the stratigraphy are identified across the different units. Occurrence of these mineral assemblages is interpreted to be varying degrees of alteration across the sequences of the study area. Gossanous and iron oxide rich zones were also identified in Figure 20 whose occurrence is also interpreted as exhalative horizons or weathered veins that acted as fluid pathways. The lineaments and structures displayed in Figure 16 give some insight on the impact of structure on alteration mineral distribution in the study area. The integral analysis of Figure 27 and Figure 16 implies that both structure and lithology control the mineral alteration in the study area. The structures are interpreted to be fluid conduits.

The interpreted alteration minerals and their relation to the different lithological units are summarised in Table 5. The potential paleosurfaces, geochemical characteristics, geological and associated field data are also described.

Summary Table

Table 5: Summary of interpreted Units and their associated mineralogical and geological characterisation

Unit/ Contact	Hyperspectral minerals	Spatial distribution of alteration	Geophysical + aerial photo	Field observations	Geological map
G1 **Contacts:** **G1_G2(transitional north)** **G1_G2(sharp south)** **G1_G3** **Potential paleosurface**	Epidote-chlorite 10%, amphibole 14%, talc 2%, Mg-chlorite 2%, Fe-chlorite 8%, nontronite-saponite 1% dolomite 5%, serpentinite 1%, MgFeChl 3%, muscovite 7% paragonite 10% pyrophyllite 0.04% Aspectral 36%	Top Along fractures, Along bedding, zonated in the far west of unit	Mafic (low radioelement content) Moderate to intense fracturing/faulting (NE-SW trend) Highly magnetic structures Felsic structure cross-cutting (NW-SE) fabric	Basalt + volcaniclastic, quartz-chlorite-carbonate schist Chloritized, silicified & carbonated samples	North star basalt: Metabasalt and metadolerite; local pillow structures Mt Ada basalt : Komatiitic basalt + dolerite; metamorphosed Komatiite, with pyroxene spinifex texture; local talc--carbonate rock; metamorphosed, Red, white, and black layered, jaspilitic chert; Duffer formation: Sand, silt, and gravel in active drainage channels; includes clay, silt, and sand in poorly defined drainage courses on floodplains
G2 **Contacts:** **G2_G3 (transitional)** **G2_G4** **Potential paleosurface**	Muscovite 9% muscovite-illite 35%, phengite 8% paragonite 1% (Fe-chlorite 3%, epidote 1%, amphibole 1% ,dolomite 1%) Aspectral 40%	Pervasive Along drainage channels	Mafic & felsic, with elevated k%, variable magnetism, high in the north and low in the south,	Volcanoclastic , tonalite, basalt, conglomerate, gritstone, agglomerate, dacite, sandstone(g2-g4), dolerite-gabbro, (near g1_g2)	Duffer formation: Dacitic volcanic breccia, sandstone, and tuff; metamorphosed + sand, silt, and gravel in active drainage channels; includes clay, silt, and sand in poorly defined drainage courses on floodplains +fine-grained felsic volcanic sandstone; local chert, wacke and conglomerate; thinly bedded; locally silicified; Residual calcrete; massive, nodular, and cavernous limestone; variably silicified
G3 **Contact:** **G3_G4 (sharp)** **Potential paleosurface**	Muscovite 15%, muscovite-illite 47%, phengite 12% paragonite 1% (Fe-chlorite 4%, nontronite 1%, dolomite 1%) Aspectral 18%	Pervasive	Felsic, with elevated k%, very low magnetic expression	Volcaniclastic, conglomerate, sandstone, greywacke + tonalite, sandstone	
G4 **Contact :** **G4_G5 (transitional)** **G4_G6 (sharp)** **Potential paleosurface**	Muscovite 36%, muscovite-illite 19%, paragonite 24% phengite 2% Fe-chlorite 1%, Aspectral 17% Distinct layering between G4_G6 contact	Pervasive,	Felsic, with elevated K%, no magnetic expression	Volcaniclastic conglomerate chert, andesite, gritstone greywacke, sulphide fe gossan, chert, exhalative, sandstone, stromalitic chert	Panorama(Salgash): Rhyolitic tuffaceous volcaniclastic sandstone, including ash beds; well bedded; metamorphosed quartz-porphyritic rhyolite; locally schistose; metamorphosed
G5 **G5_G6 (transitional)**	Muscovite 51%, paragonite 32%, phengite 1%, muscovite-illite 2% Aspectral 14%	Bottom	Mafic, high eU content, with low eth, moderately magnetic	Sandstone, chert, basalt	Panorama(Salgash):??Basalt? Quartz-porphyritic rhyolite; locally schistose; metamorphosed + White, grey, and blue-black layered chert after dolomite; locally stromatolitic; metamorphosed

G6 **Contact:** **G6_G7 (sharp)** **Potential paleosurface**	Paragonite 25%, pyrophyllite 3% dickite 3%, muscovite 14%, phengite 2%, muscovite_illite 7% Distinct layering of Fe-chlorite 10%, epidote-chlorite 5%, amphibole 2%, MgFeCh 1%, Aspectral 27%	Top	Mafic & felsic, with very high K-content, magnetic imprints on minor lineaments in the centre of unit NE-SW fault-line displacing unit G6 and G7	Basalt, exhalative, andesite exhalative, chert, basalt, sandstone, tuff, sandstone-conglomerate, andesite (close to g13top)	Eurobasalt(Kelly): Komatiite, with pyroxene spinifex texture; local talc--carbonate rock; metamorphosed, massive and pillowed lavas and subvolcanic intrusions massive basalt;
G7 **Contacts:** **G7_G8 (sharp)** **G7_G10 (sharp)** **Potential paleosurface**	Pyrophyllite 8%, alunite 1%, dickite 7%, paragonite 9%, muscovite 3%, muscovite_illite 1% Fe-chlorite 3% Aspectral 67%	Bottom, along fractures, top	Mafic & felsic, low radioelements, high eTh with moderate eU enrichment, strong magnetic imprints with faulting and fracturing	BIF jaspilite, sandstone-siltstone-BIF, gabbro, Fe-rich shale, greywacke, silica breccia (southside)	Wyman(kelly),cleaverville(gorge creek/ fortescue),cenzoic sediments: Porphyritic rhyolite and rhyodacite; local felsic volcaniclastic rocks; metamorphosed Felsic volcanic sandstone; tuffaceous; local quartz sandstone; metamorphosed + BIF and ferruginous chert; local banded quartz--magnetite--grunerite rock; metamorphosed +Ferruginous duricrust; includes massive, pisolitic, and nodular ferricrete
G8 **Contacts:** **G8_G9/G7 (sharp)** **Potential paleosurface**	Paragonite 58%, muscovite 12% Aspectral 30%	Pervasive	Felsic, high radioelement enrichment of all 3, with elevated Th-content, no magnetic imprints	Turbidite, sandstone-siltstone, siltstone, conglomerate (out of study area but same unit)	Lallah Rook Sandstone (De Grey): Sandstone with beds of conglomerate, and minor siltstone and shale; metamorphosed
G9 **Contacts** **G9_G7 (transitional)**	Paragonite 45%, Muscovite 1%, Dickite 1%, Aspectral 52%	Pervasive	Mafic& felsic Th-rich with a moderate eu enrichment, low magnetic imprint	Mt Roe basalt	Mt Roe Basalt(Bruce): Massive, porphyritic, vesicular, and amygdaloidal basalt; some pillow basalt
G10 **Contacts:** **G7_G10 (sharp)** **Potential paleosurface**	Dolomite 13%, talc-amphibole 14%, Fe-chlorite 2%, MgChl 3%, epidote-chlorite 1%, serpentinite, amphibole-biotite 1%, muscovite 3%,muscovite-illite 2%, phengite 1%, dickite 1%, paragonite 2%, Aspectral 55%	Bottom	Mafic, low radioelement, with elevated eu and moderated eth, low magnetic imprint	Carbonate, greywacke, chert/basalt	Dalton Suite: Metaperidotite and serpentine--chlorite schist + serpentinite, schistose
G11 **Contact:** **G11_G1** **Potential**	Paragonite 18%, muscovite 38%, muscovite-illite 2%, FeChl1%, MgChl 5%,	Pervasive	Felsic, high radioelement content of all 3, with elevated eu, no	U/M basalt contact, Qtz-Chl-Carb Schist (in g1 south)	Emu Pool Supersuite: Strongly foliated to schistose metamonzogranite; fine to medium grained

paleosurface	amphibole 3%, dolomite 3%, talc-amphibole 3%, MgFeCh 1%, epidote 3% Aspectral 22%		magnetic imprint		
G11 top	Aspectral 10%, Paragonite 74%, muscovite 2%, FeChl 2%, amphibole-biotite 1%, MgFeChl 8%, epidote 2%	Pervasive	Felsic, high radioelement content of all 3, with elevated eu, no magnetic imprint	U/M basalt contact, Qtz-Chl-Carb Schist (in g1 south)	Emu Pool Supersuite: Strongly foliated to schistose metamonzogranite; fine to medium grained
G11 mid	Aspectral 8%, paragonite 82%, muscovite 8%, MgFeChl 1%	Pervasive	Felsic, high radioelement content of all 3, with elevated eu, no magnetic imprint	U/M basalt contact, Qtz-Chl-Carb Schist (in g1 south)	Emu Pool Supersuite: Strongly foliated to schistose metamonzogranite; fine to medium grained
G12 (Compositional variable units)	Dolomite 7%, Epidote-chlorite 15%, Fe-chlorite 1%, Mg-chlorite 4%, Amphibole-biotite 11%, Talc-amphibole 4%, MgFeChl 5% Muscovite 3%, Muscovite-illite 2% Phengite 1%, Paragonite 2%, Aspectral 45%	Pervasive	Mafic, low radioelement, with Th enrichment, magnetic with fracturing Fracture zone (NE-SW trend)	Quartz-carbonate gossan in fault, Dolomitised Ultramafic-basalt contact, basalt, Chlorite-carbonate schist	Mcphee formation: Talga talga Talc--carbonate and chlorite--serpentine--carbonate schist; metamorphosed ultramafic volcanic rocks(westg12,embeddedqithi n g1)
G13(right top)	Aspectral 11%, muscovite 2%, FeChl 11%, MgChl 2%, nontro-sapo 1, amphibole-biotite 30%, dolomite 25%, talc-amphibole 9%, MgFeChl 1%, epidote-chlorite 8%	Pervasive	Mafic, low radioelement, with Th enrichment, magnetic with fracturing Fracture zone (NE-SW trend)	Gabbro, dolerite, chlorite-schist	Komatiite, with pyroxene spinifex texture; local talc--carbonate rock; metamorphosed
G14(bottom left)	Aspectral 3%, FeChl 1%, amphibole-biotite 9%, dolomite 1%, MgFeChl 44%, epidote 40%	Pervasive	Mafic, low radioelement, with Th enrichment, magnetic	Quartz vein	Red, white, and black layered, jaspilitic chert; metamorphosed
G15(bottom right) (top)	Aspectral 5%, paragonite 1%, serperntinite 3%, FeChl 14%, MgChl 4%, amphibole-biotite 22%, Dolomite 40%, talc-amphibole 8%, epidote 2%	Pervasive	Mafic, low radioelement, with Th enrichment, magnetic with fracturing Fracture zone (NE-SW trend)	Basalt, breccia, dolerite	Komatiite, with pyroxene spinifex texture; local talc--carbonate rock; metamorphosed
G15(mid)	Aspectral 28%, paragonite3%,	Pervasive	Mafic, low radioelement,	Basalt, breccia,	Komatiite, with pyroxene spinifex texture; local talc--

	serpentinite 3%, muscovite4%, phengite 1%, muscovite-illite 1%, FeChl 9%, MgChl 19%, amphibole-biotite 2%, dolomite 18%, talc-amphibole 5%, epidote 7%		with Th enrichment, magnetic with fracturing Fracture zone (NE-SW trend)	dolerite	carbonate rock; metamorphosed
G15(bottom)	Aspectral 26%, paragonite 2%, Fechl 4%, MgChl 30%, amphibolite-biotite 1%, dolomite 13%, talc-amphibolite 5%, epidote 18%	Pervasive	Mafic, low radioelement, with Th enrichment, magnetic with fracturing Fracture zone (NE-SW trend)	Basalt, breccia, dolerite	Komatiite, with pyroxene spinifex texture; local talc--carbonate rock; metamorphosed
G16 **G16(left)**	Aspectral 33%, Fe-chlorite 4%, Epidote-chlorite 2%, amphibole-biotite2%, Muscovite 43%, Paragonite 11%, Phengite 2%, muscovite-illite 2%, (Dickite, alunite)	Pervasive	Low radioelement enrichment, with slightly elevated Th-content, no magnetic imprint	Sandstone, andesite, basalt	Euro Basalt (Kelly): Komatiitic basalt; massive and pillowed lavas and subvolcanic intrusions; local pyroxene spinifex texture; metamorphosed
G16(right)	Aspectral 16%, dickite 10%, paragonite 16%, alunite 2%, palygorskite 1%, kaolinite 1%, muscovite11%, FeChl 19%, amphibolite-biotite 2%, MgFeChl 10%, epidote 13%	Pervasive	Low radioelement enrichment, with slightly elevated Th-content, no magnetic imprint	Sandstone, andesite, basalt	Euro Basalt (Kelly): Komatiitic basalt; massive and pillowed lavas and subvolcanic intrusions; local pyroxene spinifex texture; metamorphosed
G16(mid)	Aspectral 36%, Dickite 14%,paragonite 7%, muscovite 8%, muscovite-illite 2%, FeChl 15%, amphibole-biotite 2%, MgFeChl 2%,epidote 12%	Pervasive	Low radioelement enrichment, with slightly elevated Th-content, no magnetic imprint	Sandstone, andesite, basalt	Euro Basalt (Kelly): Komatiitic basalt; massive and pillowed lavas and subvolcanic intrusions; local pyroxene spinifex texture; metamorphosed
G16(top)	Aspectral 59%, dickite 4%, paragonite 9%, muscovite 4%, FeChl 13%, MgChl 1%, MgFeChl 1%, epidote 7%	Pervasive	Low radioelement enrichment, with slightly elevated Th-content, no magnetic imprint	Sandstone, andesite, basalt	Euro Basalt (Kelly): Komatiitic basalt; massive and pillowed lavas and subvolcanic intrusions; local pyroxene spinifex texture; metamorphosed
G17 **G17(top)**	Aspectral 48%, Pyrophyllite 7%,	Pervasive	High radioelement	No sample	Wyman(Kelly):

	Dickite 20%, Paragonite 19%, muscovite 4%, muscovite-illite 1%,		enrichment, with high Th and U content, no magnetic imprint		Felsic volcanic sandstone; tuffaceous; local quartz sandstone; metamorphosed Cenozoic Sediments: Ferruginous duricrust; includes massive, pisolitic, and nodular ferricrete;
G17(mid)	Aspectral 50%, dickite 7%, paragonite 31%, pyrophyllite 1%, muscovite 8%, muscovite-illite 1%, FeChl 2%	Pervasive	High radioelement enrichment, with high Th and U content, no magnetic imprint	No sample	Wyman(Kelly): Felsic volcanic sandstone; tuffaceous; local quartz sandstone; metamorphosed Cenozoic Sediments: Ferruginous duricrust; includes massive, pisolitic, and nodular ferricrete;
G17(bottom)	Aspectral 50%, Dickite 18%, paragonite 23%, pyrophyllite 1%, muscovite 3%, muscovite-illite 1%, FeChl 3%,	Pervasive	High radioelement enrichment, with high Th and U content, no magnetic imprint	No sample	Wyman(Kelly): Felsic volcanic sandstone; tuffaceous; local quartz sandstone; metamorphosed Cenozoic Sediments: Ferruginous duricrust; includes massive, pisolitic, and nodular ferricrete;
G18	Aspectral 52%, Paragonite 22%, Pyrophyllite 13%, Dickite 11%, muscovite 1%, FeChl 1%	Pervasive	Low radioelement enrichment, with slightly elevated Th-content, no magnetic imprint	No sample	Wyman(Kelly): Felsic volcanic sandstone; tuffaceous; local quartz sandstone; metamorphosed

6. DISCUSSION

The following chapter discusses the interpreted stratigraphic column, limitations of the research and recommendations for further studies

6.1. Relative sequencing of Events (Reconstruction)

Combining all the information extracted from the various data sets (Table 5), the characteristics of altered and unaltered units have been interpreted based on the relationship of hydrothermal alteration minerals from the mineral maps to the rock units. The spatial distribution of these hydrothermal alteration minerals and rock unit characteristics are summarised and organised into a relative chronology of events for the nCGB.

The zonation of the interpreted hydrothermal minerals alludes to different episodes of deposition of genetically related strata. The units are bounded by unconformities which are considered to be sequence boundaries between the different episodes. These sequence boundaries symbolise an inferred change in the environment of deposition. In the nCGB, the overall sequence of events alludes to volcano-sedimentary deposition sequences going up the stratigraphy, approximately dipping east (Figures 2) from a mafic to a more felsic environment (Figures 12 and 26). This is in accordance with Zegers (1996), Van Krandendonk (2002) and many others (1989; 2011; 2006), confirms this general younging direction eastward across the northern CGB. Comparison of the new interpretation to the published stratigraphy (Hickman, 2011), shows similarities in the mafic sequences and transitioning into the volcanoclastic-sedimentary units. However, some differences are noted in the basal sequences, mineral variation and distribution of pyrophyllite and white mica highlighted in the mineral map and contradict the chemical environs described by Van Kranendonk and Pirajno (2004). This new information and the stratigraphical relations of the northern CGB suggest that some currently accepted models may need revision.

Within this research the depositional cycles were highlighted as the lithological units G1 to G18. The boundaries between these units are described in terms of the nature of the lithological contacts; transitional or sharp. The sharp contact surfaces are interpreted as probable paleosurfaces and mark an inferred change in depositional environment. This is consistent with Widdowson (1997) and Sillitoe (2015) characterising distinct surface and near-surface products as typical indicators of fluid discharge zones in different depositional conditions. Relevant work by Jutras (2004), analysed preserved paleosurfaces in sedimentary basins to construct a geometric stratigraphy of Gaspé Peninsula. Furthermore, mineral map interpretation show that units G1-G4, G6-G7 and G11 are likely hydrothermally altered with the distribution ranging from a pervasive, top, bottom or along fractures and drainage channels. Seven potential surfaces were identified G11-G1, G1-G2, G3-G4, G4-G6, G6-G7, G7-G8 and G8-G9.

The relative sequence of events as interpreted in this study are shown in Figure 28.

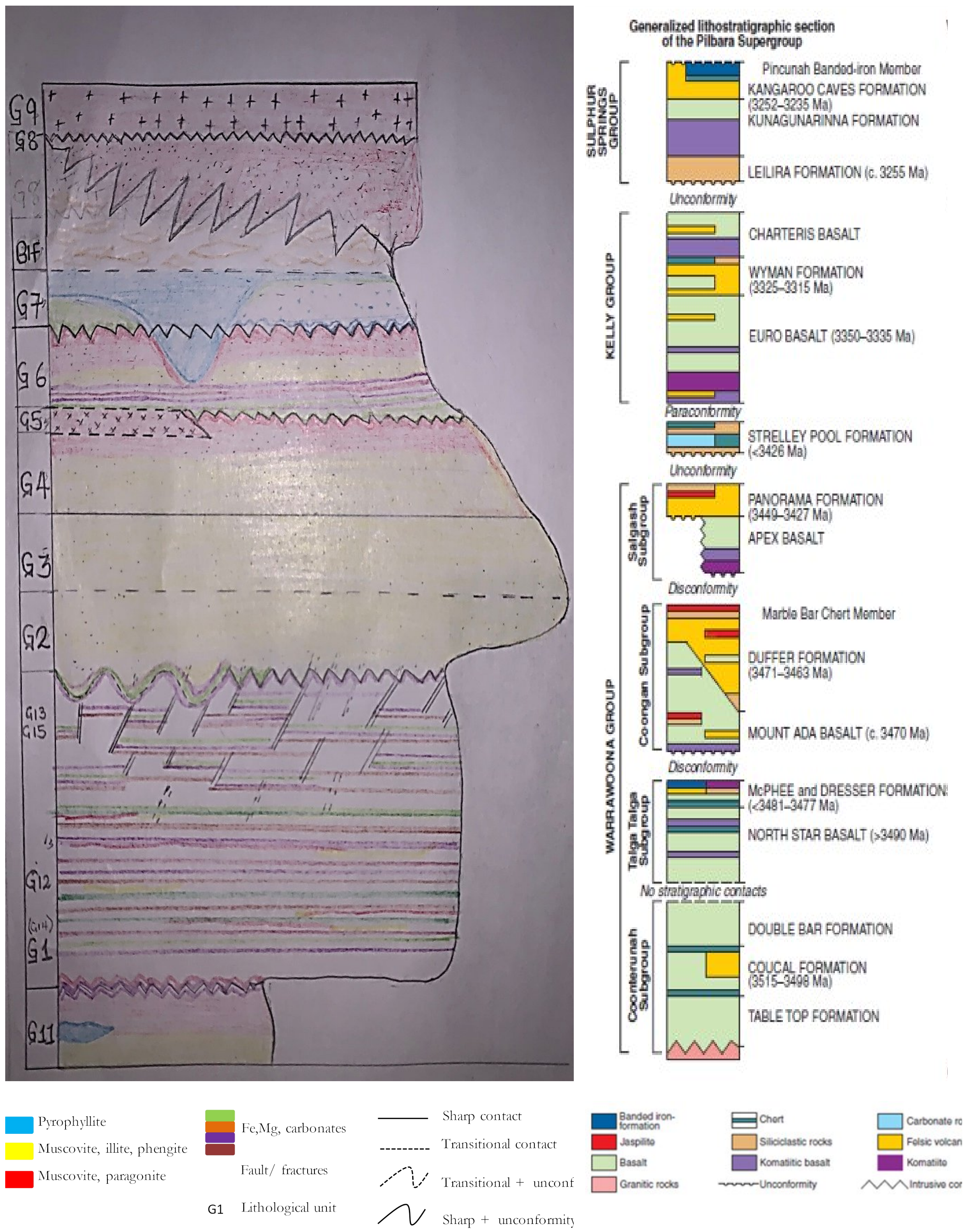

Figure 28:Stratigraphic Column showing (a)The interpreted relative sequencing of events in the nCGB, (b) The stratigraphy of the geological map after Hickman (2011)

The different units are bounded by contacts shown as either bold lines for sharp contacts or dashed lines for transitional contacts. The unconformities follow a similar pattern, with the solid jagged lines showing an unconformity and dashed jagged life showing a transitional unconformity. The solid jagged lines identify potential paleosurfaces. The colour code represents the type of hydrothermal alteration concordant with the classified mineral map in Figure 27. The different hatching styles separate the different units from each other. The BIF are bedded but represented in this column as bedded curved figures to differentiate them from the bedded mafic sequences. Furthermore, the line to the figure's right represents resistance to erosion for each unit. The faulting highlighted in G13 and G15 does not clearly express continuing upward. Continuity of these particular faults upwards is inferred.

The stratigraphical sequence in this research is explained as follows from the oldest to the youngest:
Unit G11 comprises white micas and forms the basal sequence of the Warrawoona stratigraphy within the northern CGB. The presence of these white micas could have been the result of different hydrothermal systems. The Al-micas indicate hydrothermal alteration from seawater recharge in a convective submarine hydrothermal system (Brauhart et al., 2000; van Ruitenbeek et al., 2006). Alternatively, the hydrothermal alteration could have resulted from magmatic fluid discharge related to the granitoid intrusion such as the Shaw Igneous Complex (DiMarco and Lowe, 1989; Van Kranendonk et al., 2002).
G11 comprises quartz-chlorite carbonate schists (Hein et al., n.d.) and an ultramafic contact with G1. This felsic basal sequence is not currently recognised, but fieldnotes of Hein et al. (n.d.) described a similar sequence. This unit is significant because it implies an eroded felsic depositional event that predates the 3.45Ga Duffer Formation.
Unit G1 indicates a mafic sequence marked by epidote, chlorites, amphiboles, carbonates and Mg-clays. The sequence shows distinct bedding and is interpreted to be interlayers of mafic and ultramafic rocks based on the mineralogy. G1 is interbedded with felsic sedimentary lenses with high magnetic signatures. These lenses are interpreted to be chert layers due to their magnetic signature. Hein et al. (n.d.) 's field observation notes highlight the occurrence of andesite-basalt and chert sequences that are conformably overlain by siltstone, tuff, shale and chert. The interbedded chert layers are described as slumped within the sedimentary packages (Hein et al., n.d.)
Furthermore the unit is truncated by NE-SW faults highlighted in Figure 17. The nCGB is crosscut by a series of NNW and NE trending faults (Scherrenberg et al., 2004) and several NNE-trending faults and shear-faults systems have been recorded by Hein (n.d.). Taking into account the interpreted mineralogical composition, distinct bedding and structural composition described for unit G1 in Table 5; a similarity can be drawn to the North Basalt made up of metamorphosed komatiites and basalts as described by (Hickman and Van Kranendonk, 2008). The mafic compositional layering and interbedded chert layers indicate that deposition is mainly volcanic with periods of quiescence in-between (Eriksson et al., 2001). Faulting and quartz veins could have been the pathways for fluid recharge within the sequence or a discharge of magmatic fluids from the bottom of the sequence (Pirajno, 2009a). The spatial distribution of alteration minerals in Figure 28 follows the stratigraphy zonated at the top of the sequence with carbonate, chlorite and epidote minerals as described in Table 5, as well as chloritic minerals along the fractures. Unit G1 is interpreted to have transitional contacts with units G12, and G13 to G15 are just part of the G1 sequence.

Unit G12 is a mafic sequence showing primarily interpreted amphibolite, epidote and dolomite minerals. There is uncertainty in the interpretation of dolomite due to the ambiguity of the spectra classified (Figures 24 and 27). However, the spectra show a high affinity to the carbonate group based on diagnostic absorptions for carbonates (~2302-2350, ~2140) (GMEX, 1997). Additionally, dolomite has been described as occurring in the southwestern parts of the nCGB (Zegers, 1996; Brasier et al., 2002; Hein et al., n.d.). The mineral associations indicated a carbonated mafic unit, having been deformed by the NE-SW fractures. Moderately high (MM) magnetic footprints (Figure 16b) are observed at the top of the sequence, and the zone has been interpreted as a goethite-hematite-rich zone (Figure 21). These characteristics and the hydrothermal alteration allude to this horizon as a probable volcanogenic massive-sulfide (VMS) exhalative horizon. Characterisation of exhalative horizons is under varying conditions in many active volcanic-hydrothermal systems (Sillitoe, 2015). This unit coincides with the McPhee formation, which has been geologically mapped as talc-carbonate and chlorite-serpentine schists (Van Kranendonk et al., 2002).

Unit G14 is interpreted to be part of the more extensive sequence of G1 with a higher concentration of epidote and Mg-clay (>40%). This implies chert deposition and thus a period of quiet deposition. Geological mapping noted the existence of layered jasplitic-chert-rich lenses throughout the mafic sequences in this area (Zegers, 1996; Van Kranendonk et al., 2002).

Unit G13 and G15 have been interpreted as the upper sequence of unit G1. The mafic carbonate-rich amphibolites, epidotes and chlorite and the spatial distribution of these minerals at the top of G1 support this. Evidently, lenses of felsic micas are also observed in these zones. G15 has been truncated by NE-SW fractures that separate this unit. These structures could have acted as possible conduits for hydrothermal fluids. The contact between G15 as the top sequence of G1 defines an unconformity and a potential paleosurface that should be further investigated on the ground. The mineralogy corresponds with the lithologies of Mt Ada Basalt as described by Van Kranendonk (2002) and Hickman (2011).

Unit G2 shows that the boundary between G1 and G2 presents an unconformity with a distinct change in mineral variation from mafic to felsic. This distinct change highlighted in the mineral map in Figure 27 would suggest the presence of a paleosurface. In contrast, the boundary between G2 and G1 in the NNW is gradational with intercalated chloritic and dolomitic material and might indicate simultaneous volcanic and sedimentary deposition. Unit G2 is interpreted as a pervasively hydrothermal altered layer with primarily different Al-micas of muscovite-illite, pure muscovite and phengite.

This felsic sequence laterally continues with a gradational transition into **unit G3,** reflecting a change in the deposition of the felsic material. Table 5 and field notes by Hein et al. (n.d.) describe G2 as volcanoclastic units that are successively overlain by laterally discontinuous beds of rhyodacite, tuff and pyroclastic agglomerate. Unit G3 is described as a volcanoclastic-sedimentary sequence, which comprises laterally continuous beds of conglomerate, sandstone and siltstone, jaspilite, chert and dolomite (Hein et al., n.d.). This is evidence that contact G2-G3 reflects a change in deposition and not just post-depositional alteration

Additionally, **unit G4** is a felsic layer stratigraphically overlaying G3, with a sharp contact between the two sequences with a change of the wite micas to a more Al-rich composition. Units G2-G4 are comparable to the Duffer formation from a spatial overlay with the geological map (Hickman and Van Kranendonk, 2008; Van Kranendonk, 2010). The formation is described as a volcanoclastic sedimentary sequence with dacitic volcanic breccia, sandstones and clay material in an active drainage channel (Hickman, 1983).

The K-content variation increases the stratigraphy from unit G2 to G4 (Figure 11). The K/eTh ratio of 0.4-1.5 highlighted in Figure 14 across these three units might indicate K-mobility as the chemical environment changes. Radiometric ratios of K/eTh are widely used as indicators of potassium enrichment in the hydrothermal system (Mamouch et al., 2022). Because potassium tends to be more mobile than thorium, the K/eTh is usually constant in many lithologies. Increases above thresholds of 0.2(K/eTh) are interpreted as hydrothermal alteration processes which give rise to magmatic-hydrothermal mineralisation (Hoover et al., 1992).

G2 and G3 are marked by a potassium content of 0f 2.8-4.4% (Table 4). The presence of Al-poor micas and dolomite (1%) might indicate a period of quiescence between volcano-sedimentary deposition and mineral formation at low alteration temperatures. The upper sequence G4, marked by Al-rich micas and high K-content, could signify volcano-sedimentary deposition and mineral formation in an aqueous environment but at higher alteration temperatures. Supporting evidence for this is reflected in studies carried out in the Panorama area in the Pilbara craton to characterize white micas using field reflectance spectroscopy in hydrothermal systems (Van Ruitenbeek et al., 2005; 2012). White micas were categorised on Al content in these studies to estimate the forming conditions. The Al-rich micas were restricted to low-temperature zones, whilst the Al-rich micas were an indicator of increased temperatures and acidic conditions (Van Ruitenbeek et al., 2012).

Unit G5, whilst it has a low K-content (Table 4), the mineral maps highlight this unit as muscovite rich with a transitional boundary with G4. This sequence is interpreted as an exhalative horizon based on its moderate magnetic footprint. This could indicate a discharge of magmatic fluids from the bottom of the sequence (Pirajno, 2009a). Unit G5 is similar to the layered chert of the Panorama formation as described in the published geological map (Van Kranendonk, 2010).

Unit G6 is marked by Al-rich micas such as muscovite and paragonite, spatially distributed at the top of the unit. The boundary between G6 and G4 represents an unconformity and a probable paleosurface. Of significance as well is the distinct bedded layers of mafic material between G4 and G6. The pattern is similar to that observed in the mafic sequence of G1 and is also assumed to be the same as for G16 could represent a cyclic deposition event across the study area. Additionally, G6 is marked by a relatively high K-content (Table 4). The association of the Al-rich micas and high K-content is similar to G4 and could indicate high formation temperatures. High-temperature zones in an aqueous environment tend to be marked by chlorite-quartz facies (Van Ruitenbeek et al., 2012), and this might indicate an underlying more mafic (basaltic) lithological composition (Van Kranendonk and Pirajno, 2004) for unit G6.

The boundary between G6 and G7 is also considered a potential paleosurface with an abrupt change in the chemical environment. **Unit G7** is marked by pyrophyllite at the bottom of the sequence, in association with dickite and alunite. Figure 27 shows the occurrence of pyrophyllite continuing into the bottom levels of G6. This continuation could have been facilitated through the continuous fault system shown in Figure 16 that displaces G6 and G7. Pyrophyllite occurs in a shallow-submarine setting with reducing acidic conditions, silica-rich and low-intermediate temperature hydrothermal fluids (Pirajno, 2009b, Brown et al., 2006); therefore, the pyrophyllite occurrence is interpreted as formed under similar conditions. G7 is also marked at the top of the sequence by significant magnetic anomalies interpreted as the result of the occurrences of BIFs. The Fe-rich sequences resemble the Cleaverville Formation with rich BIF horizons and quartz-magnetite rocks (Hickman, 2011).

A clear angular unconformity between G7 and G8 and the boundary is considered a potential paleosurface. **Unit G8** is marked by Al-rich mica with a pervasive spatial distribution over the layer. This layer might represent a more quiet environment after the deposition of G7. The unit presents a very high radioelement concentration (Table 4) with no magnetic relief. This unit is comparable to that of the Lallah Rook Sandstone, made up of sandstone, conglomerates and shales (Hickman, 2011).

Unit G9 is interpreted to be at the top of the sequence, overlying unit G8 and marked by a high felsic content. The unit is pervasively altered and marked with Al-rich micas. The radioelement concentration of eTh of 3.9-5.4 ppm could indicate an underlying mafic lithological composition (Van Kranendonk and Pirajno, 2004).

Unit G10, G17 and G18 were not classified as part of the stratigraphy for the sequence of the nCGB.

6.2. Accuracy and Uncertainty

Several sources of error affected the accuracy and precision of mineral prediction. Airborne data has a lot of ambiguity, from its processing as well as interpretation of it. Geolocation errors in the georegistration of the AMS hyperspectral imagery resulted in the interpretations of mineral location and spatial distribution. This introduced random errors and affected the interpretation of occurrence and spatial distribution. The effect of erroneous geolocation was also noticeable as it misaligned the geophysical data sets to the hyperspectral data in the overlay analysis. However, the geocorrection of the hyperspectral image was an overall geolocation error for the hyperspectral map was ~15m and ~20m to the far west.

Pixel inhomogeneity within mineral spectra was another factor that affected the accuracy of the mineral map. Manually picking pixels from image data meant assuming the pixel was homogeneous. This would have resulted in interpreted spectra not representative of the pixels from which they were picked. Mineral groups such as carbonates and ferric oxides were mainly affected. Additionally, the inhomogeneity of pixels meant that a separation of mineral and vegetation pixels could not be determined. The effect was that the accuracy of mineral classification was hindered and introduced uncertainty in mineral classification.

A systematic error was also present in mineral interpretations. The hyperspectral data had an insufficient spectral resolution between 1300-1900nm. This resulted in a failure to incorporate any diagnostic features between that range. In some cases, this made a complete identification of mineral spectra impossible, introducing uncertainty in the mineral classification.

Another source of error was the noise in the VNIR spectrum. This effect was observed in Figure 21, where it was challenging to pick clear pixels. A possibility for this noise was merging VNIR and SWIR data after acquisition so that each image pixel describes a complete spectral signature between 400 nm and 2500 nm. The noise effects were at the extremes of the spectrum (>960nm), at which a diagnostic feature for ferric minerals can be found. This made the classification of iron minerals difficult.

6.3. Limitations

- No rock samples were used to compare the airborne hyperspectral and field spectra. This resulted in having no means of validating the remotely sensed data with the ground truth.
- Manually picking end members means the possibility of leaving out end members
- Comparison with spectral libraries requires knowledge of ground composition; library spectra may differ from sensor
- Characterisation of alteration types fully requires additional petrological and geochemical techniques, also based on sample material
- Differentiating between primary minerals and secondary minerals, e.g. primary chlorite, primary biotite and alteration forms
- The distribution or extent of alteration zones cannot be fully classified by observation of individual mineral groups and remotely-sensed data.

6.4. Recommendations for further studies

Fieldwork is recommended to improve the ambiguities and limitations highlighted in this research and further studies. The field work is proposed to check the following:

- Carry out a systematic prospect-scale mapping in order to identify each of the paleosurfaces mentioned in this study
- Confirm the existence of the predicted structural and deformation markers and their continuity
- Identify the exhalative horizons and their spatial continuity
- Collect samples at locations concordant to the mineral map to validate the classification

Laboratory work is also required, including petrogenic and chemical analyses of the field samples for comprehensive classification of the hydrothermal alteration.

7. CONCLUSION

7.1. Conclusions

In this research, an integrated approach was used to investigate the hydrothermal events and related paleosurfaces within the northern part of the Coongan Greenstone Belt. Radiometric data were analysed and interpreted to form the framework of the study, showing the mineral zonation and general division of the lithologic units in the nCGB. Magnetic data also enhanced the classification of the lithologic units based on the magnetic signal and added the structural details to the interpreted features from the gamma-ray. Subsequently, mineral mapping techniques were applied to the airborne hyperspectral data, and a mineral map was produced. Interpretations of hydrothermal minerals' occurrence and spatial distribution were done to see how they related to the general division of the nCGB. The spatial distribution of these hydrothermal alteration minerals and rock unit characteristics were summarised and organised into a relative chronology of events for the nCGB. The conclusions drawn from this research and answering the research questions are summarised below.

1. **Which hydrothermal alteration minerals can be classified using hyperspectral mapping in the study area?**

Applying mineral mapping methods to the airborne hyperspectral data identified various hydrothermal alteration assemblages ranging from chlorite-carbonate to different white micas and pyrophyllite types. The classified minerals are pyrophyllite, dickite, alunite, kaolinite, white micas (muscovite, illite, paragonite, phengite), epidote, chlorite, amphiboles, dolomite, nontronite-saponite, Fe-MG chlorite, talc, serpentinite, hematite and goethite. The mineral classification carried uncertainties based on geolocation errors, inhomogeneous image pixels and insufficient spectral resolution in the hyperspectral data. However, the capability of classifying white micas, clays, sulfates, silicates, carbonates and iron oxides indicated a hydrothermal alteration system within the nCGB.

2. **Which paleosurfaces are distinguished, and what is their relationship with identified surface minerals?**

Potential paleosurfaces were identified through the nature of the contacts between the different lithological units. Seven potential paleosurfaces were identified as they were interpreted to be the equivalent of the sharp contacts between units. The potential surfaces presented as unconformities with distinct surface mineralogical changes between the units. This inferred a change in the depositional and mineral formation environment within the nCGB.

3. **Are there recognisable patterns at the paleosurfaces in relation to continuity, mineral patterns, and depth?**

Hydrothermal alteration followed various distribution patterns, including a pervasive pattern in the felsic regions, along the top or bottom of sequences in the more mafic regions, and along fault systems and drainage channels. The spatial distribution of alteration minerals indicates episodes of hydrothermal alteration connected to paleo-layers within the volcano-sedimentary sequence. The occurrence of pyrophyllite indicates reducing acidic conditions, silica-rich and low-intermediate temperature hydrothermal fluids. Variations in pyrophyllite and muscovite up the stratigraphy towards the paleosurface suggest a connected hydrothermal system with changing temperature, acidity and redox conditions.

4. **What is the role of the multi-disciplinary data sets in improving the understanding of the development systems in the study area?**

The use of multi-disciplinary data sets offered an integrated approach to building up the development system in the study area. The research methodology approach centred on extracting details from low resolution to get the regional framework of the study and moving up to a high resolution to give a more detailed analysis of the local framework. As such, the gamma-ray was used to show the general zonation in the study area and create a framework of the major divisions based on radioelement signatures. The magnetic data also enhanced the classification of the lithologic units based on the magnetic signal and added structural details to the interpreted features from the gamma-ray. Finer details in the mineralogical framework were extracted from the hyperspectral data and constrained the mineralogical occurrences within specific boundaries. Overall, the different sources of information, either low-resolution or high resolution, offered regional and local perspectives that led to a comprehensive geological interpretation.

5. **Which role did the hydrothermal events play in the study area, and can they be distinguished temporally?**

The qualitative surface mineral map showed white micas (muscovite, paragonite, phengite, illite), clay minerals (pyrophyllite, kaolinite, dickite), silicates (amphibole, biotite epidote, chlorite, talc), carbonate minerals (dolomite), sulfate minerals (alunite) and iron oxides (hematite, goethite). This spatial distribution of alteration minerals indicates episodes of hydrothermal alteration connected to paleo-layers within the volcano-sedimentary sequence. Additionally, the spatial distribution of these hydrothermal alteration minerals and rock unit characteristics were summarised and organised into a relative chronology of events for the nCGB. The overall sequence of events shows a younging direction up the stratigraphy towards the east. The correlation between the potential paleosurfaces formation interpreted hydrothermal alteration, and inferred changes in paleoenvironment across the study area indicate that there have been temporal changes in the nCGB study area with part of the field indicating a connected hydrothermal system with changing temperature, acidity and redox conditions.

LIST OF REFERENCES

Abubakar, A.J. afar, Hashim, M., Pour, A.B., 2018. Hydrothermal alteration mapping of mineralogical imprints associated with subtle geothermal system using mixture tuned matched filtering approach on ASTER VNIR And SWIR data. ARPN Journal of Engineering and Applied Sciences 13, 1226–1234.

Anhaeusser, C.R., 2014. Archaean greenstone belts and associated granitic rocks - A review. Journal of African Earth Sciences 100, 684–732. https://doi.org/10.1016/j.jafrearsci.2014.07.019

Bakker, W.H., 2012. HypPy User Manual [WWW Document]. ITC - University of Twente. URL http://www.itc.nl/personal/bakker/hyppy.html

Bakker, W.H., van Ruitenbeek, F.J.A., van der Werff, Harald, M.A., 2011. Hyperspectral image mapping by automatic colour coding of absorption features. 7th EARSEL Workshop of the Special Interest Group in Imaging Spectroscopy.

Beraldi-Campesi, H., 2013. Early life on land and the first terrestrial ecosystems. Ecological Processes 2, 1. https://doi.org/10.1186/2192-1709-2-1

Brasier, M.D., Green, O.R., Jephcoat, A.P., Kleppe, A.K., Van Kranendonk, M.J., Lindsay, J.F., Steele, A., Grassineau, N. V., 2002. Questioning the evidence for Earth's oldest fossils. Nature 416, 76–81. https://doi.org/10.1038/416076a

Brasier, M.D., Green, O.R., Lindsay, J.F., McLoughlin, N., Steele, A., Stoakes, C., 2005. Critical testing of Earth's oldest putative fossil assemblage from the ∼3.5 Ga Apex chert, Chinaman Creek, Western Australia. Precambrian Research 140, 55–102. https://doi.org/10.1016/j.precamres.2005.06.008

Brauhart, C.W., Groves, D.I., Murant, P., 1998. Regional alteration systems associated with volcanogenic massive sulfide mineralization at Panorama, Pilbara, Western Australia. Economic Geology 93, 292–302. https://doi.org/10.2113/gsecongeo.93.3.292

Brauhart, C.W., Huston, D.L., Andrew, A.S., 2000. Oxygen isotope mapping in the Panorama VMS district, Pilbara Craton, Western Australia: Applications to estimating temperatures of alternation and to exploration. Mineralium Deposita 35, 727–740. https://doi.org/10.1007/s001260050275

Brown, A.J., Cudahy, T.J., Walter, M.R., 2006. Hydrothermal alteration at the Panorama Formation, North Pole Dome, Pilbara Craton, Western Australia. Precambrian Research 151, 211–223. https://doi.org/10.1016/j.precamres.2006.08.014

Chang, C.-I., 2003. Hyperspectral Imaging, Hyperspectral Imaging. Springer US, Boston, MA. https://doi.org/10.1007/978-1-4419-9170-6

Clark, R.N., King, T.V.V., Klejwa, M., Swayze, G.A., Vergo, N., 1990. High spectral resolution reflectance spectroscopy of minerals. Journal of Geophysical Research 95. https://doi.org/10.1029/jb095ib08p12653

Cudahy, T., Jones, M., Thomas, M., Laukamp, C., Caccetta, M., Hewson, R., Rodger, A., Verrall, M., 2008. Next Generation Mineral Mapping : Queensland Airborne HyMap and Satellite ASTER Surveys 2006-2008. CSIRO Exploration & Mining Report P2007 / 364 152.

Cudahy, T.J., Rodger, A.P., Barry, P.S., Mason, P., Quigley, M., Folkman, M., Pearlman, J., 2002. Assessment of the stability of the Hyperion SWIR module for hyperspectral mineral mapping using multidate images from Mount Fitton, Australia. International Geoscience and Remote Sensing Symposium (IGARSS) 6, 3504–3506. https://doi.org/10.1109/igarss.2002.1027230

De Wit, M.J., 1998. On Archean granites, greenstones, cratons and tectonics: does the evidence demand a verdict? Precambrian Research 91, 181–226. https://doi.org/10.1016/S0301-9268(98)00043-6

de Wit, M.J., Hart, R., Martin, A., Abbott, P., 1982. Archean abiogenic and probable biogenic structures associated with mineralized hydrothermal vent systems and regional metasomatism, with implications for greenstone belt studies. Economic Geology 77, 1783–1802. https://doi.org/10.2113/gsecongeo.77.8.1783

DiMarco, M.J., Lowe, D.R., 1989. Stratigraphy and sedimentology of an Early Archean Felsic Volcanic Sequence, Eastern Pilbara Block, Western Australia, with special reference to the Duffer Formation and implications for Crustal Evolution. Precambrian Research 44, 147–169. https://doi.org/10.1016/0301-9268(89)90080-6

Ericsson, M., Löf, O., 2019. Mining's contribution to national economies between 1996 and 2016. Mineral Economics 32, 223–250. https://doi.org/10.1007/s13563-019-00191-6

Eriksson, P.G., Martins-Neto, M.A., Nelson, D.R., Aspler, L.B., Chiarenzelli, J.R., Catuneanu, O., Sarkar, S., Altermann, W., Rautenbach, C.J. d. W., 2001. An introduction to Precambrian basins: Their characteristics and genesis. Sedimentary Geology 141–142, 1–35. https://doi.org/10.1016/S0037-0738(01)00066-5

Geoscience Australia and Australian Stratigraphy Commission, 2017. Australian Stratigraphic Units Database. URL https://asud.ga.gov.au/search-stratigraphic-units/results/26238 (accessed 11.14.21).

Gifkins, C., Herrmann, W., Large, R.R., 2005. Altered Volcanic Rocks: A Guide to Description and Interpretation. Centre for Ore Deposit Research, University of Tasmania.

GMEX, 2008. GMEX Guides for Mineral Exploration: Spectral Interpretation Field Manual Volume 1, 3rd ed. AusSpec International.

GMEX, 1997. GMEX Guides for Mineral Exploration: Spectral Interpretation Field Manual Volume 1, 1st ed. AusSpec International.

Goodwin, A., 1981. Chapter 5 Archaean Plates and Greenstone Belts. Developments in Precambrian Geology 4, 105–135. https://doi.org/10.1016/S0166-2635(08)70010-0

Gupta, R.P., 1991. Remote Sensing Geology, 1st ed, Remote Sensing Geology. Springer Berlin Heidelberg, Berlin, Heidelberg. https://doi.org/https://doi.org/10.1007/978-3-662-12914-2

Haldar, S.K., 2018. Economic Mineral Deposits and Host Rocks. Mineral Exploration 25–45. https://doi.org/10.1016/b978-0-12-814022-2.00002-2

Hamilton, W.B., 1998. Archean magmatism and deformation were not products of plate tectonics. Precambrian Research 91, 143–179. https://doi.org/10.1016/S0301-9268(98)00042-4

Hecker, C.A., van Ruitenbeek, F.J.A., Bakker, W.H., Babatunde J., F., Dean., R., Harald M.A., van der W., van der Meer, F.D., 2019a. Mapping the wavelength position of mineral features in hyperspectral thermal infrared data. International Journal of Applied Earth Observation and Geoinformation 79, 133–140. https://doi.org/10.1016/j.jag.2019.02.013

Hecker, C.A., van Ruitenbeek, F.J.A., van der Werff, H.M.A., Bakker, W.H., Hewson, R., van der Meer, F.D., 2019b. Feature Analysis for Finding Ore. IEEE Geoscience and Remote Sensing Magazine 7, 51–71.
Hein, K.A.A., Leeuw, G.A.M. de, Scherrenberg, A.F., Wijbrans, J.R., S., W., n.d. Volcano-sedimentary stratigraphy of the northern Coongan Greenstone Belt, East Pilbara Granite-Greenstone Terrain, Australia.
Hickman, A., 1983. Geology of the Pilbara Block and its environs. Geological Survey of Western Australia, Bulletin 127.
Hickman, A.H., 2012. Review of the Pilbara Craton and Fortescue Basin, Western Australia: Crustal evolution providing environments for early life. Island Arc 21, 1–31. https://doi.org/https://doi.org/10.1111/j.1440-1738.2011.00783.x
Hickman, A.H., 2011. Pilbara Supergroup of the East Pilbara Terrane, Pilbara Craton: updated lithostratigraphy and comments on the influence of vertical tectonics. Geological Survey of Western Australia, Annual Review 2009-2010 51–59.
Hickman, A.H., Van Kranendonk, M.J., 2012. Early Earth evolution: Evidence from the 3.5-1.8 Ga geological history of the Pilbara region of Western Australia. Episodes 35, 283–297. https://doi.org/10.18814/epiiugs/2012/v35i1/028
Hickman AH, Van Kranendonk, M., 2008. Marblebar_2855.pdf. Geological Survey of Western Australia. URL https://geodocs.dmirs.wa.gov.au/Web/documentlist/3/Combined/P00AY
Hoover, D.B., Heran, W.D., Hill, P.L., 1992. The geophysical expression of selected mineral deposit models, USGS Numbered Series, Open File Report. https://doi.org/10.3133/ofr92557
Hunt, G.R., 1977. Spectral Signatures of Particulate Minerals in the Visible and Near Infrared. Geophysics 42, 501–513. https://doi.org/10.1190/1.1440721
Huston, D.L., Sun, S.S., Blewett, R., Hickman, A.H., Van Kranendonk, M., Phillips, D., Baker, D., Brauhart, C., 2002. The timing of mineralization in the Archean North Pilbara terrain, Western Australia. Economic Geology 97, 733–755. https://doi.org/10.2113/gsecongeo.97.4.733
Jutras, P., Prichonnet, G., 2004. Significance of paleosurfaces in interpreting the paleogeographic and stratigraphic evolution of the late Paleozoic Paspébiac graben, a recently identified basin in the southern Gaspé Peninsula of Quebec Canada. Bulletin of the Geological Society of America 116, 1074–1086. https://doi.org/10.1130/B25438.1
Kruse, F.A., 1988. Use of airborne imaging spectrometer data to map minerals associated with hydrothermally altered rocks in the northern grapevine mountains, Nevada, and California. Remote Sensing of Environment 24, 31–51. https://doi.org/10.1016/0034-4257(88)90004-1
L3 Harris Geospatial, n.d. ENVI Tutorials. URL https://www.l3harrisgeospatial.com/docs/tutorials.html (accessed 11.9.21).
Lawrence, M., Stenning, L., 2009. Marble Bar, Western Australia Airborne magnetic and Radiometric Geophysical Survey: Acquisition and Processing Report.
Magendrana, T., Sanjeevi, S., 2014. Hyperion image analysis and linear spectral unmixing to evaluate the grades of iron ores in parts of Noamundi, Eastern India. International Journal of Applied Earth

Observation and Geoinformation 26, 413–426. https://doi.org/10.1016/j.jag.2013.09.004
Maghsoudi Moud, F., van Ruitenbeek, F., Hewson, R., van der Meijde, M., 2021. An approach to accuracy assessment of aster derived mineral maps. Remote Sensing 13. https://doi.org/10.3390/rs13132499
Mamouch, Y., Attou, A., Miftah, A., Ouchchen, M., Dadi, B., Achkouch, L., Et-Tayea, Y., Allaoui, A., Boualoul, M., Randazzo, G., Lanza, S., Muzirafuti, A., 2022. Mapping of Hydrothermal Alteration Zones in the Kelâat M'Gouna Region Using Airborne Gamma-Ray Spectrometry and Remote Sensing Data: Mining Implications (Eastern Anti-Atlas, Morocco). Applied Sciences (Switzerland) 12, 1–19. https://doi.org/10.3390/app12030957
Murphy, R.J., Monteiro, S.T., 2013. Mapping the distribution of ferric iron minerals on a vertical mine face using derivative analysis of hyperspectral imagery (430-970nm). ISPRS Journal of Photogrammetry and Remote Sensing 75, 29–39. https://doi.org/10.1016/j.isprsjprs.2012.09.014
Nijman, W., Kloppenburg, A., de Vries, S.T., 2017. Archaean basin margin geology and crustal evolution: An East Pilbara traverse. Journal of the Geological Society 174, 1090–1112. https://doi.org/10.1144/jgs2016-127
Pirajno, F., 2009a. Tectonic Settings, Geodynamics and Temporal Evolution of Hydrothermal Mineral Systems, in Hydrothermal Processes and Mineral Systems. pp. 165–203. https://doi.org/10.1007/978-1-4020-8613-7_3
Pirajno, F., 2009b. Hydrothermal Processes and Wall Rock Alteration, in Hydrothermal Processes and Mineral Systems. pp. 73–164. https://doi.org/10.1007/978-1-4020-8613-7_2
Portela, B., Sepp, M.D., Ruitenbeek, F.J.A. Van, Hecker, C., Dilles, J.H., 2021. Using hyperspectral imagery for the identification of pyrophyllite-muscovite intergrowths and alunite in the shallow epithermal environment of the Yerington porphyry copper district. Ore Geology Reviews 131, 104012. https://doi.org/10.1016/j.oregeorev.2021.104012
Rajagopalan, S., 2003. Analytic Signal vs. Reduction to Pole: Solutions for Low Magnetic Latitudes. ASEG Extended Abstracts 2003, 1–4. https://doi.org/10.1071/aseg2003ab136
Ray, R.G., 1960. Aerial Photographs in Geologic Interpretation and Mapping, Geological Survey Professional Paper.
Scherrenberg, A.F., Hein, K.A.A., White, S., 2004. Middle Archaean gold deposits in the North Shaw-Coongan Greenstone Belt, Australia: The relative timing of events responsible for gold mineralisation. Ore Geology Reviews 25, 175–197. https://doi.org/10.1016/j.oregeorev.2004.04.001
Schopf, W.J., Packer, B.M., 1987. Early Archean (3.3-Billion to 3.5-Billion-Year-Old) Microfossils from Warrawoona Group, Australia. Science 237, 70–73. https://doi.org/10.1126/science.11539686
Sillitoe, R.H., 2015. Epithermal paleosurfaces. Mineralium Deposita 50, 767–793. https://doi.org/10.1007/s00126-015-0614-z
Tripathi, M.K., Govil, H., 2019. Evaluation of AVIRIS-NG hyperspectral images for mineral identification and mapping. Heliyon 5, e02931. https://doi.org/10.1016/j.heliyon.2019.e02931
Tripathi, M.K., Govil, H., Chattoraj, S.L., 2020. Identification of hydrothermal altered/weathered and clay

minerals through airborne AVIRIS-NG hyperspectral data in Jahajpur, India. Heliyon 6, e03487. https://doi.org/10.1016/j.heliyon.2020.e03487
Trofimovs, J., Davis, B.K., Cas, R.A.F., Barley, M.E., Tripp, G.I., 2006. Reconstructing the event stratigraphy from the complex structural-stratigraphic architecture of an Archaean volcanic-intrusive-sedimentary succession: The Boorara Domain, Eastern Goldfields Superterrane, Western Australia. Australian Journal of Earth Sciences 53, 303–327. https://doi.org/10.1080/08120090500499297
van der Meer, F.D., van der Werff, H.M.A., van Ruitenbeek, F.J.A., Hecker, C.A., Bakker, W.H., Noomen, M.F., van der Meijde, M., Carranza, E.J.M., de Smeth, J.B., Woldai, T., 2012. Multi- and hyperspectral geologic remote sensing: A review. International Journal of Applied Earth Observation and Geoinformation 14, 112–128. https://doi.org/10.1016/j.jag.2011.08.002
Van Kranendonk, M.J.;, Hickman, A.H.;, Smithies, H.R.;, Nelson, D.R., 2002. Geology and Tectonic Evolution of the Archean North Pilbara Terrain, Pilbara Craton, Western Australia. Economic Geology 97, 695–732. https://doi.org/10.2113/97.4.695
Van Kranendonk, M.J., 2010. Geology of the Coongan 1:100 000 sheet: Western Australia Geological Survey, 1:100 000 Geological Series Explanatory Notes.
Van Kranendonk, M.J., 2006. Volcanic degassing, hydrothermal circulation and the flourishing of early life on Earth: A review of the evidence from c. 3490-3240 Ma rocks of the Pilbara Supergroup, Pilbara Craton, Western Australia. Earth-Science Reviews 74, 197–240. https://doi.org/10.1016/j.earscirev.2005.09.005
Van Kranendonk, M.J., Hickman, A.H., Smithies, H.R., Nelson, D.R., Pike, G., 2002. Geology and Tectonic Evolution of the Archean North Pilbara Terrain, Pilbara Craton, Western Australia. Economic Geology 97, 695–732. https://doi.org/10.2113/97.4.695
Van Kranendonk, M.J., Pirajno, F., 2004. Geochemistry of metabasalts and hydrothermal alteration zones associated with c. 3.45 Ga chert and barite deposits: Implications for the geological setting of the Warrawoona group, Pilbara Craton, Australia. Geochemistry: Exploration, Environment, Analysis 4, 253–278. https://doi.org/10.1144/1467-7873/04-205
Van Ruitenbeek, F.J.A., Cudahy, T., Hale, M., van der Meer, F.D., 2005. Tracing fluid pathways in fossil hydrothermal systems with near-infrared spectroscopy. Geology 33, 597–600. https://doi.org/10.1130/G21375.1
Van Ruitenbeek, F.J.A., Cudahy, T.J., van der Meer, F.D., Hale, M., 2012. Characterization of the hydrothermal systems associated with Archean VMS-mineralization at Panorama, Western Australia, using hyperspectral, geochemical and geothermometric data. Ore Geology Reviews 45, 33–46. https://doi.org/10.1016/j.oregeorev.2011.07.001
van Ruitenbeek, F.J.A., Debba, P., van der Meer, F.D., Cudahy, T., van der Meijde, M., Hale, M., 2006. Mapping white micas and their absorption wavelengths using hyperspectral band ratios. Remote Sensing of Environment 102, 211–222. https://doi.org/10.1016/j.rse.2006.02.012
Walter, M.R., Des Marais, D.J., 1993. Preservation of Biological Information in Thermal Spring Deposits: Developing a Strategy for the Search for Fossil Life on Mars. Icarus 101, 129–143.

https://doi.org/10.1006/icar.1993.1011
Widdowson, M., 1997. The geomorphological and geological importance of palaeosurfaces. Geological Society Special Publication 120, 1–12. https://doi.org/10.1144/GSL.SP.1997.120.01.01
Wit, M.J.D., Furnes, H., 2016. Climatology: 3.5-Ga hydrothermal fields and diamictites in the Barberton Greenstone Belt-Paleoarchean crust in cold environments. Science Advances 2. https://doi.org/10.1126/SCIADV.1500368
Wolfe, J.D., Black, S.R., 2018. Hyperspectral Analytics in ENVI Target Detection and spectral Mapping Methods.
Wyborn, L.A.I., Heinrich, C.A. and Jaques, A.L., 1994. Australian Proterozoic Mineral Systems: Essential Ingredients and Mappable Criteria, in Australian Institute of Mining and Metallurgy Annual Conference. pp. 109–115.
Yousefi, M., Kreuzer, O.P., Nykänen, V., Hronsky, J.M.A., 2019. Exploration information systems – A proposal for the future use of GIS in mineral exploration targeting. Ore Geology Reviews 111. https://doi.org/10.1016/j.oregeorev.2019.103005
Zegers, T., 1996. Structural, kinematic and metallogenic evolution of selected domains of the Pilbara granitoid-greenstone terrain : implications for mid-Archean tectonic regimes, Geologica Ultraiectina.

APPENDIX

Annex 1: Ground Control Points

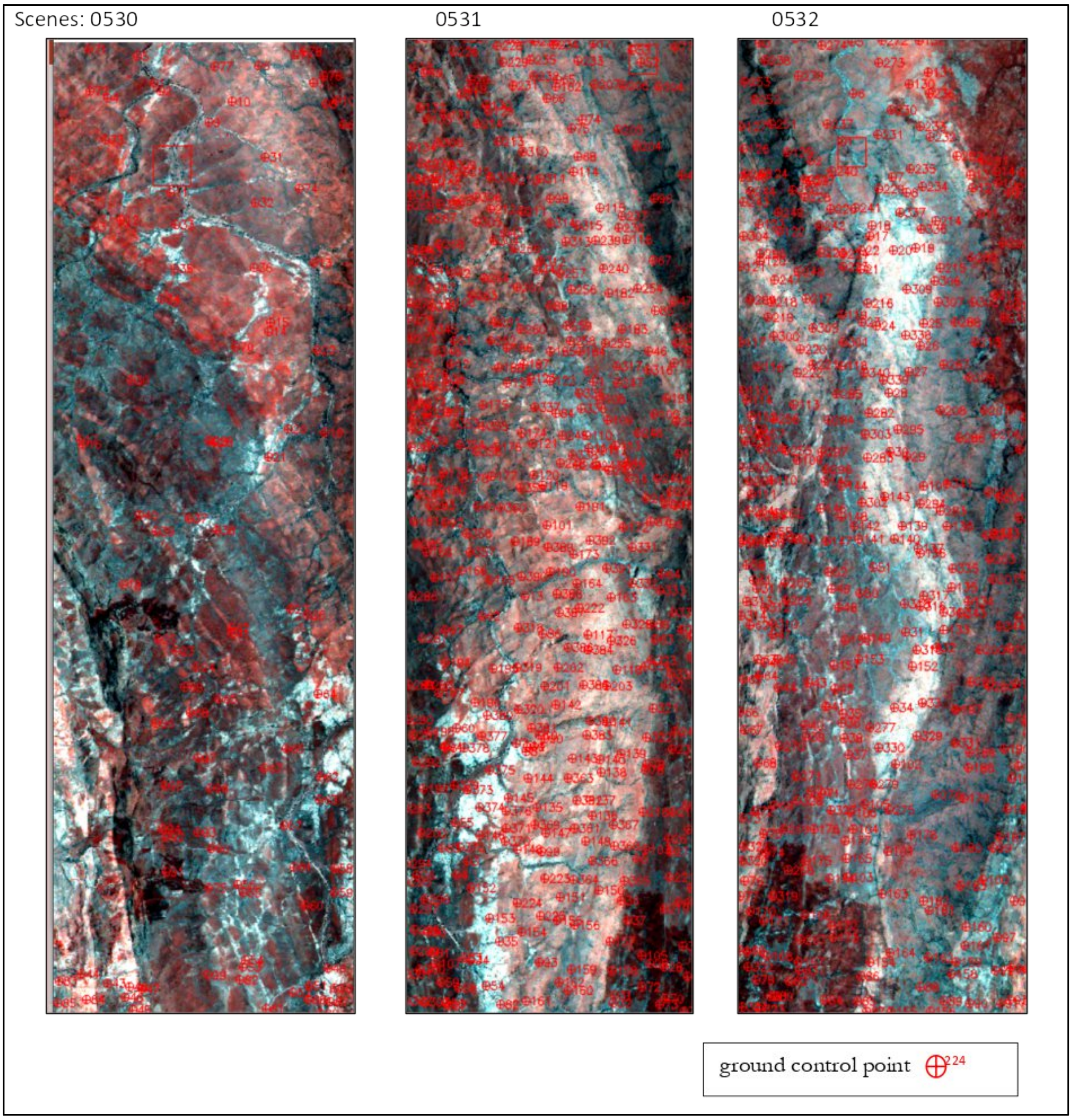

Annex 2: CTIC

Before CTIC

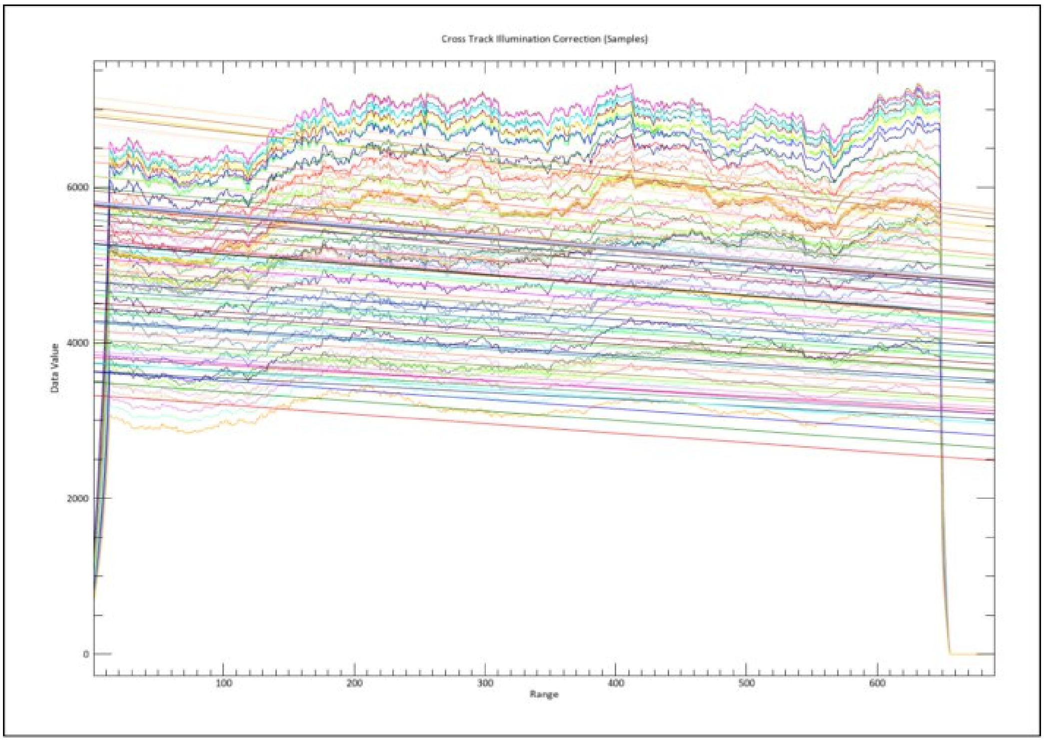

After CTIC